DESIGN AND DEVELOPMENT OF A CONTINUOUSLY VARIABLE TRANSMISSION SYSTEM TO BE USED IN HUMAN-ROBOT INTERFACES

A Thesis Submitted to the
Graduate School of Engineering and Sciences of
İzmir Institute of Technology
in Partial Fulfillment of the Requirements for the Degree of

MASTER OF SCIENCE

in Mechanical Engineering

by
Emir MOBEDİ

December 2018
İZMİR

We approve the thesis of **Emir MOBEDİ**

Examining Committee Members:

Assoc. Prof. Dr. M. İ. Can DEDE
Department of Mechanical Engineering, İzmir Institute of Technology

Assoc. Prof. Dr. Gökhan KİPER
Department of Mechanical Engineering, İzmir Institute of Technology

Prof. Dr. Lale Canan DÜLGER
Department of Mechanical Engineering, İzmir University of Economics

27 December 2018

Assoc. Prof. Dr. M. İ. Can DEDE
Supervisor
Department of Mechanical Engineering
İzmir Institute of Technology

Prof. Dr. Metin TANOĞLU
Head of the Department of
Mechanical Engineering

Prof. Dr. Aysun SOFUOĞLU
Dean of the Graduate School of
Engineering and Sciences

ACKNOWLEDGMENTS

I would first like to thank my thesis advisor, Assoc. Prof. Dr. M. İ. Can DEDE, for his support during my master education period. His door was always open whenever I ran into a trouble spot or had a question about my research. I would also like to express my sincere gratitude to Assoc. Prof. Dr. Gökhan Kiper for his valuable guidance and encouragement throughout NeuRoboScope project.

Also, I would like to thank my friends in IZTECH Robotics Lab. for their support and friendship, Çağhan Kirişçi, Emre Uzunoğlu, Osman Şahin, Barış Taner, Omar Maaroof, Orhan Ayit, Oğulcan Işıtman, Gizem Ateş, İbrahimcan Görgülü, Merve Özkahya.

Finally, I must express my very profound gratitude to my parents and my uncle for providing me with unfailing support and continuous encouragement throughout my years in IYTE and through the process of researching and writing this thesis. This accomplishment would not have been possible without them. Thank you.

This work is supported in part by The Scientific and Technological Research Council of Turkey via grant number 117M405.

ABSTRACT

DESIGN AND DEVELOPMENT OF A CONTINUOUSLY VARIABLE TRANSMISSION SYSTEM TO BE USED IN HUMAN-ROBOT INTERFACES

Continuously Variable Transmission (CVT) systems are being used for many applications such as automotive transmissions, robotics, and aerospace. In an ideal condition, these systems have the potential to provide continuously varying power transmission within a predefined limit. This transmission is accomplished with the help of friction, belt or gear systems. CVT can find application in a human-robot interface if a set of design criteria including backdrivability, independent output position and stiffness variation, shock absorbing and low mass and inertia can be satisfied. Even if there are various CVT designs in the literature for human-robot interfaces, the primary limitation of the two-cone drive CVT designs is that the output torque and the output position cannot be altered independently. Considering the friction drive CVT designs, the reason for this problem is that the friction wheel, which is designed to transmit the torque from the input cone to the output cone, gives rise to remarkable longitudinal friction force along the linear way. In order to overcome this problem, a sphere is used in the work presented in this thesis for the CVT design as the transmission element. In addition, it is stated in the literature that common CVT drive systems do not have the capability to be used in cyclic bidirectional motion. In the presented CVT design, a second sphere is added to the system with two springs from the lower part of the cones for pre-tension in order to solve the bidirectional transmission problem. Additionally, an adjustment of the normal force applied on the cones is designed in order to regulate the shock absorption limitations.

ÖZET

İNSAN-ROBOT ARAYÜZLERİNDE KULLANILMASI İÇİN BİR SÜREKLİ DEĞİŞKEN AKTARMA SİSTEMİ TASARIMI VE GELİŞTİRİLMESİ

Sürekli değişken aktarma (SDA) sistemleri otomotiv şanzımanlarında, robotik ve havacılık gibi bir çok uygulamada kullanılmaktadır. Bu sistemler teorik olarak belirli bir sınır arasında güç aktarımını kademesiz olarak değiştirebilmektedir. Söz konusu aktarma; kayış, zincir veya kuru sürtünme ile sağlanmaktadır. SDA sistemleri; geri sürülebilirlik, konumun ve direngenliğin bağımsız olarak kontrol edilebilmesi, ani fiziksel çarpışmaların sönümlenebilmesi ve düşük ataletsel özelliklere sahip olma gibi kriterlerin sağlanabildiği durumda, insan-robot ara yüzlerindeki uygulamalarda yer bulabilir. Literatürde insan-robot ara yüzlerinde kullanılması için tasarlanan çeşitli SDA sistemleri bulunsa da, iki koni ile oluşturulan SDA tasarımlarının temel kısıtlaması, çıkış konumunun ve çıkış torkunun bağımsız olarak değiştirilememesidir. Kuru sürtünme prensibi ile oluşturulan SDA sistemleri göz önüne alındığında, bahsi geçen problemin sebebi şudur: giriş konisinden çıkış konisine aktarmayı sağlayan sürtünme tekerleği önemli derecede boylamsal yönde sürtünme kuvvetine yol açmaktadır. Bu meselenin çözümlenmesi için, aktarmayı sağlayan eleman olarak bir küre kullanılmıştır. Ayrıca, yayın taramasında rastlanan bir başka problem de şudur: iki koni ile oluşturulan SDA sistemleri periyodik olarak iki yönde (saat yönü ve saatin tersi yönü) çıkış konumunu değiştirebilme kabiliyetine sahip değildir. Bu tezde sunulan özgün SDA sisteminde söz konusu problemin çözümüne yönelik olarak ikinci küre sisteme konilerin alt kısmından ön gerilmeli yaylar ile birlikte eklenmiştir. Bunlara ek olarak, koninin yüzeyine uygulanan normal kuvvetin ayarlanması sağlanarak şok sönümleme sınırlarının düzenlenmesi sağlanmıştır.

I dedicated this thesis to my dear parents İlkay and Muhammed Mobedi.

TABLE OF CONTENTS

LIST OF FIGURES

Figure **Page**

LIST OF TABLES

CHAPTER 1

INTRODUCTION

The early applications of the robots in the industry were performed by only using a pure position controllers. The first examples of these robots are found in automotive industry which are employed for painting, polishing, welding. The main function of these robots is that they accomplish the task by following a predefined trajectory with minimum position error.

The major disadvantage of the conventional industrial robots is that they cannot be used in unpredictable environments such as with humans or dynamic surroundings. Even if position control is obtained with high accuracy, the safety factor should be considered in case of a collision. Additionally, they are produced with a highly stiff structure in order to tolerate vibrations and compensate for external effects on the robot. Hence, these robots are absolutely situated in well-defined and constrained working cells or workshops.

In recent years, a new generation of robots named collaborative robots have been developed to work alongside humans in order to increase work efficiency. The well-known examples are industrial coworkers, household robots, advanced prostheses and haptic applications.

Haptic term is derived from a Greek term, Haptios, relating to the sense of touch. To clarify, the senses of the human comprises from five phenomena including hearing, sight, taste, smell and touch. Haptic devices are designed to display a variable mechanical impedance to the human operator which regulates the amount of forces felt by the user respective to his/her motion. The impedance information to be displayed to the human either can be received from a telerobot in a teleoperation scenario or from a virtual reality model in a haptic virtual reality scenario.

A human's sensory system to receive sense of touch information has the most number of sensors located all around our bodies including the sensors under the skin and mechanoreceptors on our muscles and joints. According to the targeted sensor of the body different classification of haptic devices namely tactile and kinesthetic types of devices can be designed. While tactile devices are designed to stimulate the sensors under the skin, kinesthetic devices target the sensors on the joints and muscles mostly. Kinesthetic

devices are used to make the human feel the motion, forces, moment, weight and bodily position. The joint design explained in this thesis is carried out to be used for a kinesthetic type of haptic device. The main reason to select this type of haptic device is that the joint design of these devices are similar to the joints of collaborative robots that are used in industry and in the design of prosthesis.

Working principle of a kinesthetic haptic devices can be expressed through four steps. First, the motion of the physical interaction port with the user (commonly a handle) is measured. Afterwards, this information is sent to a slave robot in a teleoperation scenario or this information is converted to the digital domain to be used in a virtual reality scenario. The slave robot or a virtual object is driven with respect to this information. The interaction forces measured or calculated during the motion of the slave robot or virtual object, which is a result of physical interaction with their environment, is sent back to the haptic device. This interaction force information is displayed to the user by the energy output from the haptic device. In a general setting, electrical energy is received by the electrical actuators (i.e. electrical motors) of the haptic device, converted into mechanical energy and amplified by the help of the mechanical transmission and the links of the haptic device mechanism.

In a more concise way of explanation, haptic devices are used to stimulate our sense of touch which makes the human to be immersed in a virtual reality scenario or in the slave robot's environment. Haptics in virtual reality systems is used for increasing the virtual presence in gaming, training and education. Haptics in teleoperation systems is used to increase the level of telepresence in tele-surgical systems, teleoperation of mobile platforms and teleoperation of robots in hazardous environments.

Since a haptic device should display a range of impedance values, one of the performance metrics of a haptic device can be determined by this range. The minimum impedance is the resistance of the device to the free motion of the human. The maximum impedance is the applicable maximum resistance that can be displayed against the motion of the human. The factors affecting these measures are the frictions at the joints and inertia of the links. While the increase in the value of these factors affect minimum impedance adversely, the maximum impedance performance is improved. Therefore, the value of these factors are selected by a compromise between the minimum and maximum impedance characteristics of the device. However, it is the variability of the joint stiffness that moves the device performance from a minimum impedance range to a maximum impedance range. Commonly this is achieved by applying a suitable control to regulate

the electrical motor's output torque with respect to its motion. While the range of the impedance is dependent on the ability of the motor up to a certain level, variable stiffness joint structures are designed to increase the impedance range.

Another cluster of devices used for human-robot interfaces are collaborative industrial robots, which work alongside the human workers. They are developed under ISO 10218-1 standard in order to prevent any damage to the human coworker. First clause (5.10.1) of this standard defines a condition that no motion will be allowed if the operator is in the collaborative workspace. In the second clause (5.10.2), the robot can be moved as long as the operator gives direct force input to the robot. The next requirement (5.10.3) is related to the distance defined between the human and the robot. The operation can be achieved if this distance is not exceeded. In the final clause (5.10.5), robots having inherent force limitations are allowed to be working with the human in continuous contact because they are not capable of applying excessive forces to the operator. This task can be achieved by control, mechanical design or a combination of them (ABB, 2017).

The main difference of collaborative robots with respect to conventional ones is that a pure motion control is not sufficient due to the physical interaction taking place between the human and the robot. Thus, they should comply to their environment in order to execute their task safely. In other words, it should not apply excessive forces in the case of a physical contact with the obstacles in its environment.

These obstacles can be defined depending on their stiffness characteristics. As an example, if the robot interacts with a wall, the environment stiffness will be higher. On the other hand, if there is a human as an obstacle, the environment stiffness will be lower. Thus, the question appears as how the joint stiffness of the robot can be adjusted as the environment stiffness changes, in a similar way with human anatomy. Overcoming this issue requires the control of joint stiffness. Joint stiffness control can be achieved either actively or passively (Faulring et al., 2007).

Active joint stiffness control is based on software methods. By obtaining the force information from the end-effector with the help of sensors, the robot joint controllers are switched to a high-gain or low-gain controller. If high position accuracy is needed in some direction where there is no physical constraint, stiff actuation with a high-gain controller is preferred. Hence, if some unexpected external forces are applied to the end-effector of the robot abruptly, the robot will withstand against this effect in order to follow the predefined trajectory closely because of the stiff joint actuation arrangement. Conversely, if the high joint compliance (low joint stiffness) is required in another direction in which

there is a physical constraint, soft joint actuation with a low-gain controller is employed. In this case, if undesired external forces are exerted on the end-effector along one direction, for example tracking an irregular surface, a low gain controller can be selected for the motion along the normal of the surface. As a result of this, the position error will be higher in that specific direction than the stiff joint actuation position error to prevent significant impacts on the surface. This is the main reason why joint stiffness control is required to be applied to robots that have physical interaction with its environment. Collaborative robots and haptic systems fall into specific sub-categories of these type of robots.

Applying active joint stiffness control has some drawbacks. In these types of control designs maintaining stability is always a challenge and due to this, higher interaction forces may emerge at the end-effector of the robot. In order to overcome this issue, advanced control architectures are utilized (Salisbury et al., 1980).

On the other hand, passive joint stiffness control methods have been utilized to alter the joint stiffness either mechanically or electromechanically. They are also named as inherently compliant actuators (variable stiffness actuators) and electromechanical systems. In the systems in which the joint stiffness is regulated purely mechanically, by inserting a mechanical element (usually a spring) between the actuator and the end-effector, constant joint stiffness is defined. This joint stiffness is adjusted by applying pretension on the spring in the beginning of the application. Consequently, these actuation systems have the potential to be used only in the tasks where the stiffness of the environment is exactly known.

In the abovementioned actuation system, since the system does not contain a force sensor, the control architecture is not as complicated as active joint stiffness control, and the cost of the actuation system is decreased. Additionally, in case of unexpected collisions, it can tolerate impacts due to the use of an elastic element (spring). The most striking example is hammering task from industry. In this application, the robot is designed to insert a nail into a wood surface. If the gear based actuation system is used for this task, the reaction of the surface may give significant damages to the actuation system. Thus, the spring based actuation system is used to perform a safe operation.

Speed reduction systems (power transmission systems) usually result in a fixed joint stiffness. Traditional reduction systems with gears have backlash problem which affects the position accuracy of the robot adversely.

Capstan drive system is a common choice of a reduction system for haptic devices which also results in fixed joint stiffness. The motion is transmitted from the input shaft to the output shaft having a greater diameter than the input shaft by a cable which is wrapped around in between the input shaft and the output shaft. The main uncertainty of the design is the backlash problem (Lu et al., 2012).

Even though there are many advantages related to the fixed joint stiffness designs indicated above, the fundamental imperfection is that these actuation systems with fixed stiffness do not have the potential to change the stiffness of the joint in the course of the operation. Hence, these actuator designs are not adaptable against unpredictable environments. In other words, need for actuators with adaptable compliance have become apparent.

Actuators with adaptable joint compliance have the capacity to interact with dynamic and uncertain environments. A general approach for these type of actuators is to use an elastic element between the actuator and the joint structure, and continuously control the compression/tension on this elastic element via an additional actuator. As a result of this, while tracking a desired motion for the joint, the actuation systems stiffness can be changed. Moreover, shock absorbing property, which is obtained thanks to the elastic element, prevents a possible physical damage during a significant physical impact.

Alternative to the general approach, continuously variable transmission (CVT) systems are being used for many applications such as automotive transmissions, robotics, aerospace (Kim et al., 2002), (Faulring et al., 2007). The invention of this drive system was made by Leonardo Da Vinci in 1490. In an ideal condition, these systems have the potential to provide continuously varying power transmission within a predefined limit. This transmission is accomplished with the help of friction, belt or gear systems (Figure 1.1). One example of gear-based CVT systems is planetary gear based CVT systems (Ivanov et al., 2014). However, they are not capable of varying the stiffness independent from the output movement, because the input, which is needed to increase the output torque, is supplied from the external load.

In the same fashion, infinitely variable transmission systems (IVT) have been developed to alter the output stiffness. IVT is the modified version of CVT and also named as toroidal CVT. The working principle is same as CVT cone-drive systems that is indicated in the previous paragraph. They are mostly employed in haptic device designs (Faulring et al., 2007).

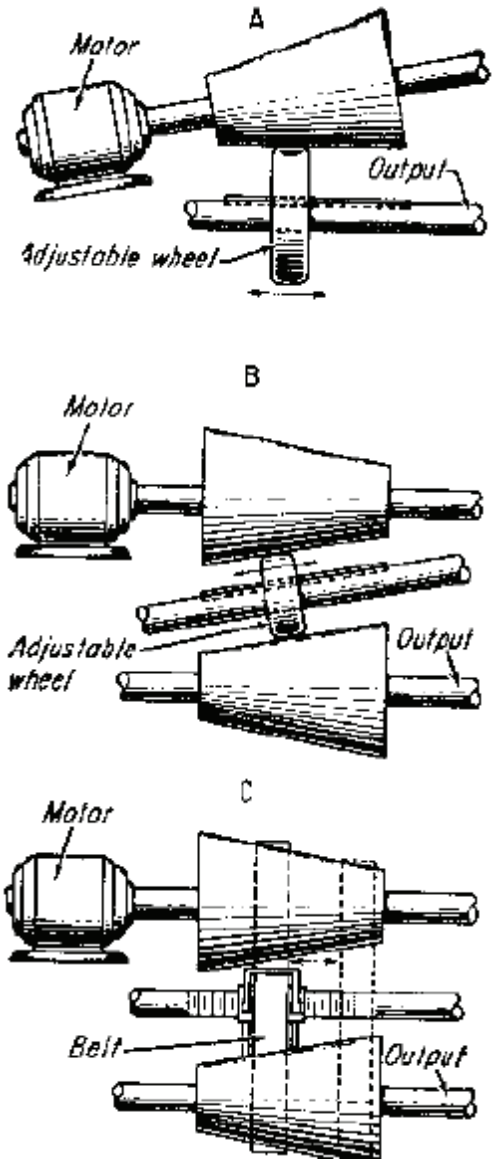

Figure 1.1. The illustration of the common two-cone CVT drives
(Source: Sclater et al., 2001)

1.1. Thesis Motivation

Until now, the actuator properties of the robots including industrial and collaborative robots are presented briefly by discussing the advantages and disadvantages. Considering the joint structures of collaborative robots, designers have certain limits to develop an actuator which has significant criteria including backdrivability, mechanical impedance, workspace, low mass and inertia, the variation of impedance without disturbing the motion, and shock absorbing (Grebenstein et al.,

2011). Good backdrivability is achieved when the resistance of the robot to the motion input by the human from the end-effector is minimized (Ishida et al., 2006). When there is a physical interaction, the robot is expected to be backdrivable so that the human-robot interaction happens in a two-way stream. The resistance mentioned above is defined as mechanical impedance which relates the resistance force to the subsequent velocity for a robot. Mechanical impedance, in short impedance, should be the maximum for enhancing accuracy and minimum for improving the backdrivability. Thus, the problem is narrowed down to the adjustment of the robot's impedance either mechanically or by control. A solution to this has been proposed in this thesis by designing a variable impedance actuation system.

Among the different variable impedance actuation systems, CVT based ones can find application in a human-robot interface if design criteria listed as backdrivability, independent output position and stiffness variation, shock absorbing and low mass and inertia are satisfied.

Even if there are various CVT designs in the literature for human-robot interfaces, the primary limitation of the two-cone drive CVT designs is that the output torque and the output position cannot be altered independently. Considering the friction drive CVT designs, the reason for this problem is that the friction wheel, which is designed to transmit the torque from the input cone to the output cone, should be moved along a linear path to vary the transmission ratio. This gives rise to remarkable longitudinal friction force along the linear path. Thus, a novel CVT is designed to overcome this limitation, and the details of the solution are presented in Chapter 3.

1.2. Aim of the Thesis

The primary purpose of this thesis is propose a new variable stiffness actuation system. This system is based on two-cone friction drive CVT, which resolves independent torque and motion problem and bidirectional torque problem.

To reach this aim, following objectives are met;

I. First prototype for proof of the concept is produced.
II. An optimization methodology based on static force analysis is proposed and implemented.
III. The final prototype of the optimized system is manufactured.

IV. The necessary tests listed below for verification of the final prototype are conducted.
   - ✓ Output force verification
   - ✓ Variation of output torque independent from the output motion tests
   - ✓ Application of bidirectional output torque tests
   - ✓ Slippage test to find the upper and lower limits of transmissible torques for determining impact absorbing range

1.3. Main Contributions

The main contribution of this thesis is to modify the well-known two-cone friction drive CVT system so that the novel CVT actuation system, which has the capability to be used for the human-robot interface, is developed.

1.4. Outline of the Thesis

In Chapter 2, the background of the stiffness control methods including passive and active approaches are introduced. In Chapter 3, the working principle of the novel CVT is explained. The kinematic analysis of the design is given in Chapter 4. In Chapter 5, the static force analysis and the design optimization methodology are discussed. In Chapter 6, the design details of the final optimized prototype and test setups are described, and the experimental verification results are presented. Finally, the results of this work are discussed and conclusions are driven by addressing future studies in Chapter 7.

CHAPTER 2

LITERATURE SURVEY

In this chapter, the literature survey of the stiffness control methods is presented. Stiffness control is divided into two main categories by Migliore et al. (2005) either actively or passively. Moreover, passive stiffness control methods are classified into two main groups by Vanderborght et al. (2013) as fixed compliance and adaptable compliance as presented in Figure 2.1.

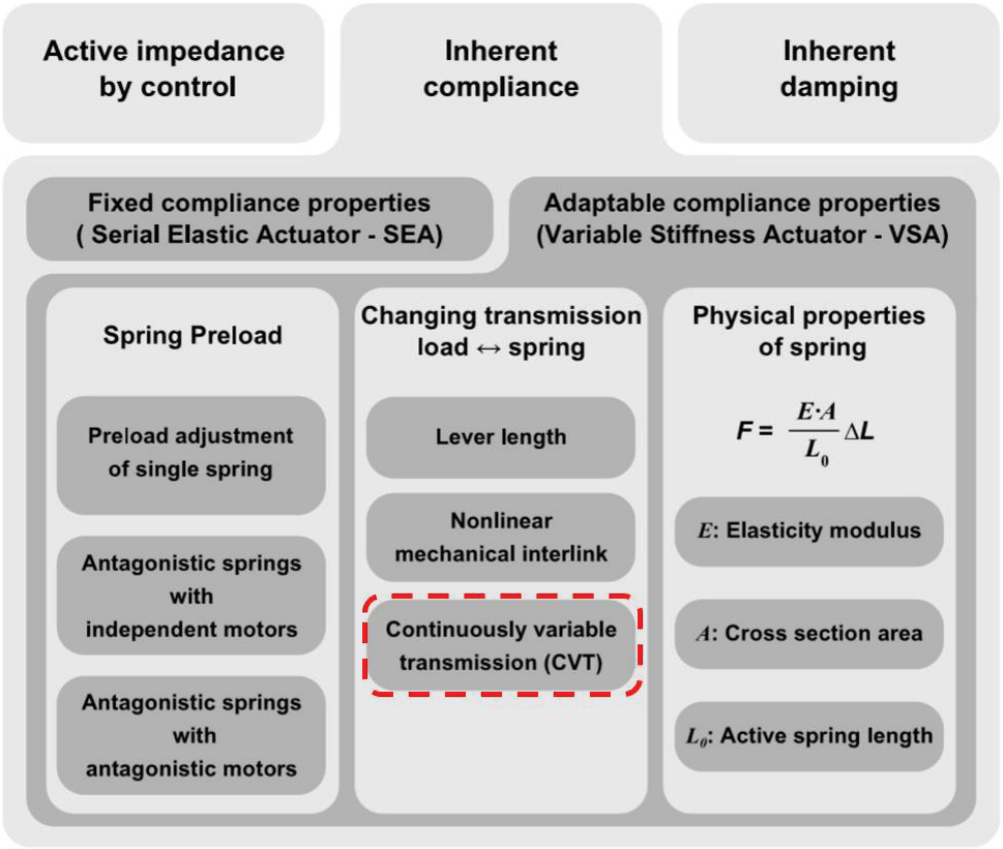

Figure 2.1. The classification of the variable impedance actuators
(Source: Vanderborght et al., 2013)

In Figure 2.1, the topic is divided into three groups as active impedance by control, inherent compliance and inherent damping. Further, inherent compliance is classified as two groups including variable stiffness actuator (VSA) and series elastic actuator (SEA).

In fact, impedance is 0^{th} order stiffness (Dede et al., 2003). The difference between impedance and stiffness is the damping and inertial effects. Hence, the classification of the joints depends upon the design and application.

2.1. Active Stiffness Control

In this category, the stiffness of the joint is adjusted with the help of a software. A compliance matrix is defined and altered depending on the task. For instance, the elements of this matrix should be assigned as larger values if the position accuracy is desired. On the contrary, the force control problem is achieved by making use of lower gains than the previous task (Dede., 2003). The prominent example for this type of control can be given from industrial robotics (Figure 2.2).

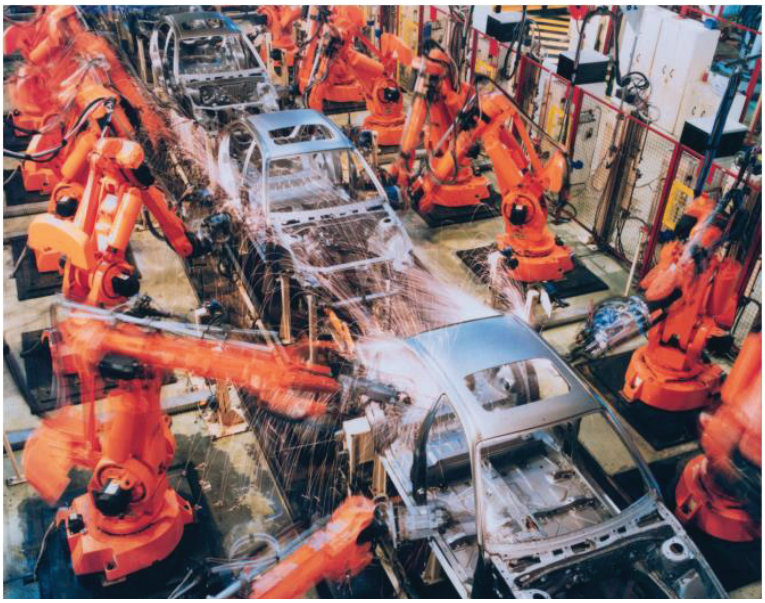

Figure 2.2. Industrial robotics used in car factories
(Source: Visser et al., 2013)

Besides, physical constraints in the environment should be considered to specify the gains. To emphasize, if there is a physical constraint in one direction, the stiffness of the joint is arranged to be lower to avoid physical impact (Salisbury et al., 1980). For example, it can be seen in Figure 2.3, there is a gripper holding the doorknob (Asada., 2016).

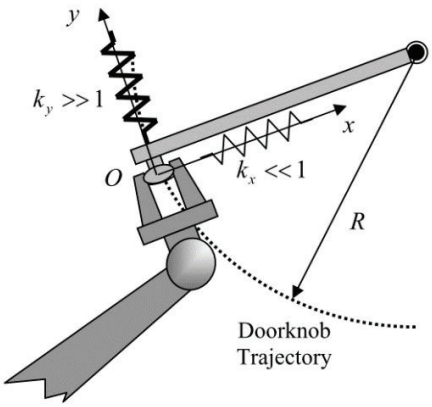

Figure 2.3. Active stiffness control task example
(Source: Asada., 2016)

In this example, it can be clearly seen that the physical constraint is along the x-direction. Therefore, the end-effector is not expected to apply excessive forces in this direction. In other words, in the x-direction, it has small stiffness and thus, high compliance. However, in the y-direction, it is the opposite. Hence, stiffness control also can be named as compliance control.

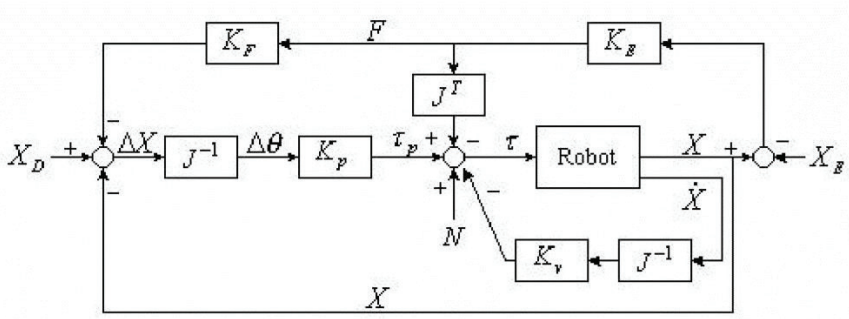

Figure 2.4. Basic principle of active stiffness control
(Source: Dede et al., 2003)

In Figure 2.4, the principle of active stiffness control employed in industrial applications is presented. K_E is the environment stiffness, K_F is the compliance term (joint stiffness), J is the Jacobian matrix, K_P and K_V are the control gains. F is the interaction force taking place between the environment and the robot. N represents the feedforward term to cancel the nonlinear effects including gravitational effects, centripetal and Coriolis forces.

In this case, K_F is defined as follows;

$$K_F = {}^{1}/_{K} \tag{1.1}$$

$$x_{modified} = FK_F \tag{1.2}$$

where K is the stiffness value. $x_{modified}$ arranges the effect of the interaction to the user. The relation between the physical and mathematical meaning can be given from the doorknob example illustrated in Figure 2.3.

Along the x-direction (Figure 2.3), joint stiffness gain is low which means that compliance is high. According to Equation 1.2, $x_{modified}$ increases since the environment is the same (F is constant). To clarify, as if the user touches a spring that the constant of it is low and the resultant displacement is high. On the other hand, in the y-direction, the stiffness is high, and compliance is low. The resultant $x_{modified}$ is lower than the first condition.

Therefore, by arranging the terms of the $\widehat{K}_F$ matrix, different stiffness values can be obtained for several degrees of freedom and environments.

2.2. Passive Stiffness Control

Passive stiffness control is sub-divided into two groups as pure mechanically or electromechanically. This category is also named as inherent compliance (Vanderborght et al., 2013). For the purely mechanical stiffness control that provides a fixed compliance, either by adding an intrinsically compliant element like springs between the end-effector and actuator or the mechanism providing a constant transfer ratio, fixed stiffness is obtained to be used for well-known environments. For the electromechanical stiffness control that provide a variable compliance, variable stiffness mechanisms are used which are capable of altering the joint stiffness as the environment changed. Therefore, these actuators have the capability to deal with different applications.

2.2.1. Fixed Compliance

The well-known example can be given as series elastic actuator (SEA) introduced at MIT (Williamson, 1995).

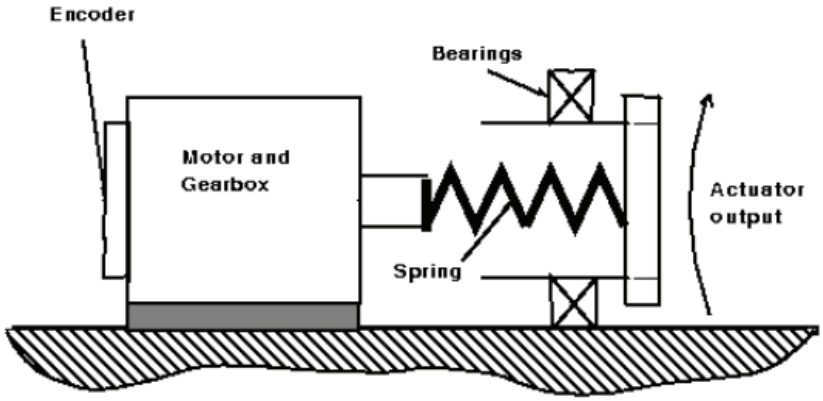

Figure 2.5. Series elastic actuator design
(Source: Williamson, 1995)

The main advantage of the design is that it is capable of absorbing impact shock thanks to spring located between the actuator and the end-effector (Figure 2.5). Also, changing the transmission is succeeded by compressing the spring with the help of motor.

Alternatively, capstan drive is preferred to be used as a fixed compliance joint (Figure 2.6). The main idea comprises from the difference of the diameters between the input shaft and the output shaft. The motion is transmitted from the input shaft, wrapped around it with cable, to the output shaft having greater diameter than input shaft. Hence, it composes a reduction and increases the force feedback capacity with low inertia and high backdrivability.

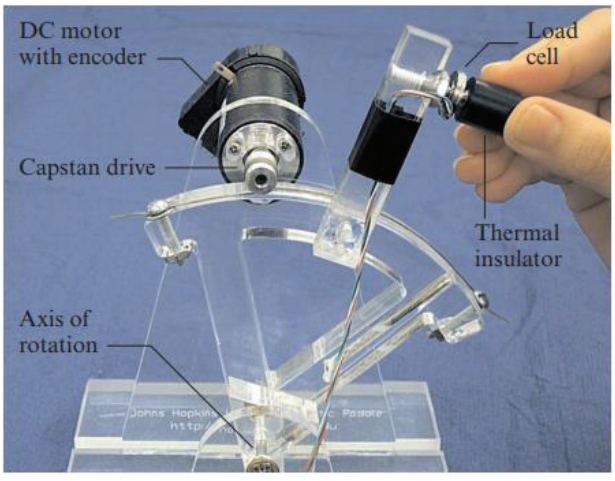

Figure 2.6. Capstan drive to be used for educational training
(Source: Okamura et al., 2005)

Most of the impedance type haptic devices are manufactured by using capstan drives in their actuation systems (Figure 2.7). Popular examples are Phantom devices Sensable Technologies (3D Systems, 2018) and haptic devices by Force dimension company (Force Dimension, 2018).

Figure 2.7. Phantom premium sensible technologies
(Source: Geomagic, 2016)

Furthermore, different combination of capstan designs are developed to be used for medical haptic applications (Li et al., 2018) as illustrated in Figure 2.8.

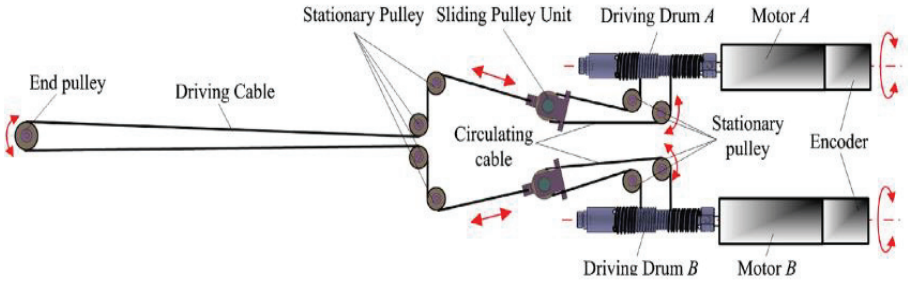

Figure 2.8. Capstan drive used in medical applications
(Source: Li et al., 2018)

2.2.2. Variable Compliance

In this section, the designs that are capable of varying the compliance with the help of mechanical ability are presented. Since the aim of the thesis is to develop a joint that has the potential to alter the compliance mechanically, the working principle and elements of these designs are investigated in detail.

2.2.2.1. Antagonistic Springs with Antagonistic Motors

In this category, all designs are capable of altering the joint stiffness and motion independently and simultaneously. Furthermore, they have shock-absorbing property in order to operate with humans or unpredictable environments.

The aim of the first design is to create net variable torque on the output shaft by changing the pretension of the linear traction spring of the novel spring device, that is, stiffness device (Figure 2.9). Even if linear traction spring is used in the device, the output stiffness results are not linear because the stiffness device is designed in such a way that rollers located at the endpoints of the springs move on the nonlinear contour (Figure 2.9).

The first advantage of the nonlinear contour (expanding contour) is to increase the output stiffness values (Migliore et al., 2005). Further, in connection with the expanding contour, the extension distance of the springs can be changed linearly or nonlinearly (Wolf et al., 2008).

In the design, there are two stiffness devices (Figure 2.9), two servo motors and pulleys on the right and left side. In the scope of this thesis, the replica of the original design is produced to understand the general principle and the requirements of the variable stiffness actuation systems. It is indicated in Figure 2.9 by (2).

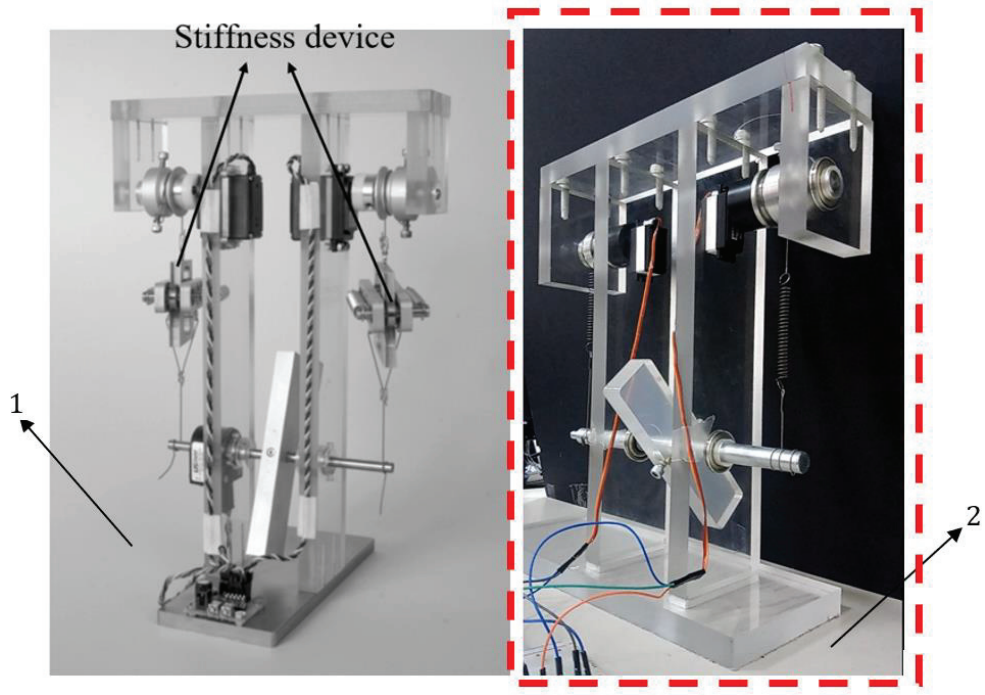

Figure 2.9. Biologically inspired joint stiffness design
(1) (Source: Migliore et al., 2005) (2) Replica of the design produced for this thesis

Working principle of the mechanism is as follows;

- Since servo motors are located reciprocally and eccentrically, position and stiffness are obtained independently. This is the main design feature of the mechanism. The top view of the design that clearly indicates the eccentricity can be seen in Figure 2.10.
- In order to alter the joint torque, motors should be rotated in the opposite direction, while to obtain output movement, motors should be rotated in the same direction.
- The connection between actuators and shaft is achieved with the help of a steel cable. The measurement of the stiffness can be achieved by disturbing the end-effector and measuring the tension of the cable at the same time. Also, the angular position should be acquired so that the deflected distance of the spring is calculated.

The reason why this design is named as antagonistic VSA is that agonist and antagonistic muscle groups are situated in arms and legs of the human body. As the position of the arms are changed without changing the stiffness, depending on the rotation direction, either agonist muscle releases and antagonist muscle contracts or the opposite one happens for counter rotation. To change the stiffness, muscles are strained and this affects the tendons around our joints. Similar principle is used for this mechanism (Laffranchi et al., 2009).

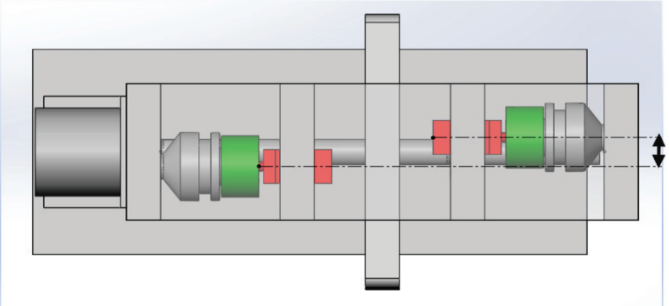

Figure 2.10. Top view of the mechanism model in Solidworks

The next version of this category is cross-coupled VSAs with antagonistic motors (Figure 2.11). The Solidworks design is presented in Figure 2.12. In this Figure, motors are represented in purple, two idle pulleys are represented in yellow, handle (output) is represented in red, third idle pulley is represented in black and timing belt is represented

in orange. Motors are position controlled backdrivable DC motors and springs are linear (Tonietti et al., 2005, Vanderborght et al., 2013).

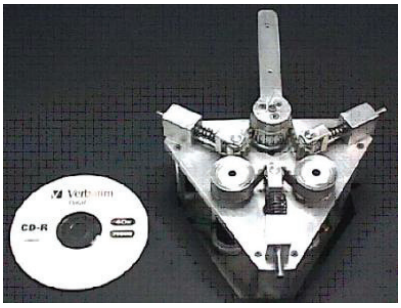

Figure 2.11. Cross couple VSA prototype
(Source: Tonietti et al., 2005)

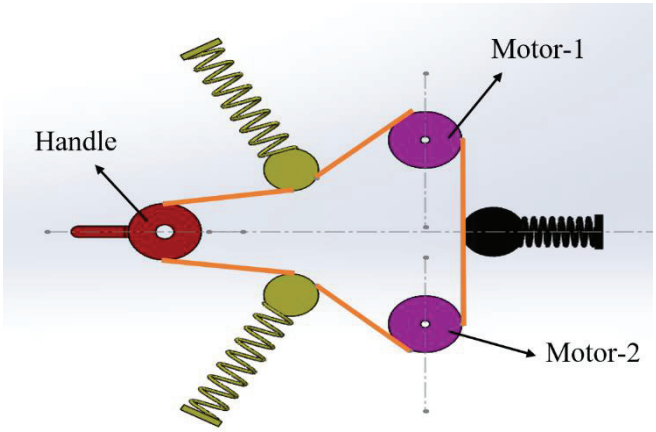

Figure 2.12. Cross coupled VSA designed in Solidworks

Working principle of the mechanism is as follows:

- Since the mechanism is named as antagonistic configuration, the main property of the design is similar to the previous design. Hence, rotation of the actuators in the same direction originates output movement, while opposite direction generates joint torque, that is, stiffness.
- When the output torque is in a minimum level, two yellow springs are not stiff. In other words, Motor-1 is rotated in CCW (counterclockwise) and Motor-2 is rotated CW (clockwise) direction. As a result of this motion, the timing belt slacks

and in order to avoid this situation, the third spring that is indicated in black is added to the system (Figure 2.12).

- To increase the stiffness, Motor-1 and Motor-2 are rotated in the opposite directions. In this case, since timing belt is not released, the third spring is not in a stiff configuration. In order to change the motion of the shaft while retaining the same stiffness, motors are rotated in the same direction.

Another example is bidirectional antagonism variable stiffness actuators (BAVS) presented in Figure 2.13. Two BAVS mechanisms are used in DLR Hand-arm system, which is presented in Figure 2.15 (Grebenstein et al., 2011).

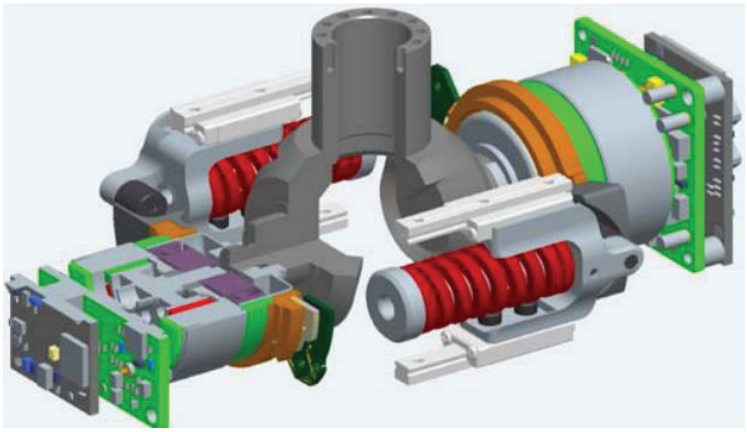

Figure 2.13. Bidirectional Antagonism Variable Stiffness Actuators (BAVS) (Source: Grebenstein et al., 2011)

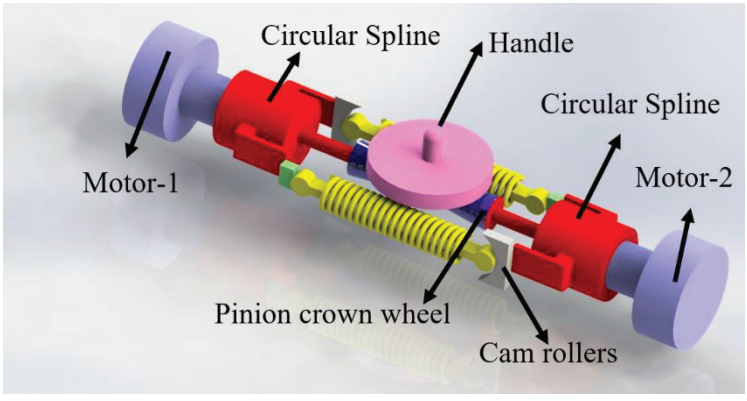

Figure 2.14. BAVS Solidworks design

In the composition of this BAVS as presented in Figure 2.14, there are two position controlled DC motors, two harmonic drives, springs, cam rollers to compress the spring, pinion crown wheel and a handle.

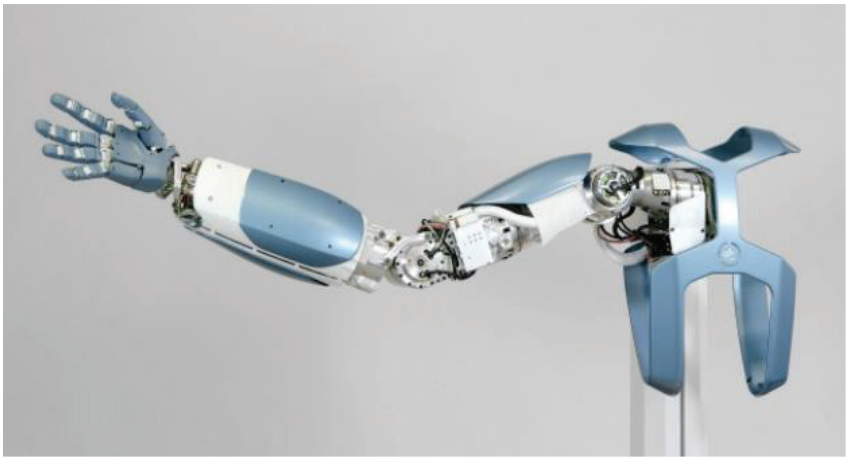

Figure 2.15. DLR Hand arm system
(Source: Grebenstein et al., 2011)

Before explaining the working principle of the mechanism, first the working principle of the harmonic drive is discussed:

Harmonic drive gear originates from three elements containing wave generator, flex spline and circular spline (Figure 2.16). In a standard setup, the wave generator has an elliptical shape and it is the input of the drive. The output can be chosen either circular spline or flex spline. Flex spline is a torsionally stiff but radially compliant element. Hence, by inserting the wave generator into the flex spline, it conforms to the elliptical shape of the wave generator. Further, as flex spline has two fewer teeth than circular spline, rotation of the wave generator leads to relative movement between the circular spline and flex spline. Therefore, as the wave generator rotates 100-times, circular spline turns 1 time due to the small teeth number difference between the circular spline and wave generator. There is numerous harmonic drive types with different transmission ratios. The suitable type can be chosen depending on the application.

There are two options to acquire different outputs. Either flex spline can be made stationary which results in obtaining the output from circular spline, or circular spline can be fixed which causes providing the output from flex spline. In the BAVS mechanism,

the first choice is preferred to change the stiffness. On the other hand; second option is utilized to alter the motion.

Working principle of the mechanism is as follows;

- The joint is designed with the principle of antagonistic configuration. Therefore, the rotation of the Motor-1 and 2 in the same sense generates output movement, while opposite rotation causes the different stiffness on the output shaft (Petit et al., 2010).

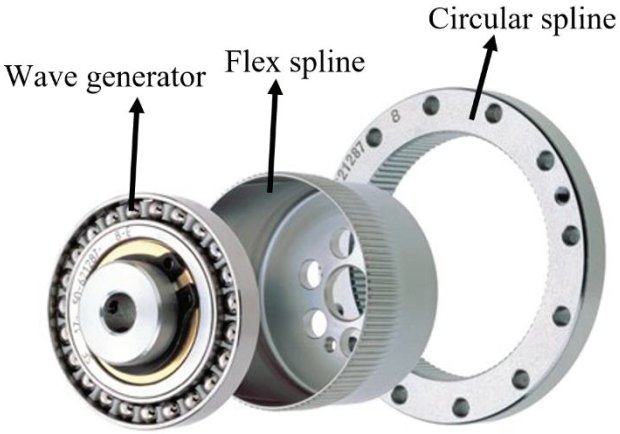

Figure 2.16. Harmonic drive
(Source: www.harmonicdrive.com)

- Springs are fixed to the ground and bedded with the help of linear bearings.
- In order to change the stiffness, rotation direction of each elements is explained via an example.

On the left side of the BAVS mechanism (Figure 2.14), Motor-1 is rotated in CCW direction, so circular spline also rotates in CCW direction because of the working principle of the harmonic drive. On the right side of the mechanism, Motor-2 is rotated in CW direction and the circular spline rotates in the same direction due to the mesh between them. During this period, since there is a pinion crown wheel, the motion of the output shaft is constrained. What happens in the course of this period is that springs are compressed by moving the linear bearing with the help of cam rollers. The level of the stiffness depends on the compression distance of the springs connected between the circular spline of the Motor-1 and 2. To summarize, when the motors are rotated in the opposite directions, the circular spline of each motor compresses the spring, and this situation gives rise to obtain a stiffer flex spline due to the mesh between them.

Subsequently, when Motor-1 and 2 are rotated in the same direction in order to change the output movement, they rotate as a higher stiffness joint. To obtain low stiffness, the opposite rotation of the motors should be applied.

The next design that is indicated as flexible antagonistic spring element (FAS) is originated from one winder (motor), two pulleys, one traction spring fixed to the base, one carrier flange and a timing belt (Figure 2.17). This design is the developed version of the cross-coupled VSA that is explained before. 19 FAS mechanisms are used in DLR Hand-arm System (Grebenstein et al., 2011). Two different operating conditions are presented in Figure 2.18.

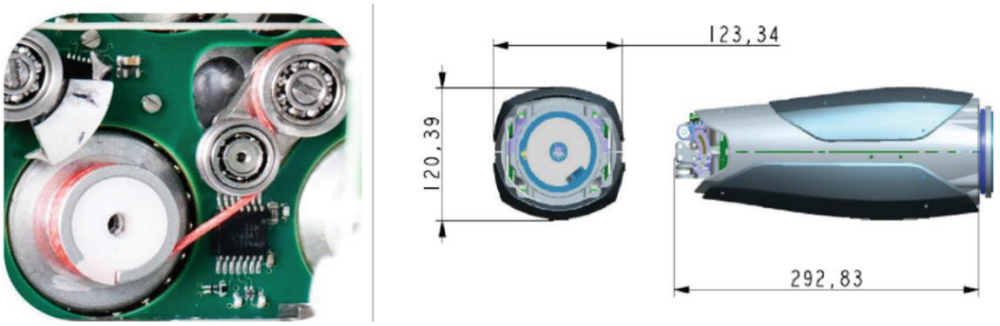

Figure 2.17. Flexible antagonistic spring (FAS) element in the arm
(Source: Grebenstein et al., 2011)

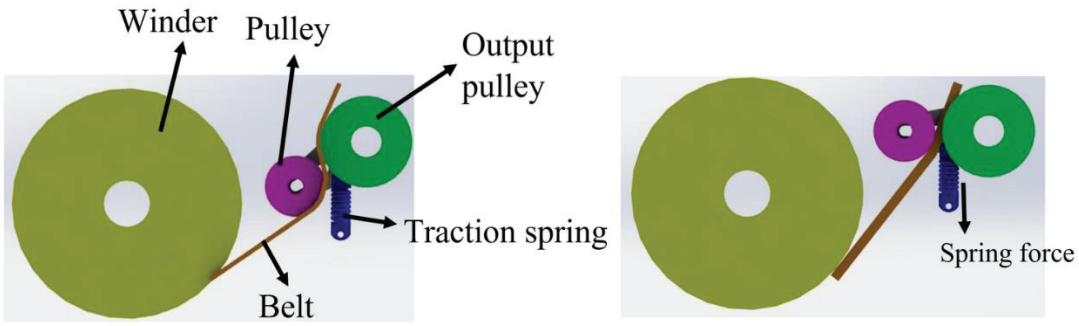

Figure 2.18. FAS Solidworks design
(a) Soft setup (b) Stiff setup

The working principle of the mechanism is as follows:

- The joint is designed with the antagonistic motor setup. Therefore, same rotation in motors results in output motion, while counter rotation alters the stiffness of the output shaft.

- To obtain low stiffness, the winder is rotated in CCW direction. Hence, the tension of the timing belt releases and carrier flange approaches to the base because of the traction spring characteristic.
- In order to increase the stiffness, the winder is rotated in CW direction. Therefore, timing belt enforces the pull on the spring and tension of the timing belt rises.

2.2.2.2. Antagonistic Springs with Independent Motors

In this category, the stiffness and the motion variation is supplied with the help of two motors that are uncoupled from each other. In other words, there is no shared mechanism to connect them to each other.

In the first design, a harmonic drive is used for transmission. In addition, the variable stiffness mechanism is located between the harmonic drive gear and joint base to increase or decrease the stiffness and accomplish safe human-robot interaction.

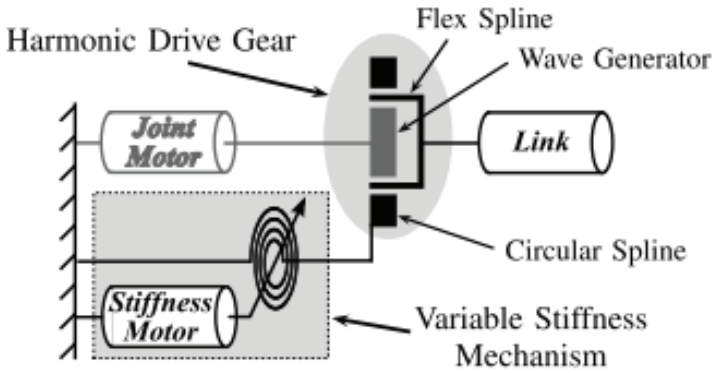

Figure 2.19. Variable stiffness (VS) joint elements
(Source: WOLF et al., 2008)

In Figure 2.19, there are two motors. First one is stiffness motor, which is smaller and lighter than the other motor that is responsible for the joint motion variation. Furthermore, the mechanism is capable of altering joint motion and stiffness, independently. In another design, there are cam discs and cam rollers in order to vary the stiffness by moving linearly through linear bearings. This design can be seen in Figure 2.20. The working principle of the design is as follows:

- In general setup, the circular spline in the harmonic gear is fixed. However, in this design, the circular spline is rotated and flex spline is fixed.
- To alter the stiffness, stiffness motor rotates with the circular spline and cam disc, as they are fixed to each other. Subsequently, since cam rollers roll on the cam disc, it compresses the spring by moving linearly. Hence, it applies force to the flex spline due to the mesh between them and renders a stiffer joint. This movement is named as translational deflection which can be observed in Figure 2.20. This is the procedure for stiffness variation.
- To alter the output motion, the joint motor is rotated without disturbing the output stiffness.

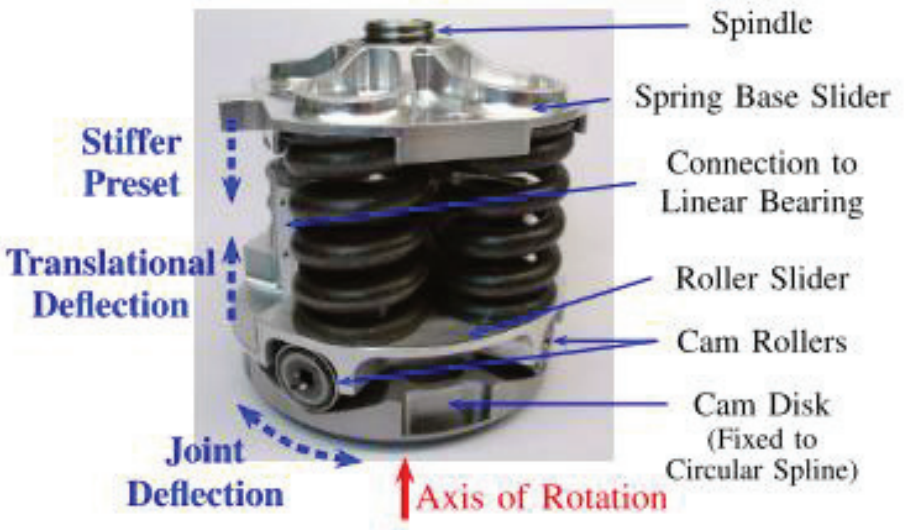

Figure 2.20. VS Joint Mechanism
(Source: WOLF et al., 2008)

2.2.2.3. Lever Length Type of VSA Joint

In this design, two position-controlled DC motors are used (Figure 2.21). Two linear springs are used to change the translational stiffness (Visser., 2013). Working principle of the mechanism is investigated as follows;

If the motor is driven along q_1, translational stiffness is altered (Figure 2.22). On the other hand, q_2 is used to achieve the variation of the output motion. To clarify, the decrease of q_1 results in the increment of the output stiffness as the moment taking place

around A is at significant level. On the contrary, the minimum stiffness is acquired if q_1 is maximized.

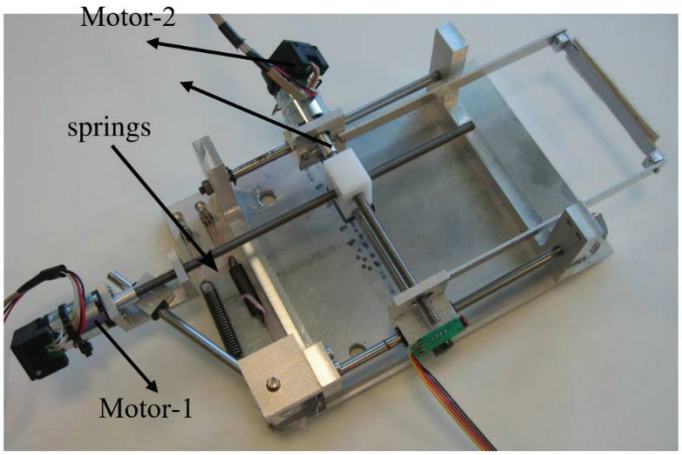

Figure 2.21. Lever length variable stiffness actuator
(Source: Visser et al., 2013)

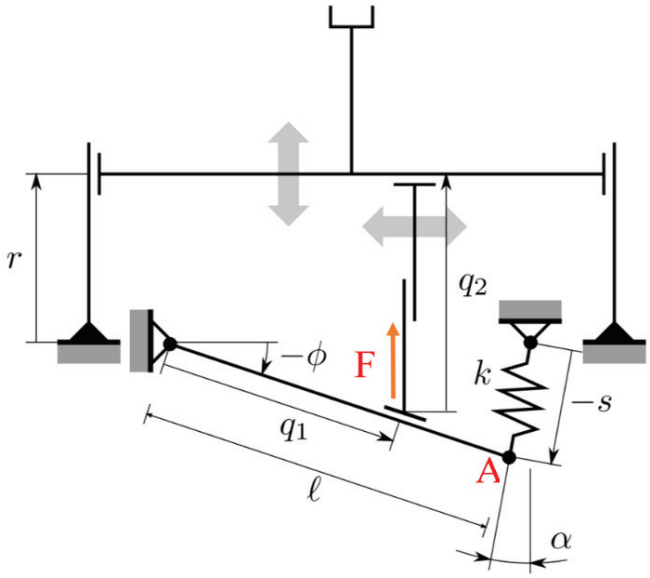

Figure 2.22. Conceptual design of the lever length variable stiffness actuator
(Source: Visser et al., 2013)

2.2.2.4. Continuously Variable Transmission (CVT)

Finally, CVT designs are examined in this section. The main motivation of these systems is to acquire stepless torque variation within a predefined limit.

The first design is based on planetary gears (Ivanov et al., 2012). The design is also named as the adaptive reducer (Figure 2.23). The mechanism comprises two parts as input and output carriers. Input carrier is named as H_1 and output is H_2 in Figure 2.25. To understand the operation principle of the mechanism clearly, the significant elements of the design is drawn in Solidworks and illustrated in Figure 2.24. The input and output carriers are indicated in yellow in Figure 2.24. The electric motor is represented in green, electric generator (it applies an external load to the output shaft) is represented in blue, shaft gear is represented in purple, satellite-2 (planet) is represented in brown in input part and satellite-5 is represented in pink colors in output part.

The kinetic energy of the rotating parts are calculated by $\frac{1}{2}I\omega^2$. In this equation, I is the inertia, and ω is the angular speed. So, if the mass is added to the system, the moment of inertia and kinetic energy are increased, simultaneously. The reason why this detail indicated is that there is an extra mass around wheel-3 which can be seen in Figure 2.25. In other words, this wheel acts as a flywheel.

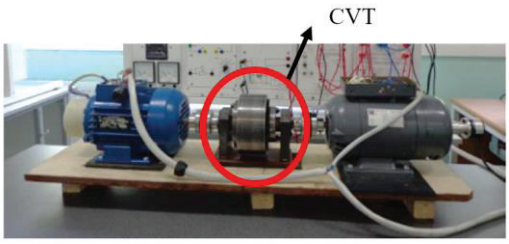

Figure 2.23. CVT mechanism experiment setup
(Source: IVANOV et al., 2014)

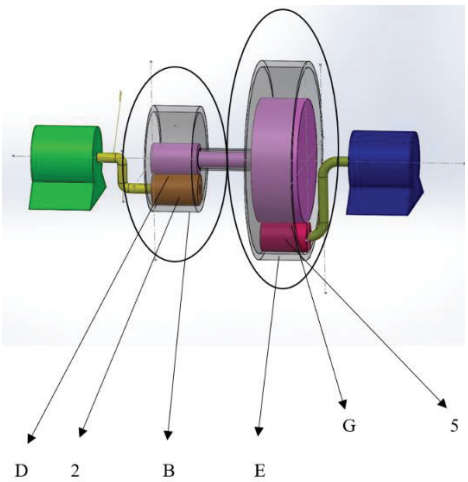

Figure 2.24. Solidworks drawing of the reducer

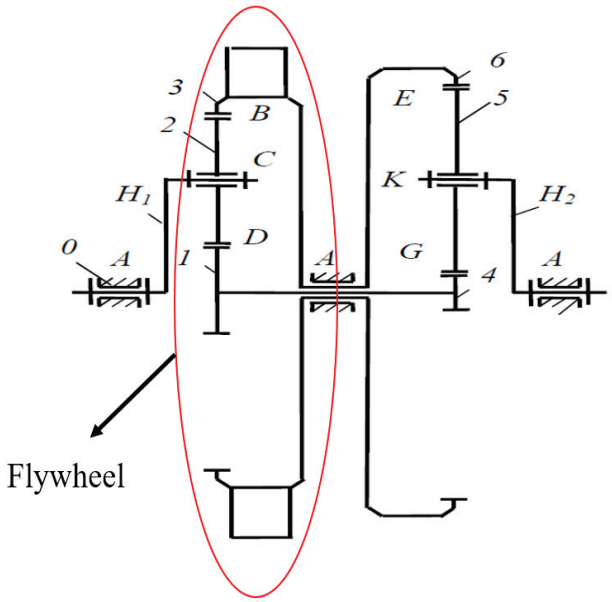

Figure 2.25. CVT mechanism
(Source: IVANOV et al., 2014)

This adaptive drive has three working conditions which are the start-up, operating and stopped. In the start-up condition, the electric motor is rotated from zero speed to the desired value. How this motion happens and the details of the operation step-by-step are stated as follows:

- M_{H1} (input torque of the motor) is applied by the motor to the carrier H_1.
- Planet-2 enforces to rotate the ring-3 and sun-1, but these wheels also have a connection at the output part. Since the output-part radii of the wheels are designed greater than the input part, it creates resistance (reaction force) and does not permit internal motion in the reducer.
- The system starts to rotate as a whole. It can be thought that as if the internal connection of the reducer (point G, E, B, D) is welded to each other. Hence, input carrier speed (ω_{H1}) is equal to output carrier speed (ω_{H2}) and also the moments are equal to each other ($M_{H1} = M_{H2}$).
- In fact, the system has two degrees of freedom. However, by adding one constraint, the system is left with one degree of freedom. So, by using one input given from the electric motor, calculations can be made.

This interval continues until the system reaches a certain speed and torque. During this operation, the system accumulates the kinetic energy. If the load is applied to the system

without waiting for this start-up regime, the system will just be stopped due to the low energy. One of the examples can be given from the industry for this situation. When an eccentric press machine is initiated, the operator should wait for a certain amount of time. During this interval, flywheel of the press accumulates the energy. If the operator does not wait, the press applies pressure to the part but cannot complete its work and locks itself. The same situation happens for adaptive reducer at the start-up regime.

In operating regime:

- Output resistance (external load) is increased gradually by the electric generator without changing the electric motor (input) torque. Hence, the constraint applied in start-up regime is removed.
- By giving two inputs (electric motor and electric generator), the mechanism becomes two degrees of freedom, and relative internal motion starts in the reducer.
- Until certain output resistance, adaptive reducer accomplishes adaptation to the external load.
- If the load value exceeds this output resistance, the stopped regime starts and details of this interval are stated below;

In stopping regime;

- In operating regime, planet-5 was translating and rotating. However, in the stopping regime, it cannot translate due to the overload on the output carrier. Therefore, planet-5 only rotates about its axis as idle. The angular velocity of the planet-5 increases because it is not able to consume energy for translation.
- Since the velocity of planet-5 increases, the velocity of the sun 1-4 and ring 3-6 also reach a significant value. However, input speed and moment remain constant.
- Planet-2 still rotates and translates around sun-1 by increasing the rotation velocity. The translating velocity of planet-2 remains constant due to the constant input speed of the electric motor.
- By achieving this operation, the system does not lock itself against the overload.

The next CVT design is named cobot which is designed to be used in haptic applications (Faulring et al., 2007) (Figure 2.26). Variation of the stiffness is based on friction drive method.

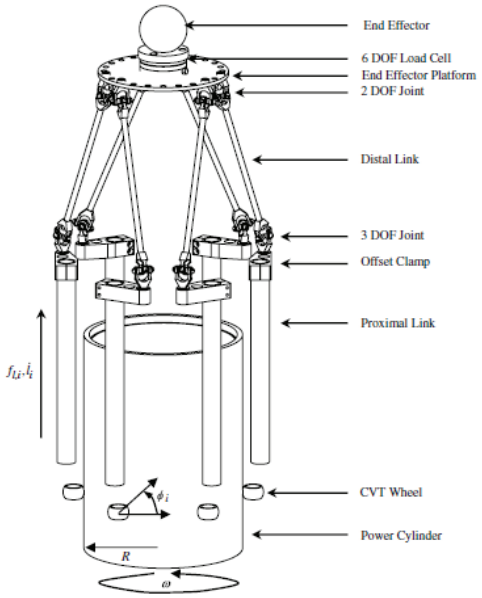

Figure 2.26. Cobotic hand design
(Source: Faulring et al., 2007)

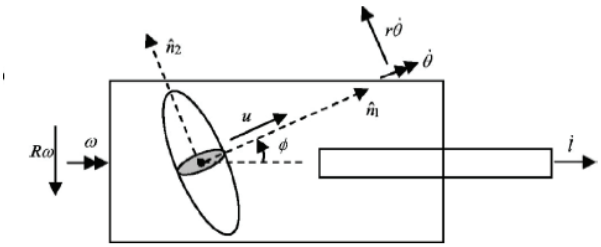

Figure 2.27. Side view of the CVT wheel
(Source: Faulring et al., 2007)

The working principle of the mechanism is stated below:

- CVT wheels have two degrees of freedom which are roll and yaw as indicated in Figure 2.27.
- The proximal link is translated by means of a carriage either along the upwards or downwards direction.

- When stiffness variation is required, power cylinder is rotated, and CVT wheels are steered depending on the desired stiffness. So, the variation of the stiffness is achieved by altering the ϕ angle.
- If $\phi = 0$ is adjusted, the proximal link will be locked and translational motion stopped due to the frictional wheel design. On the other hand, if $\phi = \frac{\pi}{2}$ is arranged, the proximal link will decouple entirely from the power cylinder. Hence, by avoiding the arrangement of $\phi = \frac{\pi}{2}$, desired stiffness is acquired.

Additionally, spherical continuously variable transmission (S-CVT) is one of the examples of CVT design (Kim et al., 2002). In this work, two input discs, two output discs and one variator provided friction surfaces are connected with the sphere in order to adjust the stiffness of the output discs by the help of friction force (Figure 2.28).

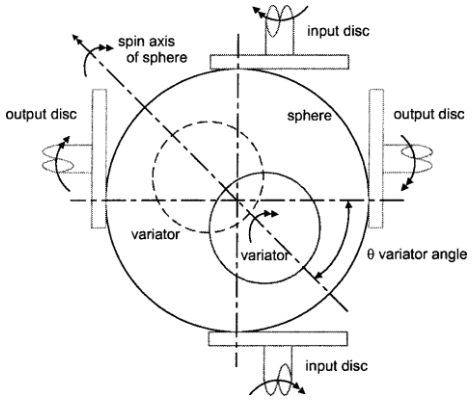

Figure 2.28. Spherical continuously variable transmission
(Source: Kim et al., 2002)

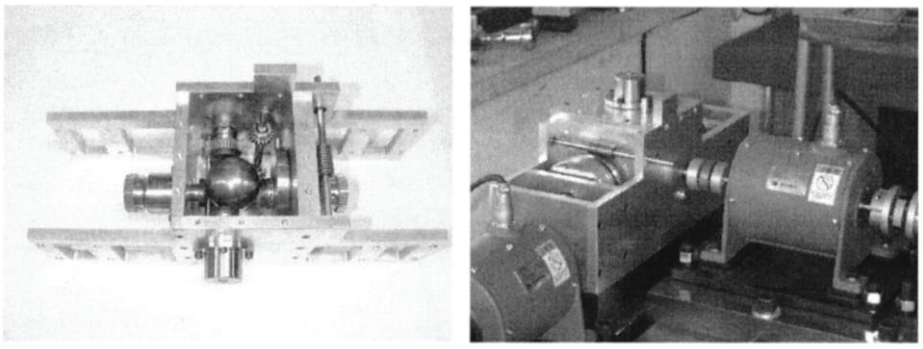

Figure 2.29. Spherical continuously variable transmission test bench
(Source: Kim et al., 2002)

Input and output discs have point type of contact with a sphere. By adjusting the location of the rotation axis of the sphere, output velocity and output torque are altered (Figure 2.29).

2.3. Conclusion

In this chapter, different types of variable stiffness joint designs found in the literature are examined. Their advantages and disadvantages are exploited. The primary advantage of the biologically inspired antagonistic springs with antagonistic motors type of joint design is that without using the current control in motor and feedback loop, joint stiffness and joint angle are changed independently with the help of mechanical stiffness device (Migliore et al., 2005). Moreover, the open-loop control algorithm is used, and the mechanism has the potential to absorb impacts in order to achieve safely human-robot interaction. Since stiffness is obtained passively, stability is guaranteed. On the other hand, the joint motion is limited due to the servo motors. Furthermore, because of the friction in the stiffness device, some part of the energy input via servomotors are dissipated. Thus, it limits the maximum joint torque. In addition, since the spring is utilized in the stiffness device, modelling the system is challenging due to the nonlinear characteristic of the spring.

The main advantage of the Cross-Coupled VSA design is that it has the capability to work unlimited operating range. However, the timing belt is connected continuously with pulleys and motors (Tonietti et al., 2005, and Vanderborght et al., 2013). Also, all forces act on it. Hence, it should be replaced with a new one after some period of use.

The fundamental advantage of BAVS is that since the harmonic drive is used for transmission, high torques can be obtained. Furthermore, the connection of the output shaft and handle is provided with the help of pinion crown wheel system. As a disadvantage, against the unexpected impacts, the harmonic drive is not resistant (Ishida et al., 2006). Further, pinion crown wheel system adds extra inertia on the mechanism. Hence, it affects the backdrivability, negatively (Ishida et al., 2006). Besides, transferring the force direction by 90° with the help of pinion crown wheel may give rise to issues for some tasks. In other words, the axis of the motors and the output shaft are not located along the same axis.

Antagonistic springs with independent motors, has shock-absorbing feature due to the spring located between the joint and base. Furthermore, it is smaller than previous designs, so it has the capacity to be utilized in many applications (Wolf et al., 2008, and Grebenstein et al., 2011). On the other hand, since the stiffness motor is located in the joint, it creates extra inertia. Therefore, backdrivability property is affected, negatively.

Additionally, lever length type of variable stiffness joint design has shock-absorbing feature and independent position-stiffness property. Furthermore, it has a relatively simple mechanical design. However, since the distance, which is named as moment length, between the connection point of the nut screw and bedding is located far away from the rotation axis, reaction forces bend the screw nut. Therefore, it does not allow stretching the springs correctly. Hence, ϕ angle (Figure 2.22) cannot be adjusted precisely (Visser et al., 2011). Finally, since the mechanism occupies a larger volume than the other designs, it does not have the capability to be used in a wide variety of tasks such as humanoid robot joints.

Planetary gear based CVT design has the potential to alter the stiffness mechanically. Additionally, against the overload, the system has stopped regime and this feature protects the joint inherently. Moreover, the mechanical design is simpler than spring based variable stiffness joints. Therefore, it is easy to obtain force and kinematic analysis of the system. On the other hand, stiffness and position cannot be altered independently as one of the inputs of the system is output resistance. However, in previous designs, which are produced with antagonistic configuration have a property of obtaining the stiffness variation independent from the output resistance. Moreover, since the mechanism is produced from a planetary gear system, the inertia of the wheels is greater than previous designs. Therefore, the user feels those effects while handling the handle for a haptic application or in prosthesis application.

The IVT mechanism is capable of transforming the rotational transmission to the linear transmission. Nevertheless, the steering wheel should be controlled precisely to obtain the exact stiffness output (Kim et al., 2002). Furthermore, the power cylinder makes the design bulky because of volume. Also, the whole cobot is carried by the CVT wheels. Therefore, bearings located in the wheels are forced under the cobot weight and dynamic effects in the course of operation.

To summarize, the novel CVT presented in this thesis is developed to overcome the abovementioned limitations. The detailed working principle of the new design is discussed in the next chapter.

CHAPTER 3

WORKING PRINCIPLE OF THE NOVEL CVT

In this chapter, the working principle of the novel CVT design, the design details and the experimental study that is conducted to prove the working principle of the design are presented.

In conventional friction-drive two-cone CVTs, there are two cones which are covered with friction material, and a wheel is used to transmit the moment from one cone to the other. Moment and speed transmission levels are altered by changing the ratio of the radii of the input and output cones in contact with the wheel by varying the position of contact of the wheel. However, it is not possible to control output position and output torque independently in this way since the wheel does not have the capability to perform the holonomic motion. In other words, the cones must be rotated to change the transmission ratio, and this situation limits the usability of the two-cone CVT drive in human-robot interfaces.

To cope with this issue, the first modification is made by using a sphere, which is capable of executing holonomic motion, as the transmission element instead of the wheel (Figure 3.1). Hence, point type of contact with two cones is guaranteed which allowed controlling output position and output torque independently. Also, the cones are covered with a rubber surface made from diaphragm to create friction surfaces on the cones to avoid slippage without applying the larger amount of normal force on the cones.

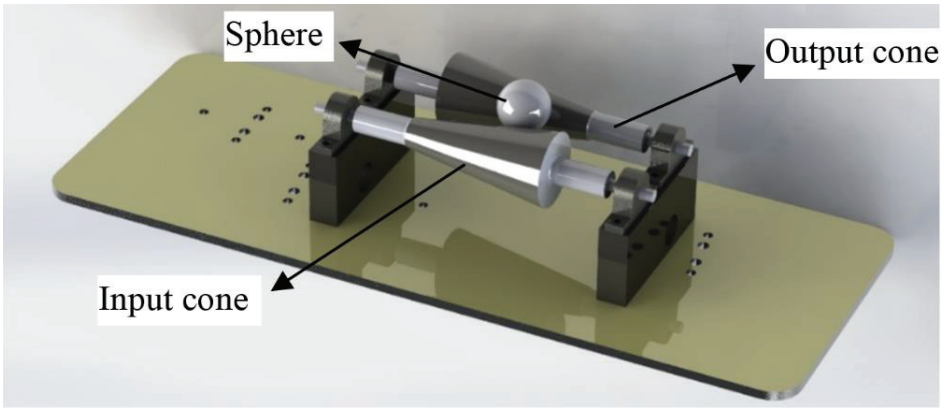

Figure 3.1. Isometric view of the single-sphere two-cone CVT

The location of the spheres is important for the shifting action which accomplishes alteration of the transmission ratio. If the sphere is located exactly between two cones, it is not possible to change the transmission ratio without changing the output position. The proof of this problem is presented in Figure 3.2.

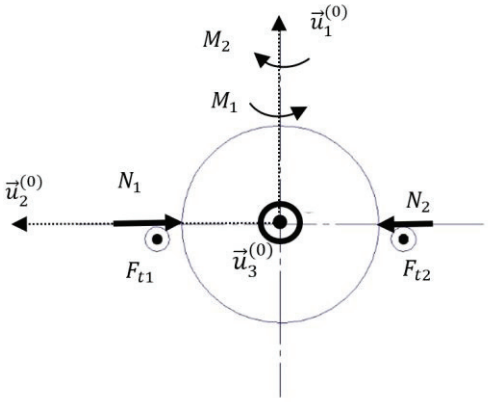

N_1: Normal force applied by the input cone
N_2: Normal force applied by the output cone
F_{t2}: Tangential force acting on the right side of the sphere and belonging along the longitudinal direction
F_{t1}: Tangential force acting on the left side of the sphere and belonging along the longitudinal direction
F_1: Spring force acting on the upper sphere
F_1: Spring force acting on the lower sphere
r: radius of the sphere

Figure 3.2. Free-body diagram of the sphere located between the cones

$$\vec{M}_1 = r\vec{u}_2^{(0)} \times F_{t1}\vec{u}_3^{(0)} = F_{t1}r\vec{u}_1^{(0)} \tag{3.1}$$

$$\vec{M}_2 = -r\vec{u}_2^{(0)} \times F_{t2}\vec{u}_3^{(0)} = -F_{t2}r\vec{u}_1^{(0)} \tag{3.2}$$

Tangential forces are equal to each other since the normal forces and friction coefficient are the same for the two cones which makes $\vec{M}_1 = \vec{M}_2$ in Equations 3.1 and 3.2. Therefore, the sphere cannot roll around $\vec{u}_1^{(0)}$ axis, and it needs to slip between the two cones in order to change the transmission ratio. However, slip between the cones and the transmission element is not desired in order to guarantee the transmission within the selected limit value of applied torques from the input cone. For this reason, the sphere should be able to roll instead of a pure slippage, and thus, the sphere is located above the cones. The mathematical proof of the rolling action of the sphere is shown by Equation 3.3 and 3.4 based on the free-body diagram of the sphere above the cones presented in Figure 3.3.

The angle between the frames $\mathcal{F}_0$ and $\mathcal{F}_1$, and $\mathcal{F}_0$ and $\mathcal{F}_2$ are defined as $\measuredangle\, \vec{u}_1^{(0)} \rightarrow \vec{u}_1^{(1)} = \frac{\pi}{2} - \beta_1$ and $\measuredangle\, \vec{u}_1^{(0)} \rightarrow \vec{u}_1^{(2)} = \frac{\pi}{2} + \beta_2$. Based on this definition, the moments that occur due to the friction forces in the opposite direction of the shifting force are calculated in Equation 3.3 and 3.4.

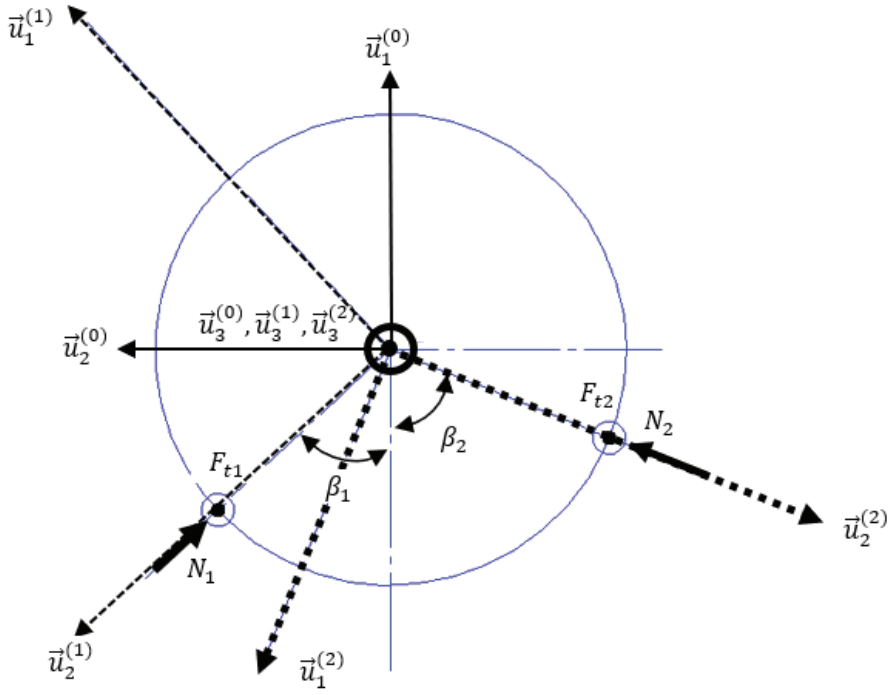

Figure 3.3. Free-body diagram of the sphere located above the cones

$$\vec{M}_1 = r\vec{u}_2^{(1)} \times F_{t1}\vec{u}_3^{(1)} = F_{t1} r \vec{u}_1^{(1)} \tag{3.3}$$

$$\vec{M}_2 = r\vec{u}_2^{(2)} \times F_{t2}\vec{u}_3^{(2)} = F_{t2} r \vec{u}_1^{(2)} \tag{3.4}$$

The above vector equations can be resolved in the inertial frame $\mathcal{F}_0$ as presented in Equations 3.5 and 3.6. It should be noted that; $\hat{C}^{(0,i)}$ is the transformation matrix between the inertial frame and the i^{th} frame, $\tilde{u}_3$ resembles the skew-symmetric matrix form of the $\bar{u}_3$ column matrix.

$$\bar{M}_1^{(0)} = \hat{C}^{(0,1)} \bar{M}_1^{(1)} = F_{t1} r e^{\tilde{u}_3 (90-\beta_1)} \bar{u}_1 = F_{t1} r [\bar{u}_1 \sin\beta_1 + \bar{u}_2 \cos\beta_1] \tag{3.5}$$

$$\bar{M}_2^{(0)} = \hat{C}^{(0,2)} \bar{M}_2^{(2)} = F_{t2} r e^{\tilde{u}_3 (90+\beta_2)} \bar{u}_1 = F_{t2} r [-\bar{u}_1 \sin\beta_2 + \bar{u}_2 \cos\beta_2] \tag{3.6}$$

When Equations 3.5 and 3.6 are investigated, it is obvious that $\vec{u}_2$ component of the moments makes the sphere to roll on the cones and $\vec{u}_1$ component of the moments act against each other to prevent the rotation around $\vec{u}_1$. Therefore, it is possible to move the transmission element without the necessity of slippage, and this is the reason why the sphere must be located above the cones.

Nevertheless, relocation of the sphere above the cones does not fully solve the problem. In order to explain the new problems, Figures 3.4 and 3.5 are drawn. In Figure 3.4, it is assumed that there is a handle coupled with the output cone and the user holds

it. When the input is in CW direction, the transmission is achieved as indicated in Figure 3.4. The friction forces acting on the sphere during transmission is the downward direction (P_1, P_2) and hence, the transmission without slippage is guaranteed up to a certain limit. For the other case in which the input is in CCW direction as presented in Figure 3.5, transmission cannot be guaranteed since the friction forces acting on the sphere (P_3, P_4) are upward and this reduces the normal force between the sphere and the cones ("W" is a weight of the sphere). This situation results in slippage at the point of contact at lower ranges of transmission torque value. In order to propose a solution to this problem, a second sphere below the cones is added to the system. Also, as presented in Figure 3.6, two additional forces are used to apply pre-tension (F_1, F_2) to each sphere guaranteeing the same amount of normal force on each sphere in order to solve the bidirectional transmission problem.

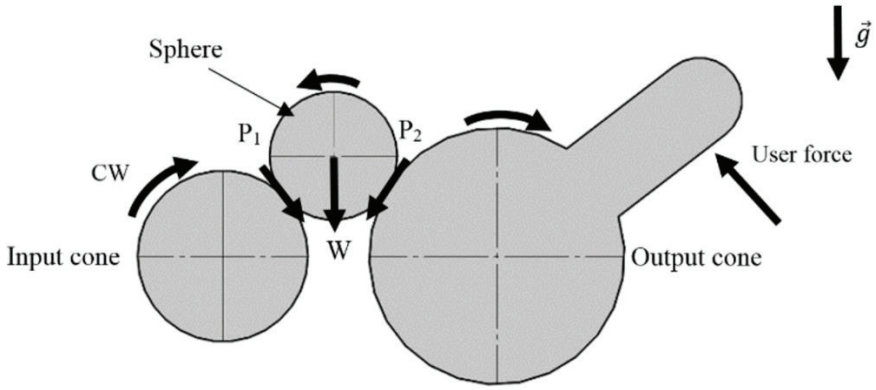

Figure 3.4. Side view of the one transmission point for CW direction

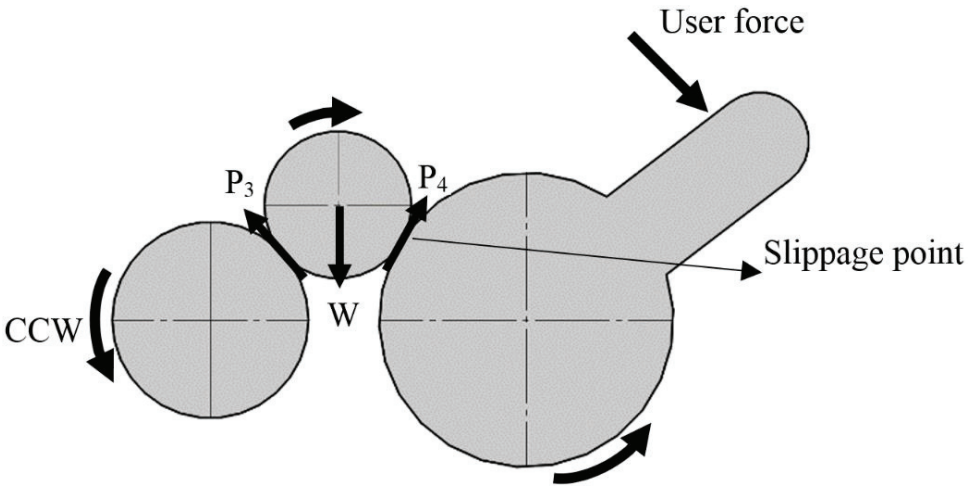

Figure 3.5. Side view of the one transmission point for CCW direction

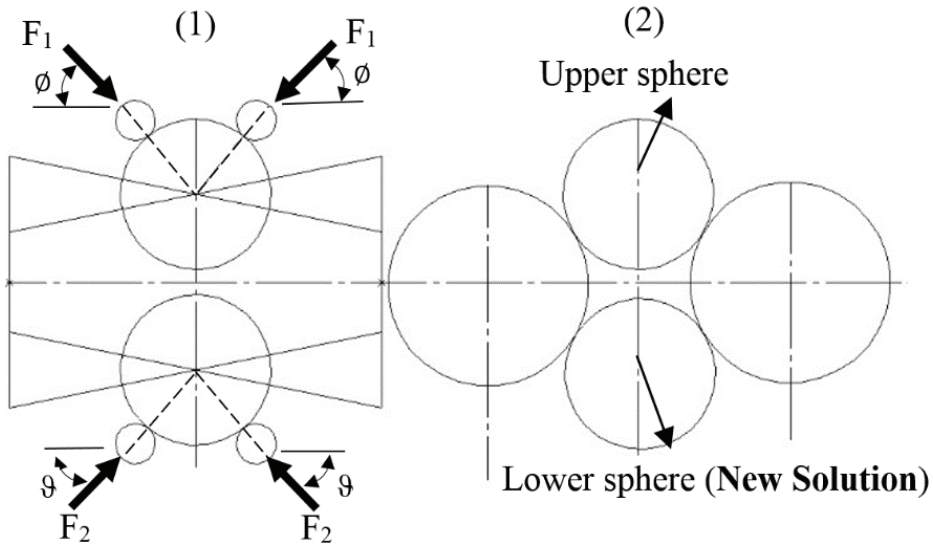

Figure 3.6. Double-sphere CVT (1) Front view (2) Side view

3.1. Proof of the Concept Design

The design details of the novel CVT (Figure 3.7) are presented in this section in order to be used for manufacturing a prototype for proof of the design tests.

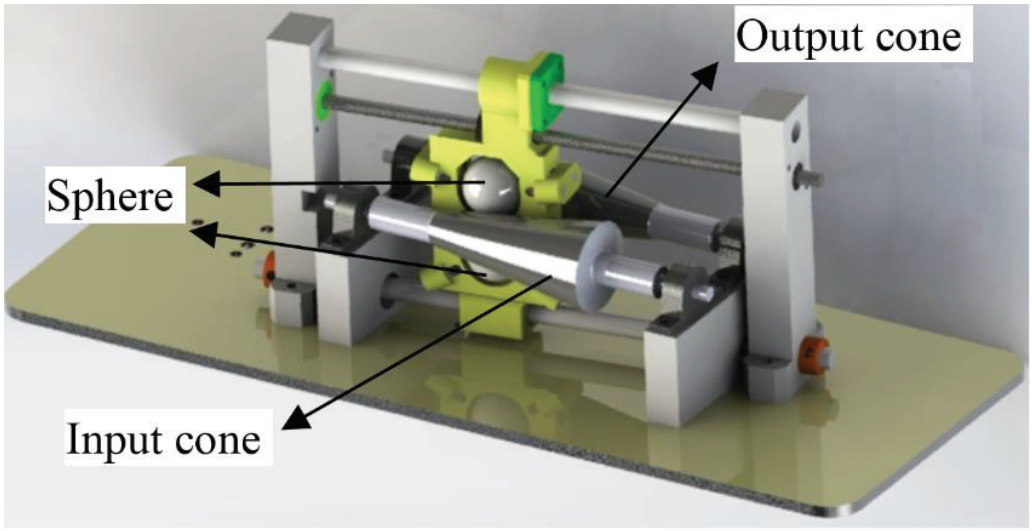

Figure 3.7. Isometric view of the double-sphere two-cone CVT

First, the exploded view of the carriage system, which is used for carrying the two spheres that alter the transmission ratio, is indicated in Figure 3.8.

In this design, there are a total of 8 parts as follows: compression springs **(6)**, support elements **(5)**, four pieces steel pins **(4)** and bearings **(3)**, two pieces steel spheres **(1,2)** and the carriage **(8)**. In the assembly process, first, upper and lower spheres are placed into the sphere cavities, and the bearings are placed into the slots. Following this, steel pins are mounted through the bearings holes so that the spheres can be confined in the carriage. The next step is related to the application of pre-tension on the spheres. Two support elements are located at the back of the steel pins, and springs are placed at the back to the aforementioned support elements. Finally, a set-screw **(7)** is mounted on the spring so that the pretension of the spring can be altered.

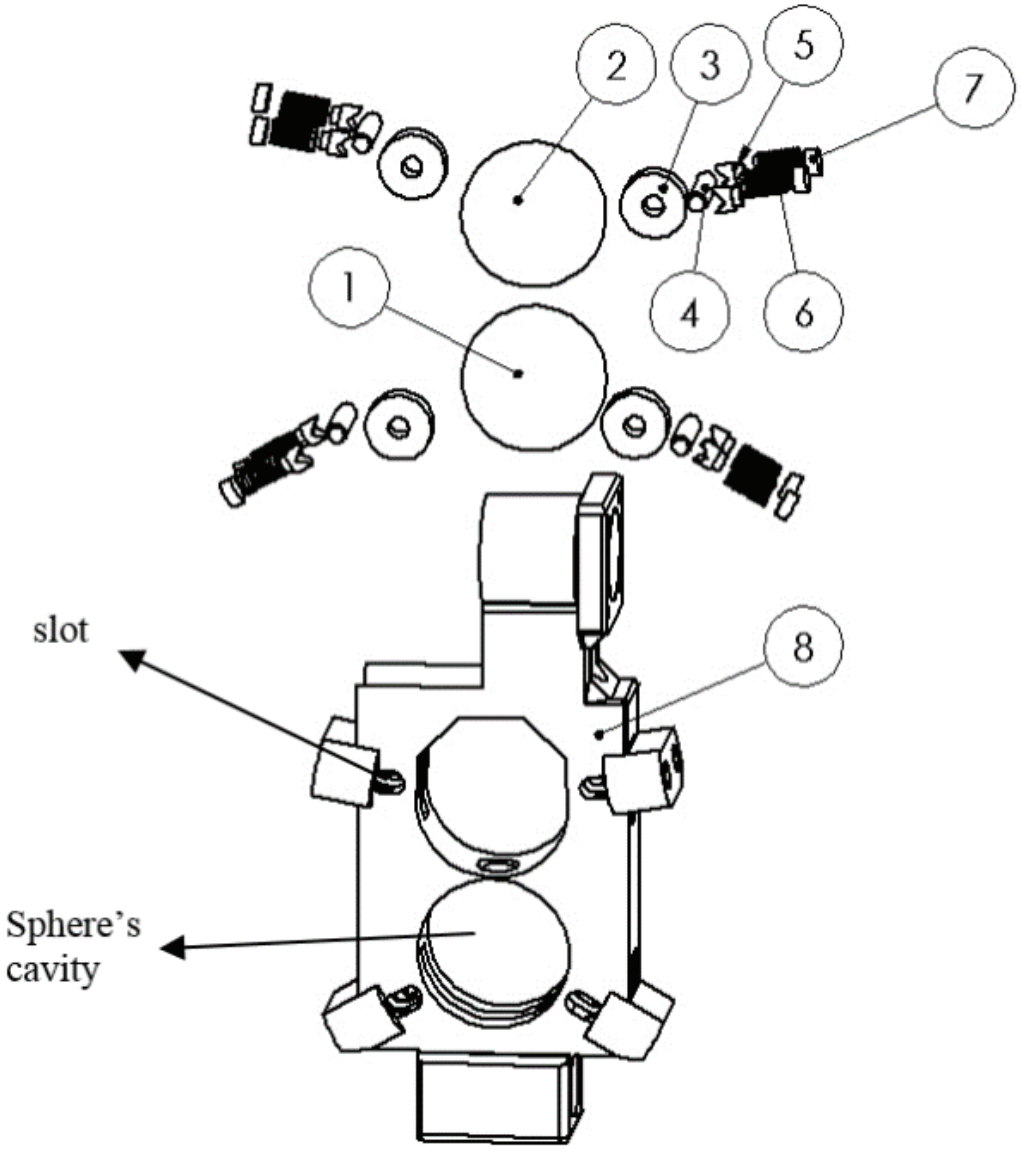

Figure 3.8. Exploded view of the carriage system

After assembling the carriage system, the carriage system is assembled on a screw-nut system **(11)** and linear guides **(9)** at the upper and lower part of the carriage system as shown in Figure 3.9. The cones are denoted as **(10)** and the bedding pieces for the cones and the carriage's linear guides are denoted as **(12)** , and **(13)** respectively in Figure 3.9.

By adjusting the normal force between the cones and sphere through varying the compression on springs denoted by **(6)**, the transmission torque limits can be set. As an example; if it is required to set the torque transmission limit to lower values, the normal force is reduced by releasing the compression on the spring, and as a result of this, when this limit is exceeded there will be slippage between the cones and the sphere. This property provides a protection against the excessive amount of torques to be applied to either the user or the actuator during operation. Therefore, the joint structure is inherently safe in the mechanical design sense.

If the system is arranged so that the spheres are aligned along the vertical axes, then the compression force (F_2) on the sphere below has to be higher than the compression force (F_1) on the sphere above in order to overcome the gravitational effects. As a result of this adjustment, normal forces between the cones and the spheres are set to be equal to each other, and the same type of transmission in two directions is made possible.

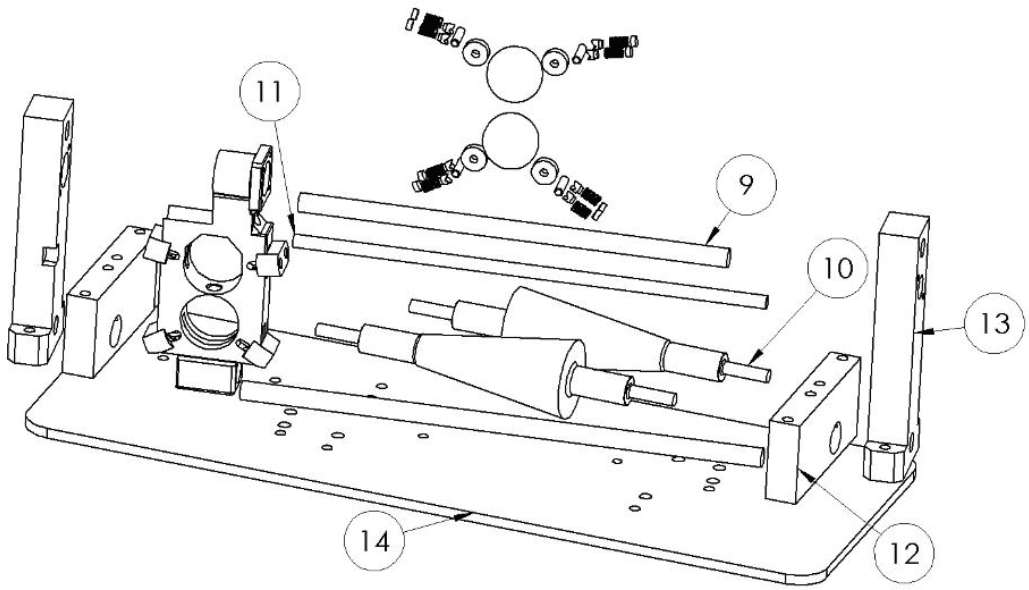

Figure 3.9. Exploded view of the whole assembly

The reason why bearings are used to transmit the compression force to the spheres is to minimize the friction in the linear guiding, which results in quicker response time for the variations in the transmission ratio.

3.2. Experimental Results

In order to validate working principle, proof of design experiment is conducted to observe if the same amount of torque can be transmitted in both clockwise (CW) and counter-clockwise (CCW) directions (Figure 3.10).

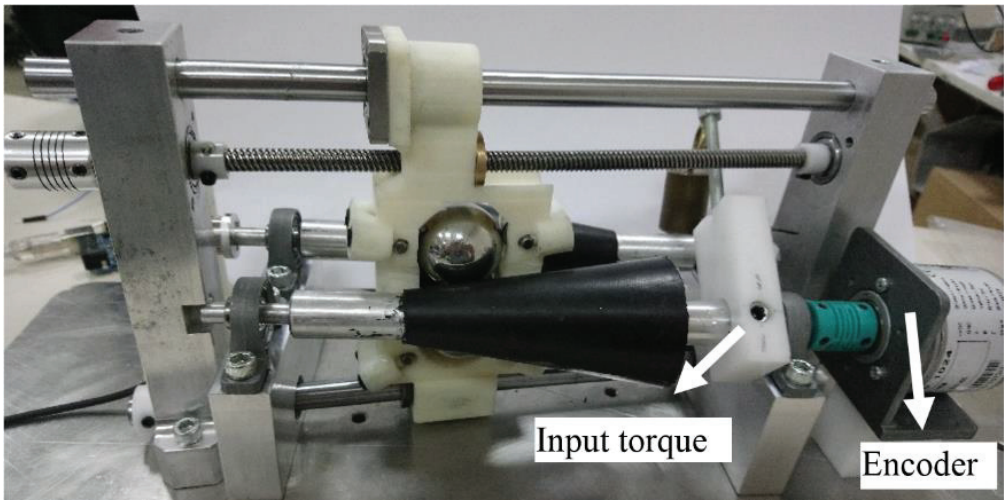

Figure 3.10. Experimental setup right side view

The experiment is carried out by determining 6 locations of the cone that corresponds to different test diameters. The location of the carriage is determined by measuring the distance from the wall (Figure 3.12). Afterwards, the selected locations' diameters are measured on the cones by the help of digital caliper (Mitutoyo). Input torque of 72 mN.m is applied by hanging a calibrated mass on the input cone from a measured moment arm length.

An encoder (Figure 3.10) with 0.3515° resolution is assembled on the input cone to observe if any slippage between the input cone and the sphere occurs. Output cone is coupled with a force/torque sensor (ATI, Nano17), which is presented in Figure 3.11, from which only the torque along the axis of rotation of the cone is measured. The output cone is mechanically fixed to the inertial frame in order to constrain its rotation.

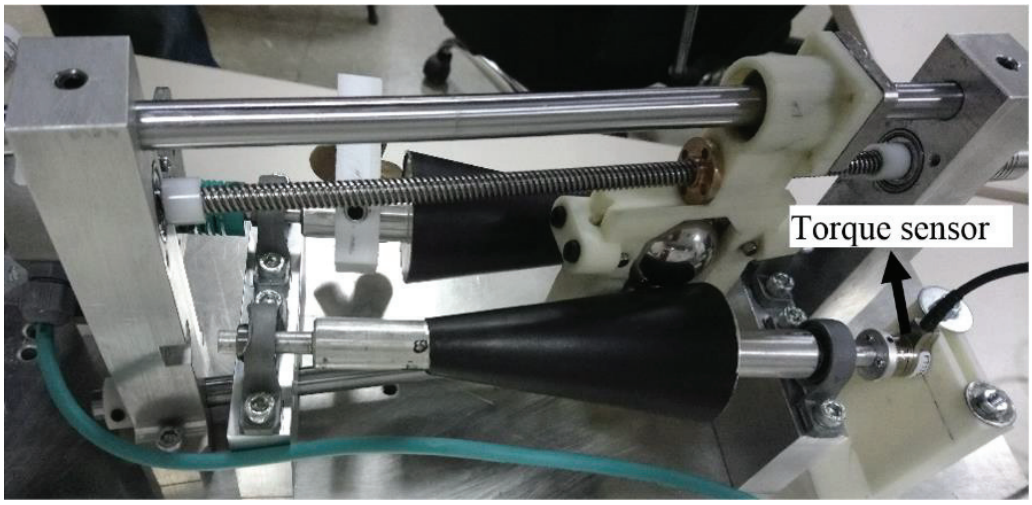

Figure 3.11. Experimental setup left side view

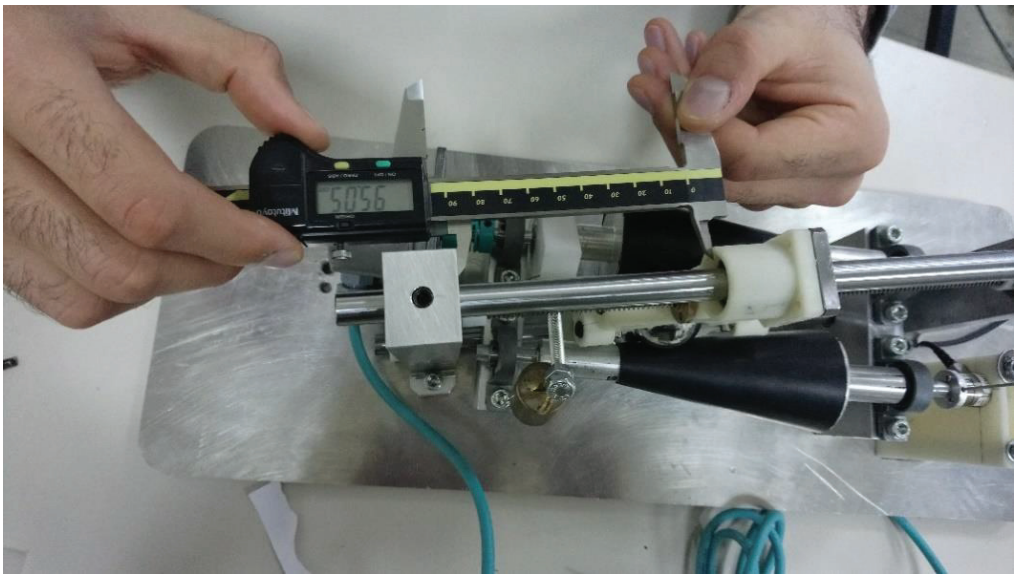

Figure 3.12. The determination of the position of the carriage from the base

In Table 3.1, the measured output torques for the same input torques in both CW and CCW directions are presented in each test point. According to these results, the torque transmission in both directions was accomplished.

Nevertheless, there are relatively small inconsistencies between the output torque measured in both directions at the same test point. Also, the inconsistency with respect to the direction of operation is not always in favor of one direction. For example, the CW output torque is higher than the CCW only in the 1st, 3rd, 4th and 6th test locations.

Table 3.1. Experimentally obtained output torque results

r_{out}/r_{in}	Input torque (mNm)	Direction	Output torque (mNm)
0.56	72	CW	33.39
		CCW	32.22
0.75	72	CW	40.17
		CCW	43.36
0.95	72	CW	52.52
		CCW	51.98
1.07	72	CW	66.57
		CCW	65.17
1.31	72	CW	68.21
		CCW	73.80
1.36	72	CW	85.66
		CCW	80.40

Therefore, it can be concluded that the inconsistency is not due to the concept that is tested here but due to the measurement inconsistencies and manufacturing errors. Especially, the manufacturing errors on the smoothness of the surfaces and the errors when placing the friction surfaces on the cones may have affected these results.

3.3. Conclusion

In this chapter, a new continuously variable transmission system to be used for human-robot interaction is introduced. The primary novelty of the design presented here is the modification of the transmission element from a wheel to two-spheres. The experimental results with the proof-of-concept prototype have showed that bidirectional torque transmission is possible with this design. Also, with this design, the user is able to alter the backdrivability level by ensuring the safe interaction which is demanded very vital criterion in the topic of robot-human interaction.

CHAPTER 4

KINEMATIC ANALYSIS OF THE CVT

In this chapter, the geometrical relations and the kinematic analysis of the new CVT design are studied. All calculations that are presented here are carried out by assuming all the components are perfectly rigid. In the first section, the position and orientation of the sphere with respect to the inertial frame (world frame) are computed by making use of five design parameters. The reason for this is to identify the limits of the CVT mathematically so that the optimum design methodology given in the next chapter can be acquired. To achieve this, the necessary rotations between the frames are defined, and the angles are computed with the help of plane geometry. In the next section, velocity level kinematics is investigated to prove the speed reduction achieved by using the cones. As a final step, numerical simulations with package programs are carried out to verify the calculations, and the reasons of errors are discussed. Calculations including velocity level kinematics and static force analysis are carried out based on the geometrical calculations given in the Section 4.1.

4.1. Geometrical Calculations of the CVT

In this section, the geometrical calculations of the CVT are carried out. The primary objective of this part is to compute the necessary positions and orientations of the bodies with the help of design parameters. To clarify, an arbitrary position of the sphere making contact with the cones is considered. Then, the required planes and the triangles are analyzed via the 3D drawing of the first prototype of the CVT. For each defined length or angle, the parametric formula is originated and controlled whether they are equal to the measured values from the 3D drawing.

Afterwards, these formulas are coded in Matlab environment, and the required orientations are calculated symbolically. Finally, the verification is achieved by comparing the calculated angles with the 3D drawing. The comparison is realized for five different positions. The results are presented at the end of this section.

In Figure 4.1, the isometric view of the drive is presented. There is a sphere located above the cones, and all the calculations are carried out by considering this structure. The other sphere, which is located below the cones, is not taken into account since investigating one sphere interaction is sufficient to understand how the system works.

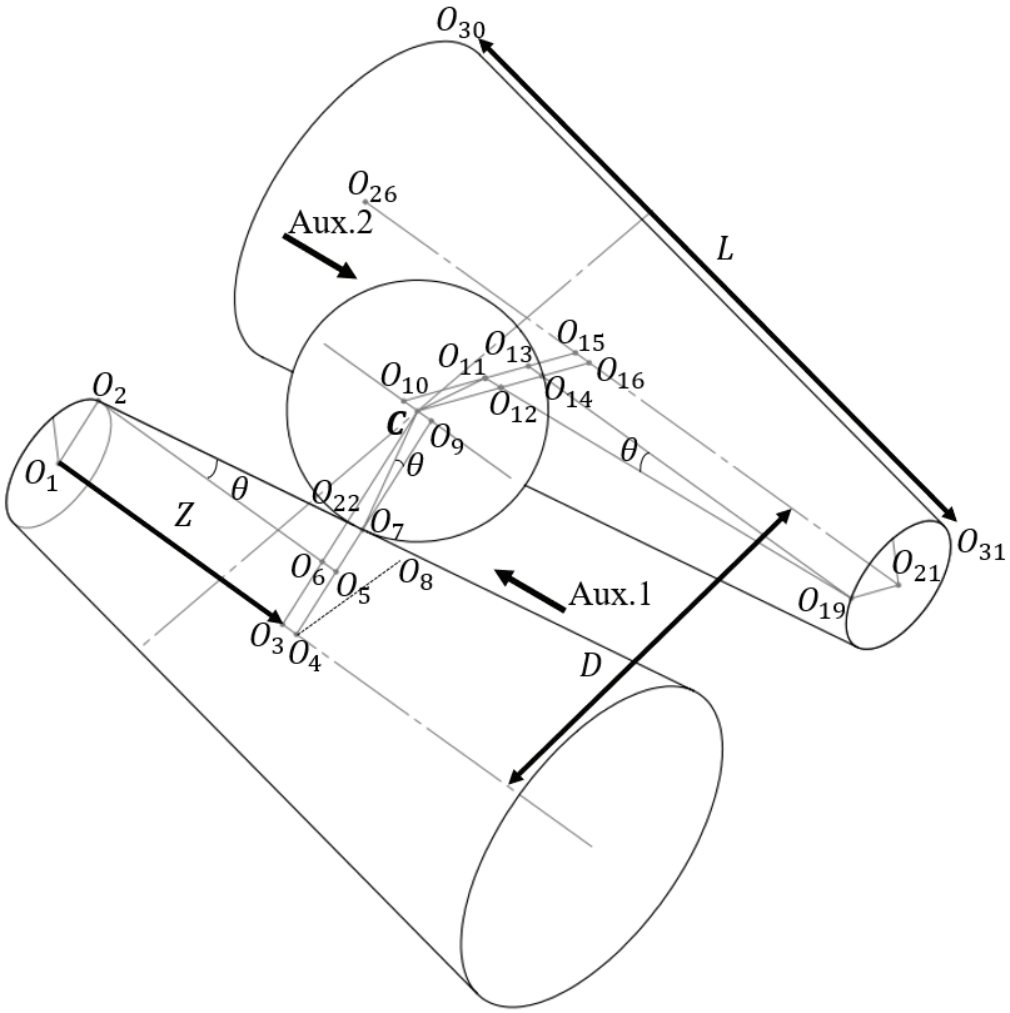

Figure 4.1. Isometric view of the drive

Additionally, since the two spheres are located along the same vertical axis, in other words, they always move symmetrically with respect to the $O_1O_3O_{16}O_{26}$ plane, it is sufficient to carry out the calculations with one of the spheres.

The properties of the lines are presented as follows:

$$\overrightarrow{O_1O_4} \parallel \overrightarrow{O_2O_5} \parallel \overrightarrow{O_{10}O_9} \parallel \overrightarrow{O_{13}O_{19}} \parallel \overrightarrow{O_{15}O_{21}} \tag{4.1}$$

$$\overrightarrow{O_{10}O_{15}} \parallel \overrightarrow{CO_{16}} \parallel \overrightarrow{CO_3} \parallel \overrightarrow{O_9O_4} \tag{4.2}$$

$$\overrightarrow{CO_7} \perp \overrightarrow{O_2O_7} \text{ and } \overrightarrow{CO_{11}} \perp \overrightarrow{O_{19}O_{11}} \tag{4.3}$$

The design parameters are *R, r_1, L, θ, D* where:

R ($\left|\overrightarrow{CO_7}\right|$): Radius of the sphere

r_1 ($\left|\overrightarrow{O_1O_2}\right|$): Minimum cone radius

L ($\left|\overrightarrow{O_{30}O_{31}}\right|$): The length of the side of the cone

θ: Cone angle

D: The distance between the cone's rotation axes

Z: The distance of the center of the sphere from the O_1

The necessary lengths are defined and calculated in between Equation 4.4 and 4.9.

$$\left|\overrightarrow{O_{22}O_7}\right| = \left|\overrightarrow{CO_{10}}\right| = \left|\overrightarrow{CO_9}\right| = \left|\overrightarrow{O_6O_5}\right| = \left|\overrightarrow{O_{11}O_{12}}\right| = \left|\overrightarrow{O_{13}O_{14}}\right| = \left|\overrightarrow{O_{15}O_{16}}\right| = R\sin\theta \tag{4.4}$$

$$\left|\overrightarrow{O_1O_3}\right| = \left|\overrightarrow{O_2O_6}\right| = \left|\overrightarrow{O_{26}O_{16}}\right| = Z \tag{4.5}$$

$$\left|\overrightarrow{O_{26}O_{21}}\right| = L\cos\theta \tag{4.6}$$

$$\left|\overrightarrow{O_{16}O_{21}}\right| = L\cos\theta - Z \tag{4.7}$$

$$\left|\overrightarrow{O_2O_5}\right| = \left|\overrightarrow{O_2O_6}\right| + \left|\overrightarrow{O_6O_5}\right| = Z + R\sin\theta \tag{4.8}$$

$$\left|\overrightarrow{O_{19}O_{13}}\right| = \left|\overrightarrow{O_{21}O_{15}}\right| = \left|\overrightarrow{O_{16}O_{21}}\right| + \left|\overrightarrow{O_{16}O_{15}}\right| = L\cos\theta - Z + R\sin\theta \tag{4.9}$$

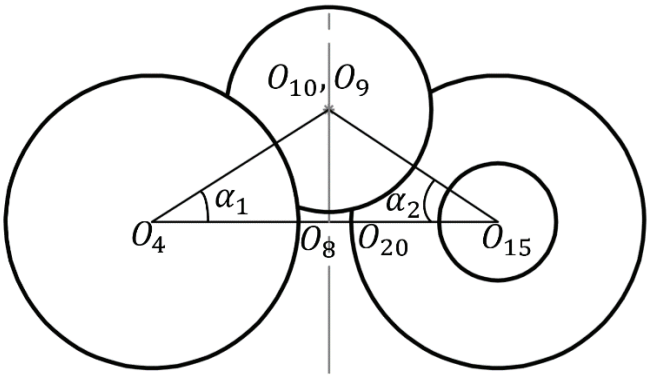

Figure 4.2. Front view of the drive

Based on the Figure 4.2, the triangles presented in Figure 4.3 are formed. In Figure 4.3, O_{20} is illustrated. This point can also be seen clearly in Figure 4.2. Since $\left|\overrightarrow{O_2O_5}\right|$ and $\left|\overrightarrow{O_{19}O_{13}}\right|$ are known, y_1 and y_2 are calculated in Equation 4.10 and 4.11.

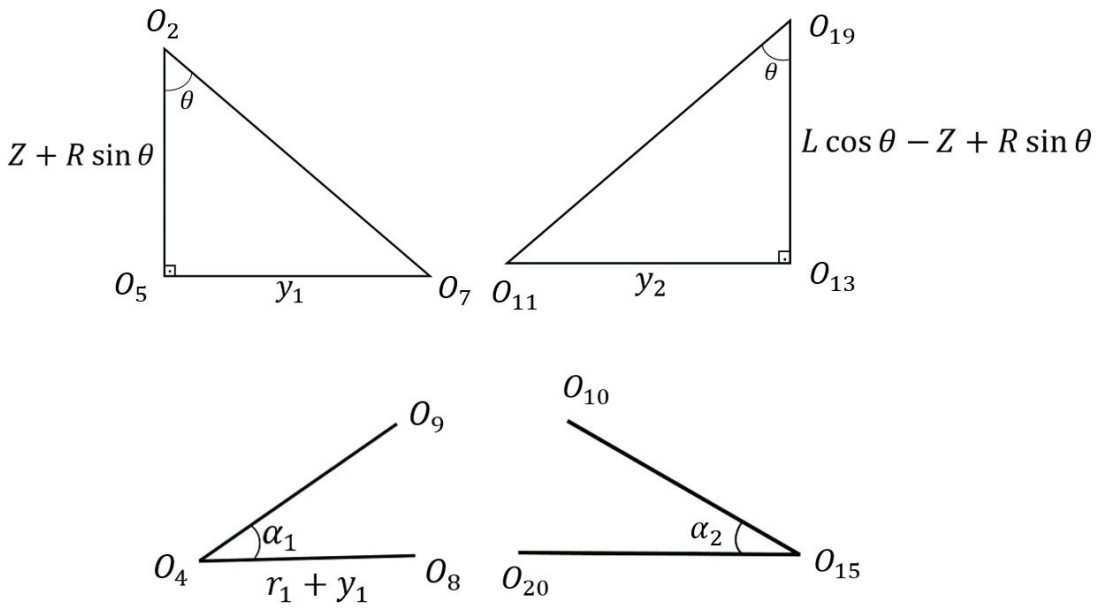

Figure 4.3. 1st group of triangles illustration

$$y_1 = \tan\theta\,(Z + R\sin\theta) \tag{4.10}$$

$$y_2 = \tan\theta\,(L\cos\theta - Z + R\sin\theta) \tag{4.11}$$

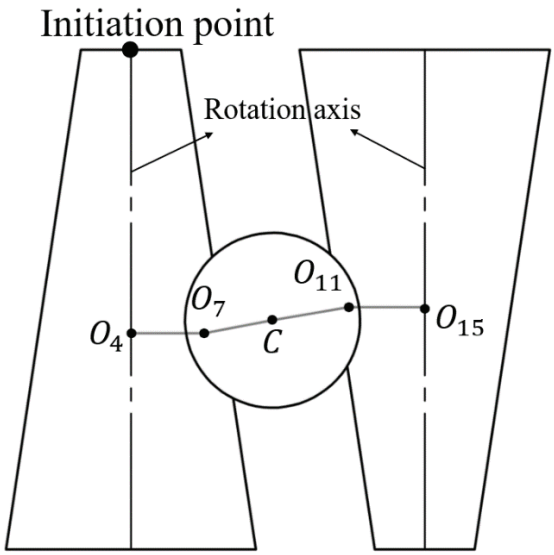

Figure 4.4. Top view of the drive

In Figure 4.4, O_7 and O_{11} are contact points of the sphere. It can be clearly observed that these points are not along the same horizontal axis. Hence, effective rotation

radii do not have the same distance from the initiation point for any position of the sphere. These radii (r_2 and r_3) are calculated from the Equation 4.12 and 4.13 by drawing a line which is perpendicular to the rotation axis of the cones. In fact, r_2 is not the smallest cone radius. However, it is the effective radius.

Considering Figure 4.3, since $O_9O_4O_8$ and $O_{10}O_{15}O_{20}$ define a half triangle, the intersection of them, which is presented in Figure 4.5, denotes a complete triangle. Thus, r_L and r_R are computed from Equation 4.14 and 4.15

$$r_2 = \left|\overrightarrow{O_4O_7}\right| = y_1 + r_1 \tag{4.12}$$

$$r_3 = \left|\overrightarrow{O_{11}O_{15}}\right| = y_2 + r_1 \tag{4.13}$$

$$r_L = \left|\overrightarrow{O_9O_4}\right| = r_1 + y_1 + R\cos\theta \tag{4.14}$$

$$r_R = \left|\overrightarrow{O_{10}O_{15}}\right| = r_1 + y_2 + R\cos\theta \tag{4.15}$$

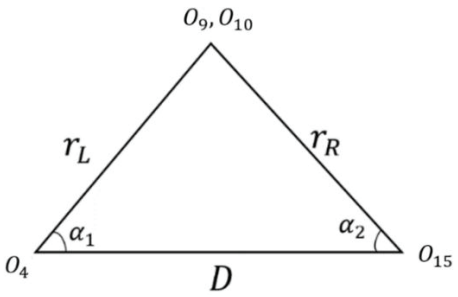

Figure 4.5. The illustration of $O_9O_4O_{15}$ triangle

Cosine theorem is implemented in Equation 4.16 and 4.17 to compute the α_1 and α_2.

$$\cos\alpha_1 = (r_L^2 + D^2 - r_R^2)/(2r_LD) \tag{4.16}$$

$$\cos\alpha_2 = (r_R^2 + D^2 - r_L^2)/(2r_RD) \tag{4.17}$$

Now, the coordinates of the center of the sphere can be written with respect to O_1:

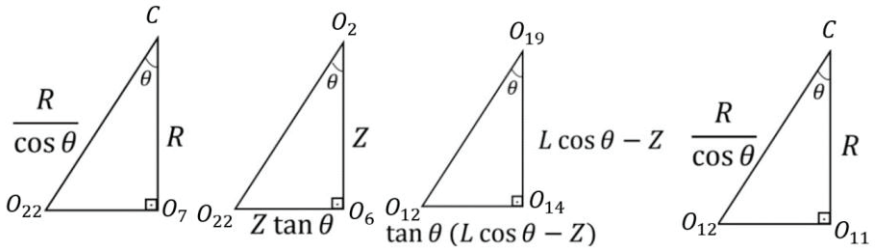

Figure 4.6. 2nd group of triangles

Since $|\overrightarrow{CO_7}|$, $|\overrightarrow{O_2O_6}|$, $|\overrightarrow{O_{19}O_{14}}|$ and $|\overrightarrow{CO_{11}}|$ are known, $|\overrightarrow{CO_{22}}|$, $|\overrightarrow{O_{22}O_6}|$, $|\overrightarrow{O_{12}O_{14}}|$ and $|\overrightarrow{CO_{12}}|$ are found from trigonometric relations indicated in Figure 4.6. Also, by using these triangle equalities, the following distances (Equation 4.18 and 4.19) are obtained from Figure 4.7:

$$r_{CL} = |\overrightarrow{CO_3}| = r_1 + Z\tan\theta + (R/\cos\theta) \tag{4.18}$$

$$r_{CR} = |\overrightarrow{CO_{16}}| = r_1 + \tan\theta(L\cos\theta - Z) + (R/\cos\theta) \tag{4.19}$$

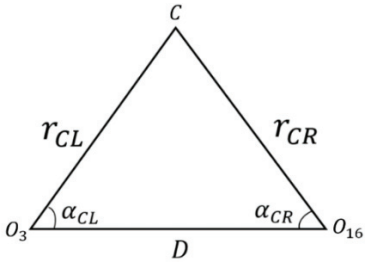

Figure 4.7. The illustration of the center of the sphere by the help of a triangle

Using cosine theorem, α_{CL} and α_{CR} are computed (Equation 4.20 and 4.21). Hence:

$$\cos\alpha_{CL} = (r_{CL}^2 + D^2 - r_{CR}^2)/(2r_{CL}D) \tag{4.20}$$

$$\cos\alpha_{CR} = (r_{CR}^2 + D^2 - r_{CL}^2)/(2r_{CR}D) \tag{4.21}$$

Obviously $\alpha_1 = \alpha_{CL}$ and $\alpha_2 = \alpha_{CR}$.

The position vector of the center of the sphere, $\vec{P}_C$, with respect to 0th frame (Figure 4.8) is written in Equation 4.22.

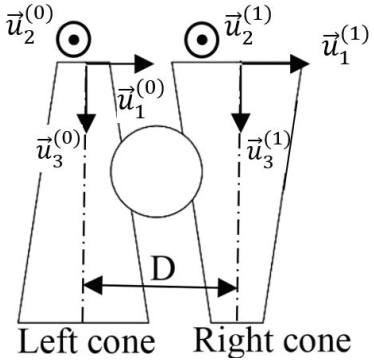

Figure 4.8. The illustration of the 0th and 1st frame

$$\vec{P}_C = \overrightarrow{O_1C} = (r_{CL}\cos\alpha_{CL})\vec{u}_1^{(0)} + (r_{CL}\sin\alpha_{CL})\,\vec{u}_2^{(0)} + Z\vec{u}_3^{(0)} \tag{4.22}$$

In Figure 4.9, 4.10 and 4.11, the translation of the center of the sphere as it is moved from one end of the drive to the other end with respect to $\vec{u}_2^{(0)} - \vec{u}_3^{(0)}$ plane, $\vec{u}_1^{(0)} - \vec{u}_3^{(0)}$ plane, and in 3D are illustrated, respectively. Indeed, all three graphs are drawn by making use of Equation 4.22.

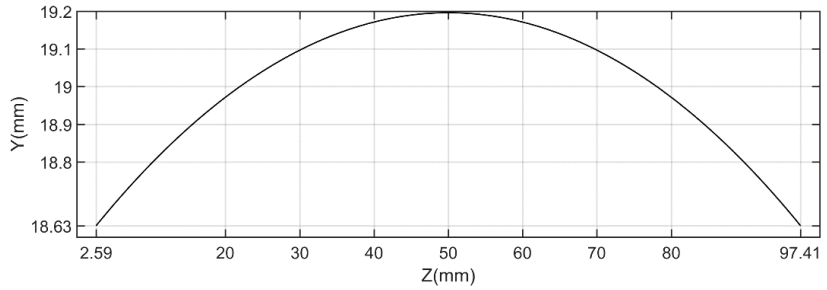

Figure 4.9. The position variation of the center of the sphere in $\vec{u}_2^{(0)} - \vec{u}_3^{(0)}$ plane

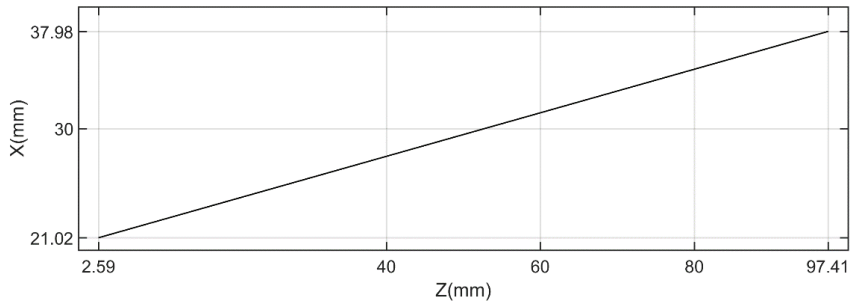

Figure 4.10. The position variation of the center of the sphere in $\vec{u}_1^{(0)} - \vec{u}_3^{(0)}$ plane

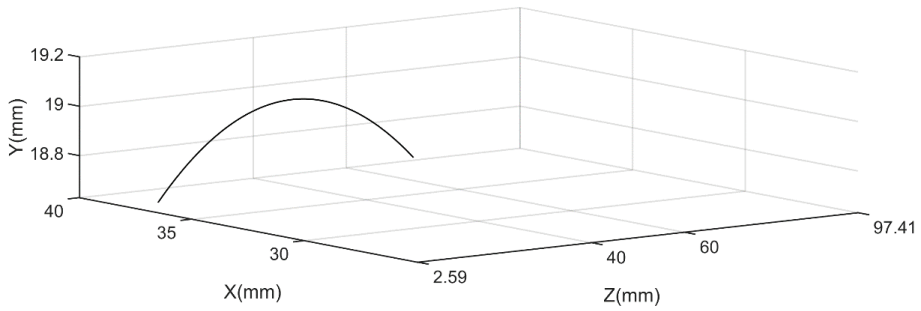

Figure 4.11. The position variation of the center of the sphere in 0th frame

The position vector of the left cone contact point with respect to 0th frame can be considered now. The left cone contact point is O_7 . Therefore, $\vec{P}_L$ defines the $\overrightarrow{O_1O_7}$ distance (Equation 4.23).

$$\vec{P}_L = ((r_1 + y_1)\cos\alpha_1)\vec{u}_1^{(0)} + ((r_1 + y_1)\sin\alpha_1)\vec{u}_2^{(0)} + (Z + R\sin\theta)\vec{u}_3^{(0)} \quad (4.23)$$

The position vector of the right cone contact point with respect to 1st frame is written by the help of $\overrightarrow{O_{26}O_{11}}$ since the right cone contact point is O_{11}. Therefore, the $\vec{P}_R$ (Equation 4.24) defines the $\overrightarrow{O_{26}O_{11}}$ distance:

$$\vec{P}_R = (-(r_1 + y_2)\cos\alpha_2)\vec{u}_1^{(1)} + ((r_1 + y_2)\sin\alpha_2)\vec{u}_2^{(1)} + (Z - R\sin\theta)\vec{u}_3^{(1)} \quad (4.24)$$

In order to represent $\vec{P}_R$ in 0th frame, the transformation matrix $\widehat{H}^{(0,1)}$ is defined in Equation 4.25, and the necessary rotations are performed in Equation 4.26 and 4.27.

$$\widehat{H}^{(0,1)} = \begin{bmatrix} 1 & 0 & 0 & D \\ 0 & 1 & 0 & 0 \\ 0 & 0 & 1 & 0 \\ 0 & 0 & 0 & 1 \end{bmatrix} \quad (4.25)$$

$$\bar{P}_R^{*(0)} = \widehat{H}^{(0,1)}\bar{P}_R^{*(1)}, \text{ where } \bar{P}_R^{*(i)} = \begin{bmatrix} \bar{P}_R^{(i)} \\ 1 \end{bmatrix} \quad (4.26)$$

$$\vec{P}_R = (-(y_2 + r_1)\cos\alpha_2 + D)\vec{u}_1^{(0)} + ((y_2 + r_1)\sin\alpha_2)\vec{u}_2^{(0)} + (Z - R\sin\theta)\vec{u}_3^{(0)} \quad (4.27)$$

After determining the position vector of the contact points with respect to the inertial frame, the boundary conditions of the contact points in terms of the Z parameter is indicated. Considering Figures 4.1 and 4.4, it is clear that the minimum Z value from the inertial frame of reference (0th frame) is equal to $\vec{u}_3^{(0)}$ element of the $\vec{P}_R$ (Equation 4.28). In other words, if taking this component to be zero (Equation 4.29), the minimum Z value can be computed (Equation 4.30). The reason for this is that the position of the right cone contact point is always closer to the inertial frame than the left cone contact point.

$$\vec{P}_R = (-(r_1 + y_2)\cos\alpha_2)\vec{u}_1^{(1)} + ((r_1 + y_2)\sin\alpha_2)\vec{u}_2^{(1)} + (Z - R\sin\theta)\vec{u}_3^{(1)} \quad (4.28)$$

$$0 = Z_{min} - R\sin\theta \quad (4.29)$$

$$Z_{min} = R\sin\theta \quad (4.30)$$

On the other hand, the maximum Z value is obtained from $\vec{u}_3^{(0)}$ element of $\vec{P}_L$. In this case, this element is made equal to $L\cos\theta$ as the maximum distance from the inertial frame is stated with this term.

The maximum Z value is obtained from Equation 4.6. $\vec{u}_3^{(0)}$ element of the $\vec{P}_L$ is equated to the maximum distance ($L\cos\theta$) from the inertial frame of reference in Equation 4.31 and 4.32.

$$Z_{max} + R\sin\theta = L\cos\theta \tag{4.31}$$

$$Z_{max} = L\cos\theta - R\sin\theta \tag{4.32}$$

In this way, the boundary conditions of the Z values are computed. These boundaries help us to determine the maximum, and the minimum transmission ratio of the drive as this ratio is regulated through the location of the contact points with respect to the inertial frame. The details of this study are discussed in Chapter 5.

Until now, the position of the sphere is calculated with respect to the inertial frame. However, the orientation of this element is not examined. At this point, the investigation of this issue is addressed.

In Figure 4.12, side view of the CVT is presented. A plane is defined by making use of C, O_7 and O_{11} points (Figure 4.1).

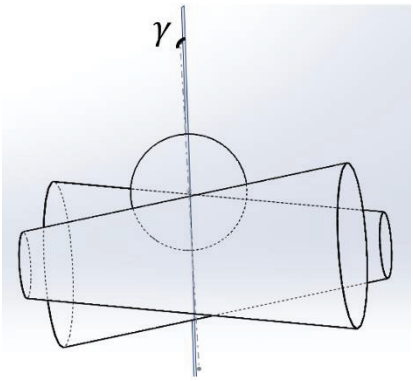

Figure 4.12. The illustration of the γ angle

It is observed in Figure 4.12 that there is an angle defined with γ between the vertical axis of the sphere and the aforementioned plane. This means that if the input cone is rotated around $\vec{u}_3^{(0)}$ axis, the effect of this rotation on the sphere will not be only around the one axis due to γ angle. There are two components. Therefore, the new frame is attached to the center of the sphere so that the rotation with respect to the 0^{th} frame is calculated.

In Figure 4.13 (the detailed view of Figure 4.1), there are three frames identified with numbers 2, 3 and 4. The second frame has the same orientation with respect to the inertial frame and the first frame that is stated in Figure 4.8. Therefore, rotations with respect to the second frame can be considered as the rotations with respect to the inertial frame. In the third frame, it is aimed to determine the axis which is tangent to the left cone contact point along the longitudinal direction. Thus, the rotation (θ_{11}) is performed around $\vec{u}_2^{(2)}$ axis as it can be seen in Figure 4.13 and 4.17. Afterwards, the axes that are aligned with the left cone contact point are specified by rotating the third frame around $\vec{u}_3^{(3)}$ due to the fact that $\vec{u}_3^{(3)}$ is tangent to the sphere and the left cone contact point. Thus, the required axes, which describes the surface normal of the left cone contact point, is assigned as $\vec{u}_1^{(4)}$ that is aligned with $\overrightarrow{O_{23}C}$. Further, $\vec{u}_2^{(4)}$ defines the direction of the tangential velocity and the forces acting between the cones and the sphere. This issue is analyzed in Section 4.2.

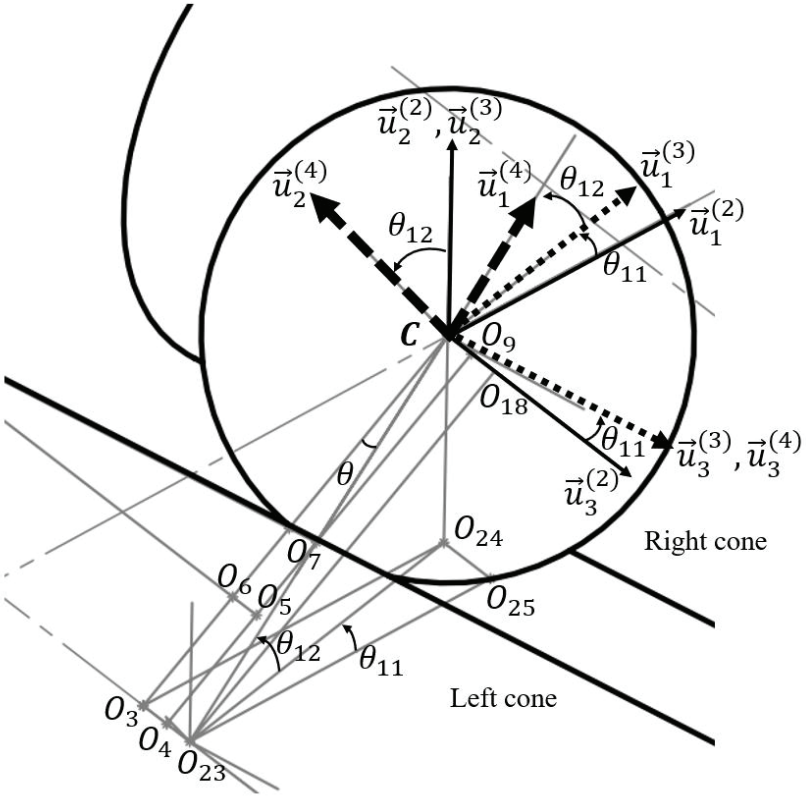

Figure 4.13. Detailed view of the left cone contact point

After identifying the required angles, the parametric equalities of these angles are investigated by the help of the 3D drawing. First, the CO_3O_{23} triangle is evaluated (Figure

4.14). In this case, $\overrightarrow{CO_3}$ is perpendicular to $\vec{u}_2^{(0)}(\vec{u}_2^{(2)})$ which is the rotation axis of the input cone. Since $\left|\overrightarrow{CO_3}\right|$ is already known as r_{CL} and the angle between the $\left|\overrightarrow{O_3\vec{C}}\right|$ and $\left|\overrightarrow{O_{23}\vec{C}}\right|$ is θ, $\left|\overrightarrow{O_3O_{23}}\right|$ can be calculated. Afterwards, $\left|\overrightarrow{O_3O_{24}}\right|$ and $\left|\overrightarrow{CO_{24}}\right|$ are found from the CO_3O_{24} triangle as stated in detail in Figure 4.14.

To determine the θ_{11}, $O_{23}O_3O_{24}$ is worked out. In this case, it is clear that $\left|\overrightarrow{O_3O_{24}}\right|$ is parallel to $\left|\overrightarrow{O_{23}O_{25}}\right|$ and $\left|\overrightarrow{O_3O_{23}}\right|$ is parallel to $\left|\overrightarrow{O_{24}O_{25}}\right|$. Further, since these terms are computed already, θ_{11} is obtained as illustrated in Figure 4.15. The calcualtions for θ_{11} are presented in between Equation 4.33 and 4.35.

Finally, θ_{12} is calculated from the $O_{24}O_{23}C$ triangle as presented in Figure 4.16. The necesssary mathemetical operations are performed in Equation 4.36 and 4.37.

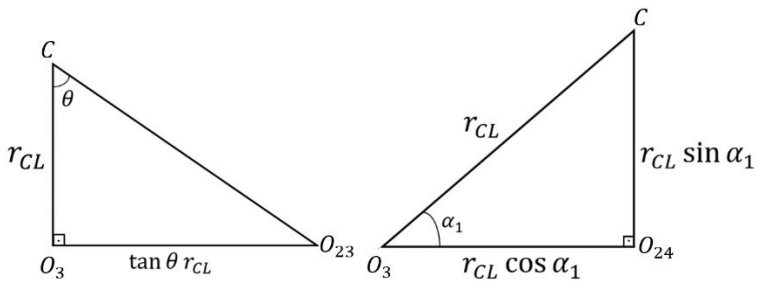

Figure 4.14. 3rd group of the triangles

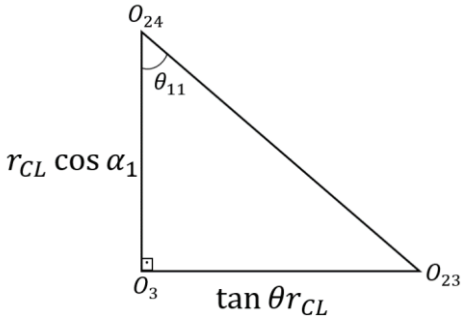

Figure 4.15. The illustration of the $O_{24}O_3O_{23}$ triangle

$$\left|\overrightarrow{O_{23}O_{24}}\right| = \sqrt{(r_{CL}\cos\alpha_1)^2 + (\tan\theta r_{CL})^2} \quad (4.33)$$

$$\tan\theta_{11} = (\tan\theta r_{CL})/(r_{CL}\cos\alpha_1) \quad (4.34)$$

$$\theta_{11} = \tan^{-1}((\tan\theta r_{CL})/(r_{CL}\cos\alpha_1)) \quad (4.35)$$

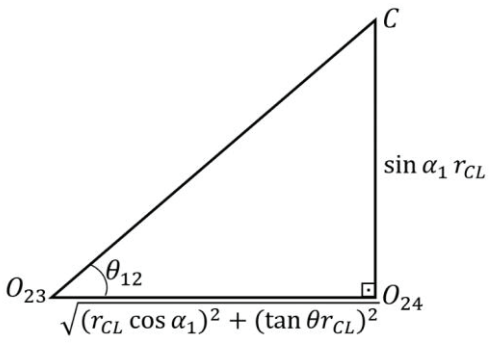

Figure 4.16. The illustration of the $CO_{24}O_{23}$ triangle

$$\tan\theta_{12} = (\sin\alpha_1 r_{CL})/(\sqrt{(r_{CL}\cos\alpha_1)^2 + (\tan\theta r_{CL})^2}) \quad (4.36)$$

$$\theta_{12} = \tan^{-1}((\sin\alpha_1 r_{CL})/(\sqrt{(r_{CL}\cos\alpha_1)^2 + (\tan\theta r_{CL})^2})) \quad (4.37)$$

The rotations in between frames are illustrated in Figure 4.17.

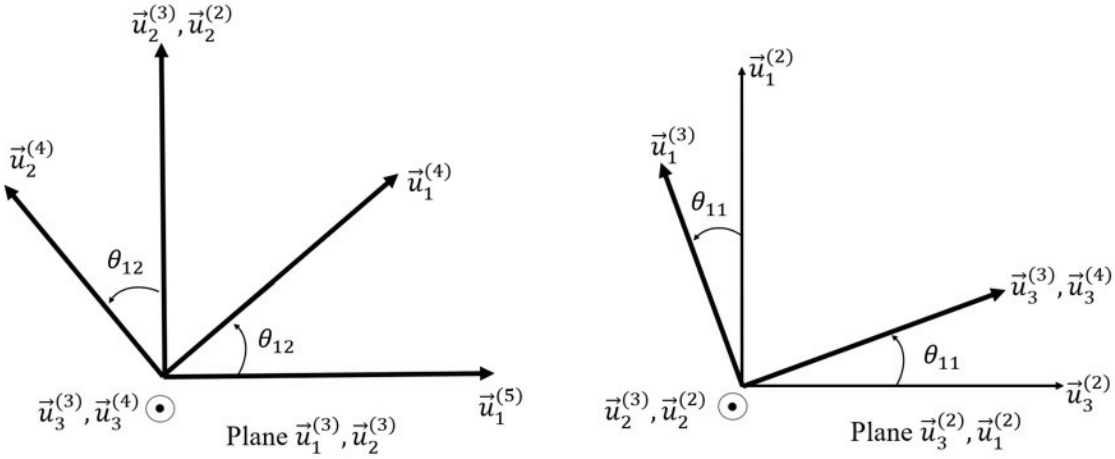

Figure 4.17. Rotations taking place on the sphere for left contact point

Since the orientation of the 0th and 2nd frame is the same, the rotation matrix are written between the 2nd and the 4th frame is in Equation 4.38, 4.39 and 4.40.

$$\hat{C}^{(2,4)} = \hat{C}^{(2,3)}\hat{C}^{(3,4)} = e^{\tilde{u}_2^{(3)}\theta_{11}} e^{\tilde{u}_3^{(3)}\theta_{12}} \quad (4.38)$$

$$\hat{C}^{(2,3)} = \begin{bmatrix} \cos\theta_{11} & 0 & \sin\theta_{11} \\ 0 & 1 & 0 \\ -\sin\theta_{11} & 0 & \cos\theta_{11} \end{bmatrix} \quad (4.39)$$

$$\hat{C}^{(3,4)} = \begin{bmatrix} \cos\theta_{12} & -\sin\theta_{12} & 0 \\ \sin\theta_{12} & \cos\theta_{12} & 0 \\ 0 & 0 & 1 \end{bmatrix} \quad (4.40)$$

$$\hat{C}^{(2,4)} = \begin{bmatrix} \cos\theta_{11}\cos\theta_{12} & -\cos\theta_{11}\sin\theta_{12} & \sin\theta_{11} \\ \sin\theta_{12} & \cos\theta_{12} & 0 \\ -\cos\theta_{12}\sin\theta_{11} & \sin\theta_{11}\sin\theta_{12} & \cos\theta_{11} \end{bmatrix} \tag{4.41}$$

where, $\hat{C}^{(0,i)}$ is the transformation matrix between the inertial frame and the ith frame. The complete version of the rotation matrix (Equation 4.41) which has a relation with design parameters (R, r_1, L, D, θ), is not written here as it has higher number of terms to be presented.

As a next step, the rotations taking place between the sphere and the right cone contact point are analyzed. Since the surface normal for the right contact point ($\overrightarrow{CO_{11}}$) and the left contact point ($\overrightarrow{CO_7}$) do not make the same orientation with respect to the 0th frame, each of them is considered separately. The orientation of the surface normal for the right contact point with respect to the 0th frame is indicated in Figure 4.18.

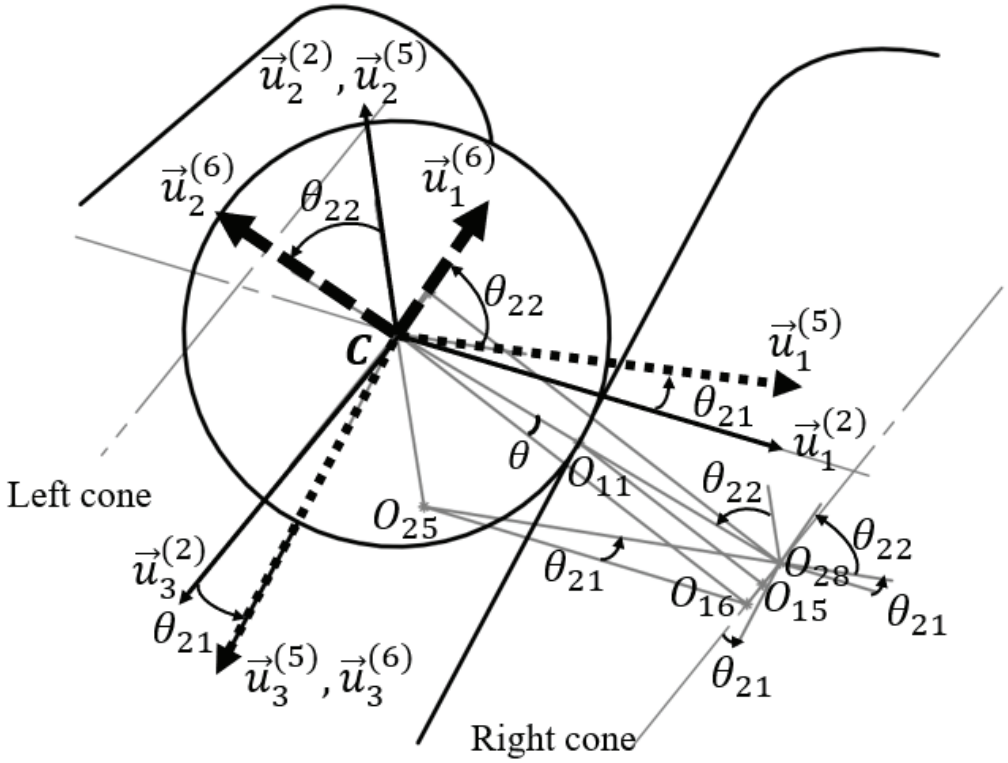

Figure 4.18. Detailed view of the right cone contact point

In Figure 4.18, the second frame is the mutual frame for the two contact points as it can be seen in Figure 4.13. Hence, the connection between them is achieved with the help of this frame. Same as the previous contact point rotations, there are three frames illustrated with the number 2, 5 and 6. Thus, in the 5th frame, the axes that are tangent to

the sphere along the longitudinal direction is obtained. Finally, in the 6th frame, the axis ($\overrightarrow{O_{28}C}$) that is aligned with the contact point of the right cone and the sphere is acquired and defined as $\vec{u}_2^{(6)}$.

Afterwards, the parametric calculations are performed with the help of triangles. First, $CO_{16}O_{28}$ triangle is evaluated and $\left|\overrightarrow{O_{16}O_{28}}\right|$ is found from the trigonometry. Then, $\left|\overrightarrow{CO_{25}}\right|$ and $\left|\overrightarrow{O_{25}O_{16}}\right|$ are obtained as it can be seen in Figure 4.19. Now, θ_{21} can be calculated from the $O_{25}O_{16}O_{28}$ triangle (Figure 4.20). To do this, first $\left|\overrightarrow{O_{25}O_{28}}\right|$ is calculated (Equation 4.42), and then θ_{21} is acquired from the trigonometric relations in Equation 4.43 and 4.44. To obtain the θ_{22}, θ_{23} is computed (Equation 4.45 and 4.46) from the $CO_{25}O_{28}$ triangle (Figure 4.21). Finally, θ_{22} is calculated in Equation 4.47.

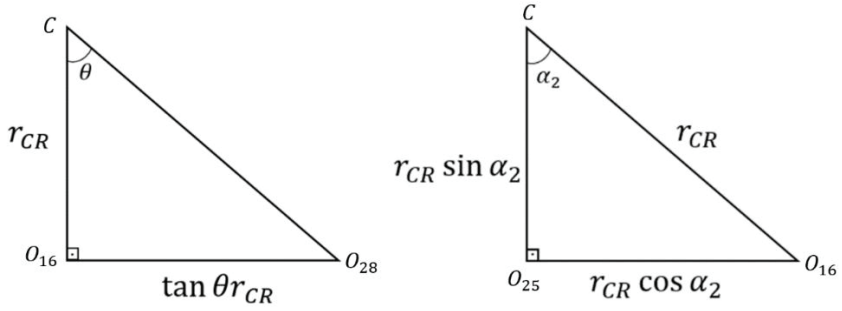

Figure 4.19. 4th group of triangles

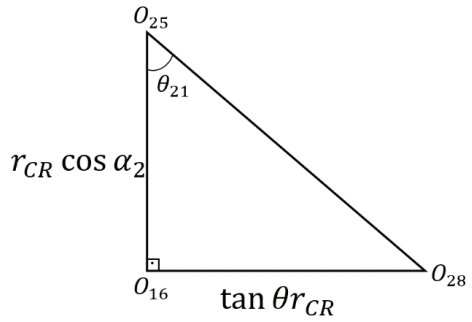

Figure 4.20. The illustration of the $O_{25}O_{16}O_{28}$ triangle

$$\left|\overrightarrow{O_{25}O_{28}}\right| = \sqrt{(r_{CR}\cos\alpha_2)^2 + (\tan\theta r_{CR})^2} \tag{4.42}$$

$$\tan\theta_{21} = (\tan\theta r_{CR})/(\sqrt{(r_{CR}\cos\alpha_2)^2 + (\tan\theta r_{CR})^2}) \tag{4.43}$$

$$\theta_{21} = \tan^{-1}((\tan\theta r_{CR})/(\sqrt{(r_{CR}\cos\alpha_2)^2 + (\tan\theta r_{CR})^2})) \tag{4.44}$$

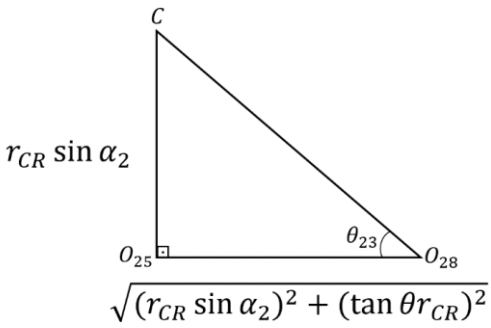

Figure 4.21. The illustration of the $CO_{25}O_{28}$ triangle

$$\tan\theta_{22} = (r_{CR}\sin\alpha_2)/(\sqrt{(r_{CR}\sin\alpha_2)^2+(\tan\theta r_{CR})^2}) \quad (4.45)$$

$$\theta_{23} = \tan^{-1}((r_{CR}\sin\alpha_2)/(\sqrt{(r_{CR}\sin\alpha_2)^2+(\tan\theta r_{CR})^2})) \quad (4.46)$$

$$\theta_{22} = 90 - \theta_{23} \quad (4.47)$$

The rotations in between the frames are illustrated in Figure 4.22.

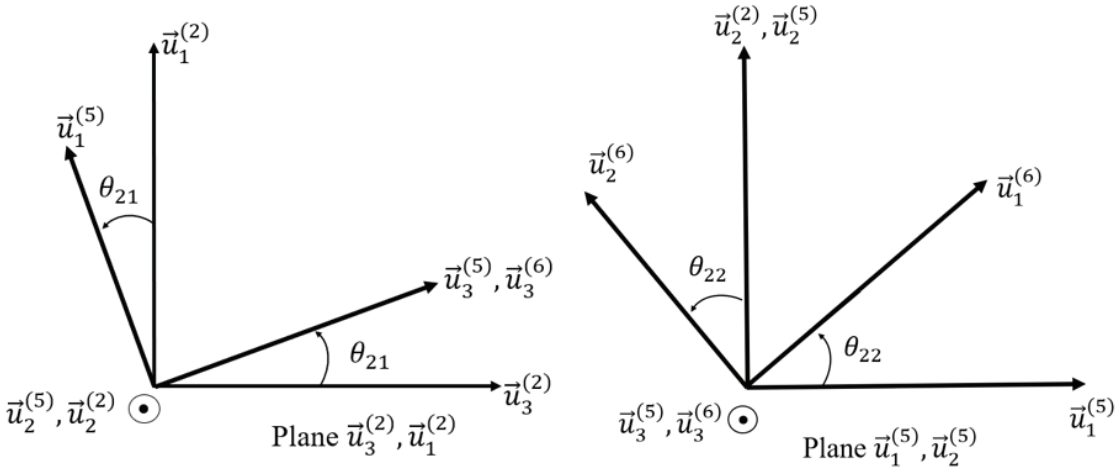

Figure 4.22. Rotations taking place on the sphere for left contact point

Since the orientation of the 0th and 2nd frame is the same, the rotation matrix are written between the 2nd and 6th frame is in between Equation 4.48 and 4.51:

$$\hat{C}^{(2,6)} = \hat{C}^{(2,5)}\hat{C}^{(5,6)} = e^{\tilde{u}_2^{(5)}\theta_{11}}e^{\tilde{u}_3^{(5)}\theta_{12}} \quad (4.48)$$

$$\hat{C}^{(2,5)} = \begin{bmatrix} \cos\theta_{21} & 0 & \sin\theta_{21} \\ 0 & 1 & 0 \\ -\sin\theta_{21} & 0 & \cos\theta_{21} \end{bmatrix} \quad (4.49)$$

$$\hat{C}^{(5,6)} = \begin{bmatrix} \cos\theta_{22} & -\sin\theta_{22} & 0 \\ \sin\theta_{22} & \cos\theta_{22} & 0 \\ 0 & 0 & 1 \end{bmatrix} \quad (4.50)$$

$$\hat{C}^{(2,6)} = \begin{bmatrix} \cos\theta_{21}\cos\theta_{22} & -\cos\theta_{21}\sin\theta_{22} & \sin\theta_{21} \\ \sin\theta_{22} & \cos\theta_{22} & 0 \\ -\cos\theta_{22}\sin\theta_{21} & \sin\theta_{21}\sin\theta_{22} & \cos\theta_{21} \end{bmatrix} \quad (4.51)$$

Same as before, the complete version of rotation matrix (Equation 4.51) which has a relation with design parameters, (R, r_1, L, D, θ) is not written here as it has high number of terms.

Finally, another cone radius is calculated in Equation 4.52.

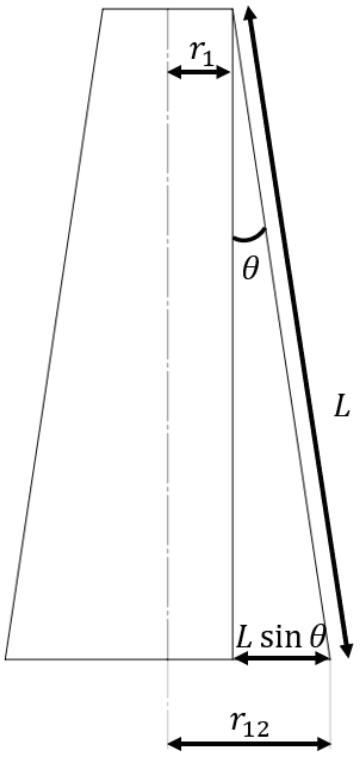

Figure 4.23. The geometric illustration of another cone radius

$$r_{12} = r_1 + l\sin\theta \quad (4.52)$$

In Equation 4.52, r_{12} is stated as the largest cone radius (Figure 4.23). This term also can be considered as r_3 (Equation 4.13) if the sphere is at the maximum Z distance since r_3 is a variable and changes according to the Z parameter.

As a final step, the angles that are calculated in this section are obtained for different Z values from Solidworks. After that, the theoretical calculations are carried out with the help of Matlab and errors are computed with respect to measured values and presented in Table 4.1.

Table 4.1. The comparison between the measured and calculated angles

$Z\ (\theta_{11})$	Measured (θ_{11})	Calculated (θ_{11})	Error% (θ_{11})
3	11.31946°	11.31969°	0.002
12	11.02832°	11.02835°	0.0002
21	10.77512°	10.77515°	0.0002
62	9.94483°	9.94487°	0.0003
70	9.82542°	9.82545°	0.0003
97	9.48851°	9.48855°	0.0003
$Z\ (\theta_{12})$	Measured (θ_{12})	Calculated (θ_{12})	Error% (θ_{12})
3	40.91493°	40.91500°	0.0001
12	39.15973°	39.15980°	0.0001
21	37.49693°	37.49690°	0.00007
62	30.80983°	30.80987°	0.0001
70	29.63348°	29.63352°	0.0001
97	25.87205°	25.87207°	0.00008
$Z\ (\theta_{21})$	Measured (θ_{21})	Calculated (θ_{21})	Error% (θ_{21})
3	9.48842°	9.48845°	0.0003
12	9.59081°	9.59085°	0.0003
21	9.70265°	9.70269°	0.0003
62	10.37715°	10.37720°	0.0004
70	10.55281°	10.55286°	0.0004
97	11.31933°	11.31938°	0.0004
$Z\ (\theta_{22})$	Measured (θ_{22})	Calculated (θ_{22})	Error% (θ_{22})
3	64.12918°	64.12915°	0.00003
12	62.90617°	62.90614°	0.00004
21	61.65407°	61.65404°	0.00005
62	55.43255°	55.43249°	0.0001
70	54.08648°	54.08641°	0.0001
97	49.08691°	49.08682°	0.0001

According to the Table 4.1, overall average error is calculated 0.0009% which concludes that the errors are in in the level of numerical error ranges.

4.2. Velocity Level Kinematics

In this section kinematic analysis of the CVT in velocity level is studied. Each element affecting the rotation is considered separately and presented step by step. Moreover, after presenting the parametric calculations, the numerical calculations are investigated so that the relation between the physical meaning and the mathematical meaning can be comprehended. The values used in numerical calculations are assigned with respect to the first prototype dimensions presented in Table 4.2.

Table 4.2. The dimensions of the first prototype

$R\,(\lvert\overrightarrow{CO_7}\rvert)$:	17.5 mm
$r_1\,(\lvert\overrightarrow{O_1O_2}\rvert)$:	10 mm
$L\,(\lvert\overrightarrow{O_{30}O_{31}}\rvert)$:	101.12 mm
θ:	0.14 rad
D:	59 mm
ω_{in}:	1.04 rad/sec (10 rpm)
Z:	2.59 mm

4.2.1. Step 1: Input Cone

In Figure 4.24, the velocities taking place in the input cone is investigated at a transmission level. The input of the system is angular velocity and it is assigned as $\vec{\omega}_{in}$. The sign of it is minus according to the determined coordinate frame (Equation 4.53). This velocity is defined in the 2nd frame since the rotation axis of the input cone is $\vec{u}_3^{(2)}$. $\vec{V}_L$ is the tangential velocity of the input cone at $\vec{r}_2$ effective rotation radius that changes as the Z distance is altered (Equation 4.54). To calculate the $\vec{V}_L$, the cross product is carried out in Equation 4.55 and 4.56. The numerical calculations are conducted in between Equation 4.57 and 4.59.

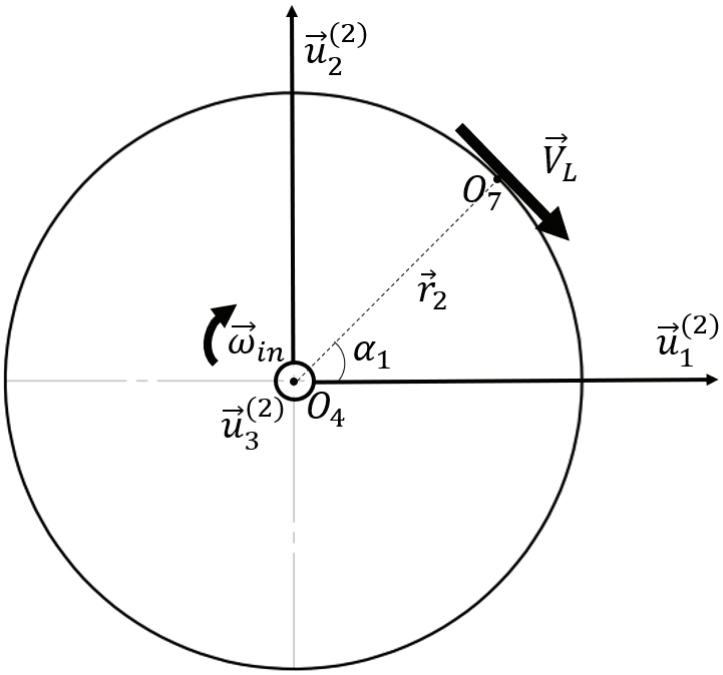

Figure 4.24. The illustration of the velocities taking place on the input cone

$\vec{\omega}_{in}$: Angular velocity of the input cone

$\vec{V}_L$: Linear velocity of the input cone

$$\vec{\omega}_{in} = -\omega_{in}\vec{u}_3^{(2)} \tag{4.53}$$

$$\vec{r}_2 = \cos\alpha_1 r_2 \vec{u}_1^{(2)} + r_2 \sin\alpha_1 \vec{u}_2^{(2)} \tag{4.54}$$

$$\vec{V}_L = \vec{\omega}_{in} \times \vec{r}_2 \tag{4.55}$$

$$\vec{V}_L = r_2 \sin\alpha_1 \omega_{in}\, \vec{u}_1^{(2)} - \cos\alpha_1 r_2\, \omega_{in} \vec{u}_2^{(2)} \tag{4.56}$$

Numerical Calculations:

$$\vec{\omega}_{in} = (-1.04)\vec{u}_3^{(2)} \tag{4.57}$$

$$\vec{r}_2 = (8.0650)\vec{u}_1^{(2)} + (7.1496)\vec{u}_2^{(2)} \tag{4.58}$$

$$\vec{V}_L = (7.4863)\vec{u}_1^{(2)} - (8.4449)\, \vec{u}_2^{(2)} \tag{4.59}$$

4.2.2. Step 2: Sphere

In this step, the angular velocity and the tangential velocity of the sphere are calculated so that the output angular velocity is denoted in terms of input angular velocity.

To do this, first, $\vec{V}_L$ is resolved in the 4th frame (Equation 4.60) since the tangential velocity of the sphere is aligned with $\vec{u}_2^{(4)}$ (Figure 4.25). However, $\vec{V}_L$ has also components along $\vec{u}_1^{(4)}$ and $\vec{u}_3^{(4)}$ as it can be seen in Equation 4.61.

Furthermore, even if $\vec{u}_3^{(4)}$ component of the $\vec{V}_L$ is constrained mechanically to obtain the output angular velocity precisely at a transmission level, it should be considered since it affects the angular velocity of the sphere. In addition, the aforementioned mechanical constraint is achieved through an almost frictionless point type of contact (bearing-sphere) that is mentioned in the previous chapter. Hence, even if the sphere is not allowed to roll around $\vec{u}_1^{(4)}$ or $\vec{u}_2^{(4)}$ axis, it has the capability to rotate at the same Z position.

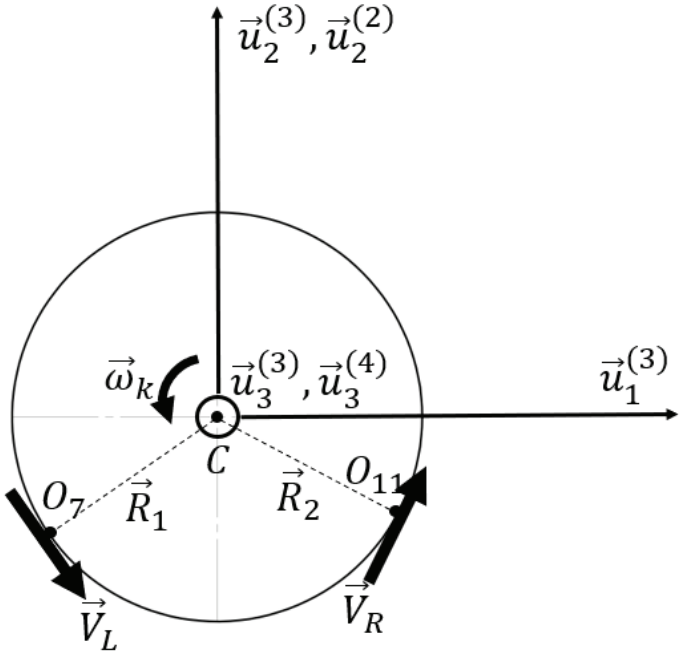

Figure 4.25. The illustration of the velocities taking place on the sphere

$$\bar{V}_L^{(4)} = \hat{C}^{(4,2)}\bar{V}_L^{(2)} \tag{4.60}$$

$$\begin{aligned}\vec{V}_L = {} & [\omega_{in} r_2(\sin\alpha_1 \cos\theta_{11} \cos\theta_{12} - \cos\alpha_1 \sin\theta_{12})]\vec{u}_1^{(4)} \\ & - [\omega_{in} r_2(\cos\alpha_1 \cos\theta_{12} - \sin\alpha_1 \cos\theta_{11} \sin\theta_{12})]\vec{u}_2^{(4)} \\ & + [\omega_{in} r_2 \sin\alpha_1 \sin\theta_{11}]\vec{u}_3^{(4)}\end{aligned} \tag{4.61}$$

In the next step, the angular velocity of the sphere is stated as $\vec{\omega}_k$ in Equation 4.62. The radius vector is defined in Equation 4.63, and the cross product is carried out in Equation 4.64 to compute the $\vec{V}_L$. Afterwards, Equation 4.61 and 4.65 are equated to each other to acquire the ω_2 and ω_3 which are written in Equation 4.66 and 4.67. Even if $\vec{u}_1^{(4)}$ component of the $\vec{\omega}_k$ is not desired because it would enforce the sphere to change the Z distance, it is written to prove this situation mathematically in Equation 4.62. It can be perceived clearly from the Equation 4.68 that $\vec{u}_1^{(4)}$ component of the $\vec{\omega}_k$ is removed due to the cross product between the $\vec{\omega}_k$ and $\vec{R}_1$(Equation 4.64).

$$\vec{\omega}_k = \omega_1 \vec{u}_1^{(4)} + \omega_2 \vec{u}_2^{(4)} + \omega_3 \vec{u}_3^{(4)} \tag{4.62}$$

$$\vec{R}_1 = -R_1 \vec{u}_1^{(4)} \tag{4.63}$$

$$\vec{V}_L = \vec{\omega}_k \times \vec{R}_1 \tag{4.64}$$

$$\vec{V}_L = [-R\omega_3]\vec{u}_2^{(4)} + [R_1\omega_2]\vec{u}_3^{(4)} \tag{4.65}$$

$$\omega_3 = \frac{[\omega_{in} r_2 (\cos\alpha_1 \cos\theta_{12} + \sin\alpha_1 \cos\theta_{11} \sin\theta_{12}]}{R_1} \tag{4.66}$$

$$\omega_2 = \frac{\omega_{in} r_2 \sin\alpha_1}{R_1} \tag{4.67}$$

$$\vec{\omega}_k = \omega_2 \vec{u}_2^{(4)} + \omega_3 \vec{u}_3^{(4)} \tag{4.68}$$

After abovementioned calculations, the angular velocity of the sphere is resolved in the 6th frame because the tangential velocity ($\vec{V}_R$) which is tangent to the sphere from the right side is defined in the 6th frame as expressed in Figure 4.18. The necessary rotations are conducted in between Equation 4.69 and 4.71. The resolution of the $\vec{\omega}_k$ in 6th frame is written out in Equation 4.72.

$$\mathcal{F}_4 \rightarrow \mathcal{F}_3 \rightarrow \mathcal{F}_2 \rightarrow \mathcal{F}_5 \rightarrow \mathcal{F}_6$$

$$\bar{\omega}_k^{(2)} = \hat{C}^{(2,4)} \bar{\omega}_k^{(4)} \tag{4.69}$$

$$\begin{aligned} \vec{\omega}_k = {} & [\omega_3 \sin\theta_{11} - \omega_2 \cos\theta_{11} \sin\theta_{12}]\vec{u}_1^{(2)} + [\omega_2 \cos\theta_{12}]\vec{u}_2^{(2)} \\ & + [\omega_3 \cos\theta_{11} + \omega_2 \sin\theta_{11} \sin\theta_{12}]\vec{u}_3^{(2)} \end{aligned} \tag{4.70}$$

$$\bar{\omega}_k^{(6)} = \hat{C}^{(6,2)} \bar{\omega}_k^{(2)} \tag{4.71}$$

$$\begin{aligned}\vec{\omega}_k = [&\omega_2 \cos\theta_{12} \sin\theta_{22} \\ &+ \cos\theta_{21} \cos\theta_{22}(\omega_3 \sin\theta_{11} - \omega_2 \cos\theta_{11} \sin\theta_{12}) \\ &- \cos\theta_{22} \sin\theta_{21}(\omega_3 \cos\theta_{11} + \omega_2 \sin\theta_{11} \sin\theta_{12})]\vec{u}_1^{(6)} \\ &+ [\omega_2 \cos\theta_{12} \cos\theta_{22} \\ &- \cos\theta_{21} \sin\theta_{22}(\omega_3 \sin\theta_{11} - \omega_2 \cos\theta_{11} \sin\theta_{12}) \\ &+ \sin\theta_{22} \sin\theta_{21}(\omega_3 \cos\theta_{11} + \omega_2 \sin\theta_{11} \sin\theta_{12})]\vec{u}_2^{(6)} \\ &+ [\cos\theta_{21}(\omega_3 \cos\theta_{11} + \omega_2 \sin\theta_{11} \sin\theta_{12}) \\ &+ \sin\theta_{21}(\omega_3 \sin\theta_{11} - \omega_2 \cos\theta_{11} \sin\theta_{12})]\vec{u}_3^{(6)}\end{aligned} \tag{4.72}$$

After calculating the $\vec{\omega}_k$, $\vec{V}_R$ is computed by means of Equation 4.73 and 4.74. The resolution of $\vec{V}_R$ in 6th frame is stated in Equation 4.75. The numerical calcuations are studied in between Equation 4.76 and 4.80.

$$\vec{R}_2 = -R_2\vec{u}_2^{(6)} \tag{4.73}$$

$$\vec{V}_R = \vec{\omega}_k \times \vec{R}_2 \tag{4.74}$$

$$\begin{aligned}\vec{V}_R = [&R_2\,(\cos\theta_{21}(\omega_3 \cos\theta_{11} + \omega_2 \sin\theta_{11} \sin\theta_{12}) \\ &+ \sin\theta_{21}(\omega_3 \sin\theta_{11} - \omega_2 \cos\theta_{11} \sin\theta_{12}))]\vec{u}_1^{(6)} \\ &- [R_2(\omega_2 \cos\theta_{12} \sin\theta_{22} \\ &+ \cos\theta_{21} \cos\theta_{22}(\omega_3 \sin\theta_{11} - \omega_2 \cos\theta_{11} \sin\theta_{12}) \\ &- \cos\theta_{22} \sin\theta_{21}(\omega_3 \cos\theta_{11} + \omega_2 \sin\theta_{11} \sin\theta_{12}))]\vec{u}_3^{(6)}\end{aligned} \tag{4.75}$$

Numerical Calculations:

$$\vec{V}_L = (0)\vec{u}_1^{(4)} + (-11.18)\vec{u}_2^{(4)} + (1.47)\vec{u}_3^{(4)} \tag{4.76}$$

$$\vec{\omega}_k = (0)\vec{u}_1^{(4)} + (0.08)\vec{u}_2^{(4)} + (-0.63)\vec{u}_3^{(4)} \tag{4.77}$$

$$\vec{\omega}_k = (-0.17)\vec{u}_1^{(2)} + (0.06)\vec{u}_2^{(2)} - (0.61)\vec{u}_3^{(2)} \tag{4.78}$$

$$\vec{\omega}_k = (0.02)\vec{u}_1^{(6)} + (0.09)\vec{u}_2^{(6)} - (0.63)\vec{u}_3^{(6)} \tag{4.79}$$

$$\vec{V}_R = (-11.15)\vec{u}_1^{(6)} + (0)\vec{u}_2^{(6)} - (0.42)\vec{u}_3^{(6)} \tag{4.80}$$

4.2.3. Step 3: Output Cone

In the final step, the output angular velocity is calculated. Since the rotation axes of the output cone is aligned with $\vec{u}_3^{(2)}$, the tangential velocity of the output cone must be in the 2nd frame as well (Figure 4.26). Therefore, $\vec{V}_R$ is resolved in 2nd frame (Equation

4.81 and 4.82). Besides, $\vec{r}_3$ is the effective rotation radius of the output cone (Equation 4.84), and it changes as the Z distance varied. $\vec{\omega}_{out}$ is defined in Equation 4.83. Subsequently, the cross product is carried out in Equation 4.85 to calculate the $\vec{V}_R$ (Equation 4.86).

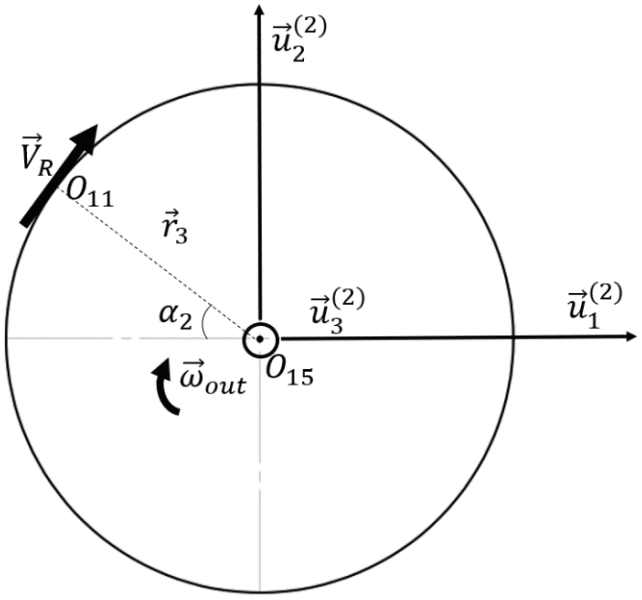

Figure 4.26. The illustration of the velocities taking place on the output cone

$$\bar{V}_R^{(2)} = \hat{C}^{(2,6)}\bar{V}_R^{(6)} \tag{4.81}$$

$$\begin{aligned}\vec{V}_R = [R(&\omega_3 \cos\theta_{11}\cos\theta_{22} \\ &+ \omega_2 \cos\theta_{22}\sin\theta_{11}\sin\theta_{12} \\ &- \omega_2 \cos\theta_{12}\sin\theta_{21}\sin\theta_{22})]\vec{u}_1^{(2)} \\ &+ [R\sin\theta_{22}\,(\cos\theta_{21}(\omega_3\cos\theta_{11} + \omega_2\sin\theta_{11}\sin\theta_{12}) \\ &+ \sin\theta_{21}(\omega_3\sin\theta_{11} - \omega_2\cos\theta_{11}\sin\theta_{12}))]\vec{u}_2^{(2)} \\ &- [R(\omega_3\cos\theta_{22}\sin\theta_{11} \\ &- \omega_2\cos\theta_{11}\cos\theta_{22}\sin\theta_{12} \\ &+ \omega_2\cos\theta_{12}\cos\theta_{21}\sin\theta_{22})]\vec{u}_3^{(2)}\end{aligned} \tag{4.82}$$

$$\vec{\omega}_{out} = -\omega_{out}\vec{u}_3^{(2)} \tag{4.83}$$

$$\vec{r}_3 = -r_3\cos\alpha_2\,\vec{u}_1^{(2)} + r_3\sin\alpha_2\vec{u}_2^{(2)} \tag{4.84}$$

$$\vec{V}_R = \vec{\omega}_{out} \times \vec{r}_3 \tag{4.85}$$

$$\vec{V}_R = r_3\sin\alpha_2\omega_{out}\vec{u}_1^{(2)} + \cos\alpha_2 r_3\,\omega_{out}\vec{u}_2^{(2)} \tag{4.86}$$

Considering the Equation 4.82, there are three components. On the other hand, in Equation 4.86, there are two components which define the pure rotation around the rotation axis of the output cone. The $\vec{u}_3^{(2)}$ component of the $\vec{V}_R$ (Equation 4.82) leads to a slippage along the $+\vec{u}_3^{(2)}$ longitudinal direction (Equation 4.89), and this situation decreases the transmitted power from the input cone to the output cone which is discussed in Figure 5.5. Moreover, this velocity is constrained mechanically in the carriage mechanism (Figure 3.8). Therefore, $\vec{u}_1^{(2)}$ and $\vec{u}_2^{(2)}$ component of the $\vec{V}_R$ which are written in Equation 4.82 and 4.86 are equated to each other, and ω_{out} is calculated in terms of ω_{in} as presented in Equation 4.87 and 4.88.

$$\omega_{out1} = \frac{V_R^{(2)}(1,1)}{r_3 \sin \alpha_2} \tag{4.87}$$

$$\omega_{out2} = \frac{V_R^{(2)}(2,1)}{r_3 \cos \alpha_2} \tag{4.88}$$

Where, $V_R^{(2)}(1,1)$ describes the $\vec{u}_1^{(2)}$ component of the $\vec{V}_R$ (Equation 4.82), and $V_R^{(2)}(2,1)$ states the $\vec{u}_2^{(2)}$(Equation 4.82).

Numerical Calculations:

$$\vec{V}_R = (-4.85)\vec{u}_1^{(2)} + (-10.03)\vec{u}_2^{(2)} + (0.38)\vec{u}_3^{(2)} \tag{4.89}$$

$$\omega_{out1} = -0.4414 \text{ rad/sec} \tag{4.90}$$

$$\omega_{out2} = -0.4472 \text{ rad/sec} \tag{4.91}$$

The difference between the Equation 4.90 and 4.91 is 0.0058.

4.3. Output Velocity Verification

In order to verify the output angular velocity calculations, simulation work is carried out both in Solidworks 2017 (Figure 4.27) and ADAMS 2017.1. In both of these simulations, the output angular velocity is measured at different diameter ratios. Angular velocity is given from the input cone as an input, and the angular velocity of the output cone is obtained as a simulation result. Second, the derived formula (Equation 4.88) is used to observe the variations of the output angular velocity with respect to the Z distance. Finally, the comparison between the simulation data and the computed data is performed to verify the derived velocity level kinematic relations. In the simulation; the stiffness, damping, static and kinetic friction coefficients are defined for the contact point. Acrylic

is chosen as a material for all three bodies since reliable data are obtained. The simulation parameters defined for both Solidworks (SW) and ADAMS are indicated in Table 4.3. Also, these parameters related to contact point are recommended in Solidworks Motion as a default values.

Table 4.3. Simulation parameters of the CVT

Simulation Parameters	
Input angular speed	0.349 rad/sec
Gravitational acceleration	9806.65 mm/s^2
Stiffness	1149.92 N/mm
Damping	0.58 N/(mm/s)
μ_s	0.15
μ_k	0.10
Solver	WSTIFF
Step size	0.001

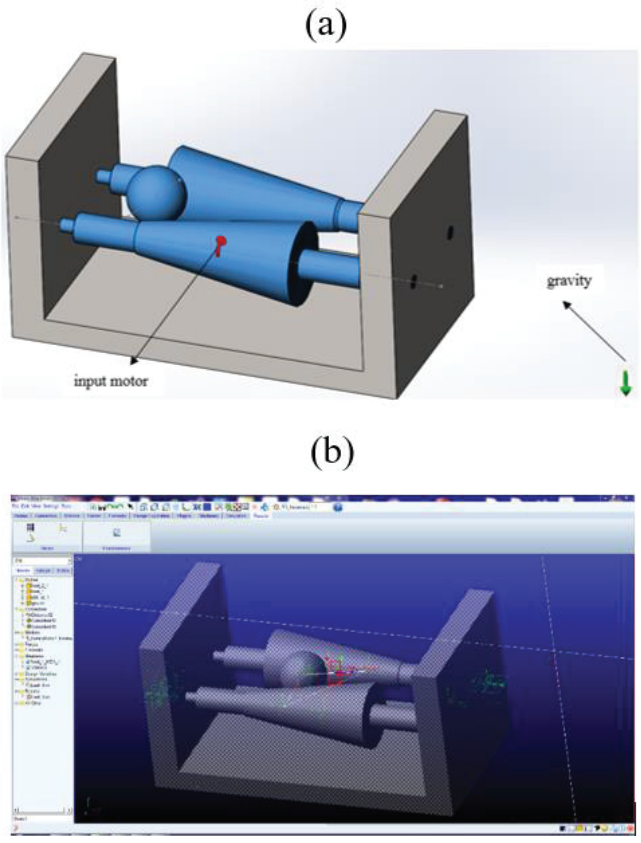

Figure 4.27. Isometric view of the simulation created in (a) SW (b) ADAMS

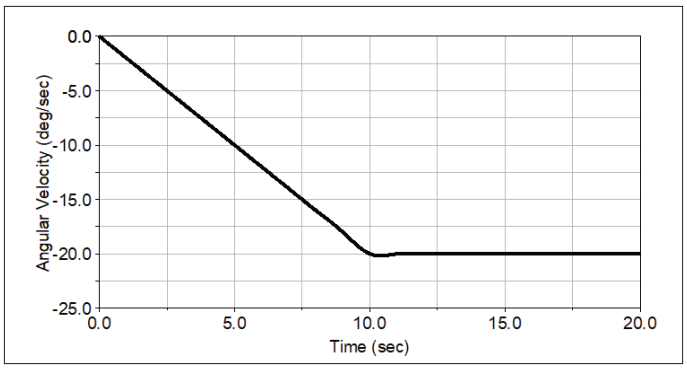

Figure 4.28. The velocity signal given to the input cone

In Figure 4.28, the input speed signal, which is applied gradually to the input cone to overcome the dynamic effects, is illustrated. Because of the selected coordinate frame, the sign of the speed is negative.

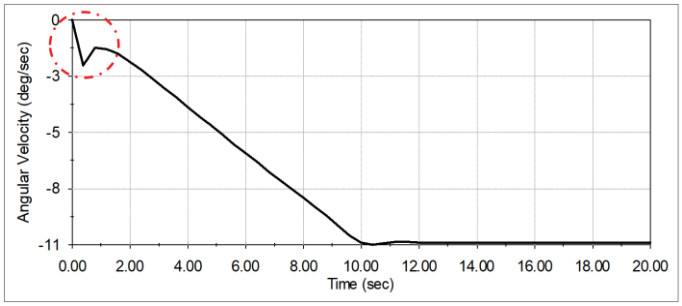

Figure 4.29. The output velocity signal for Z is equal to 15 mm

In Figure 4.29, the output velocity signal, which is obtained from Solidworks for Z is equal to 15 mm, is illustrated. At the start-up regime, the signal sharply raises and then continues to increase in the negative direction. The reason for this sudden jump originates from the mate relation between the cones and the sphere in both Solidworks and ADAMS. The contact points of the sphere cannot be defined as tangent between the cones since the power is not transmitted from the input cone to the output cone with the help of the sphere in this way. The recommended solution to achieve this task is defining the contact points tangent initially. Afterwards, this relation is removed, and the simulation is started. At that instant, the sphere penetrates the cones for an instantaneous time and then it moves above the cones and accomplishes the task. This leads to jump in the graph.

The simulations are conducted for six test points by changing the location of the sphere with the help of the Z parameter. In Table 4.4, the effective rotation radii, simulation results including ADAMS and Solidworks and the errors computed with respect to simulative data are demonstrated. The simulation results are obtained at the steady-state condition in which signal is settled at a predetermined velocity. This interval is chosen between 14 s and 20 s (Figure 4.29) for all Z distances. Afterwards, the average value is computed and presented in Table 4.4. The unit of the radii is in mm, and speeds are rad/s.

Table 4.4. The simulation results of the velocity verification

Z	Input Radius (mm)	Output Radius (mm)	Solidworks (rad/s)	Adams (rad/s)	Calculated (rad/s)	Solidworks Error %	Adams Error %
12	12.18	23.58	0.1798	0.1751	0.1791	0.4088	2.2585
15	12.63	23.13	0.1901	0.1856	0.1895	0.3238	2.0980
20	13.38	22.38	0.2081	0.204	0.2046	1.7143	0.2895
38	16.08	19.68	0.2845	0.2823	0.2847	0.0583	0.8469
50	17.88	17.89	0.3482	0.3481	0.3490	0.2123	0.2372
71	21.03	14.74	0.4972	0.504	0.4996	0.4826	0.8883
Average error %						**0.5334**	**1.1031**

According to the simulation results, the error is observed among all studies. In the 1st, 2nd, 3rd and 4th simulations that are indicated concerning the Z values (12, 15, 20, 38), the calculated speed is between the Solidworks and ADAMS data. In the 5th and 6th study, the theoretical velocity is slightly greater than simulation results. The reason for these errors originates from the contact point definition in simulations. Even if all the theoretical calculations are performed under the assumption of complete rigidity, it is impossible to define this type of contact in simulations. The friction properties should be used for the contacts. Also, the step size of the Solidworks simulation is 0.000000001. On the other hand, ADAMS is 0.001. The reason for this dissimilarity originates from the numerical calculations. The computer that was used for simulations is not capable of performing smaller step sizes. The purpose of the verification of the velocity is to validate the kinematics. Therefore, these errors can be taken as acceptable values within the numerical error range.

In Figure 4.30, the correlation between the simulation data and the calculated data are presented to observe the variations between them for all Z values. It is expected that the output velocity increases with Z distance since the output effective radius is at the maximum level at the initiation point (Figure 4.4). There is a nonlinear relationship between the velocity and Z term since there is a number of nonlinear terms that is observed in Equation 4.88.

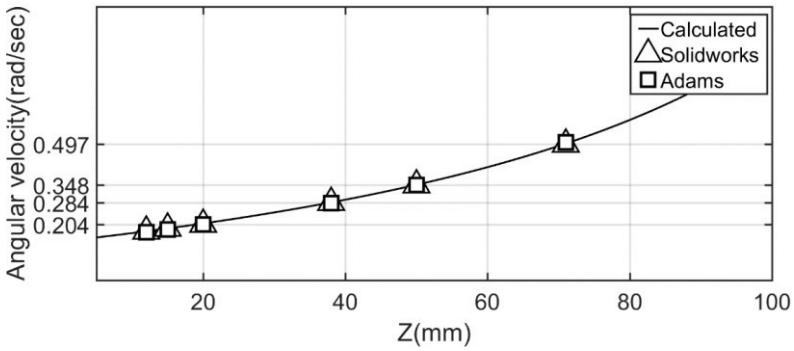

Figure 4.29. The correlation of the simulation data with respect to Z distance

In Figure 4.31, the simulation data is illustrated with respect to the calculated data. The correlation of the simulation data with the calculated velocities can be clearly observed in both figures.

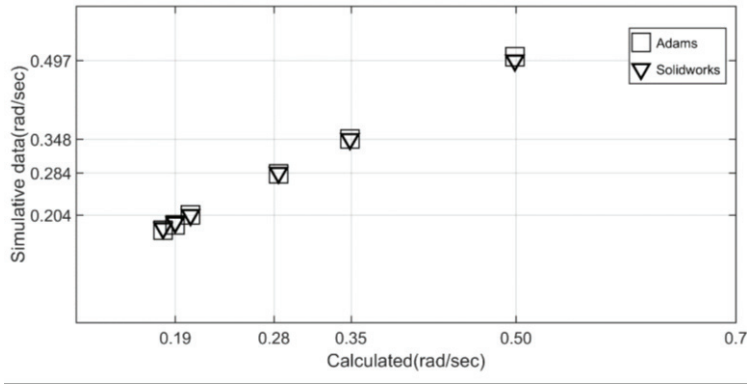

Figure 4.30. The correlation of the simulation data with respect to calculated data

In the Chapter 5, the design optimization is discussed by making use of the static force analysis of the drive.

CHAPTER 5

DESIGN OPTIMIZATION BASED ON STATIC FORCE ANALYSIS

In this chapter, the optimization methodology of the CVT is discussed based on the static force analysis of the drive system. To achieve this, firstly, free body diagram of double cone-sphere system is evaluated. All the calculations that are presented here are carried out assuming all the components are perfectly rigid. Also, the system is assessed as a quasi-static case, and the output torque variations as a function Z distance is obtained.

Secondly, design optimization is implemented by examining the effects of the design parameters on the output torque and the intended haptic scenario. The detailed strategy of the design optimization is mentioned after the quasi-static force analysis in section 5.2.

Furthermore, a similar calculation strategy that is used for velocity analysis is followed for the static force analysis. In other words, parametric calculations are examined and then numerical calculations are performed according to the first prototype dimensions stated in Table 5.1.

Table 5.1. The values to be used for calculations of the static force analysis

R ($\left\|\overrightarrow{CO_7}\right\|$):	17.5 mm
r_1 ($\left\|\overrightarrow{O_1O_2}\right\|$):	10 mm
L ($\left\|\overrightarrow{O_{30}O_{31}}\right\|$):	101.12 mm
θ:	0.14 rad
α_1:	26.12°
α_2:	41.55°
D:	59 mm
τ_{in}:	10 mNm
Z:	2.59 mm

5.1. Static Force Analysis

In this section, the static force analysis is presented step by step for three bodies including input cone, sphere and output cone.

5.1.1. Step 1: Sphere

Free-body diagram of the sphere is presented in Figure 5.1.

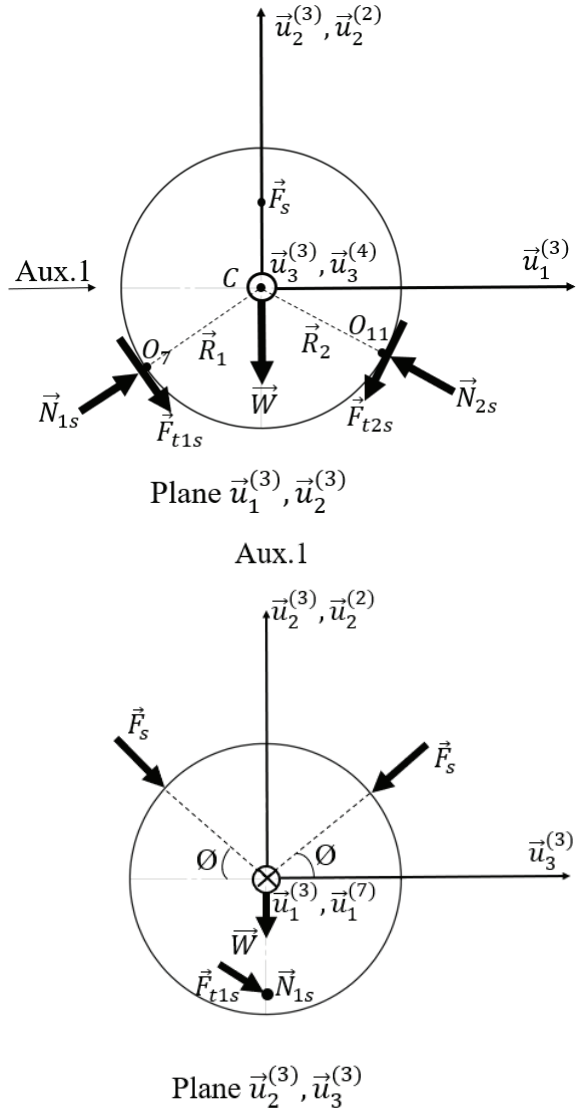

Figure 5.1. The illustration of the forces and moments acting on the sphere

F_S represents the pretension spring force acting on the sphere. Normal forces acting from the left cone and right cone to the sphere are defined as $\vec{N}_{1s}$ and $\vec{N}_{2s}$, respectively (Equation 5.2 and 5.3). Also, the tangential forces formed between the left cone and right cone contact points are denoted as $\vec{F}_{t1s}$ and $\vec{F}_{t2s}$ in Equation 5.6 and 5.7. The direction of the all forces are written with respect to the assigned coordinate frames indicated in Figure 4.13 and 4.18. To present the forces in the same matrix equation, all elements should be resolved in 2nd frame (Equation 5.4, 5.5, 5.8 and 5.9). Hence:

$$\overrightarrow{W} = -(mg + 2F_S \sin\emptyset)\vec{u}_2^{(2)} \tag{5.1}$$

where m is the mass of the sphere.

$$\vec{N}_{1s} = N_{1s}\vec{u}_1^{(4)} \tag{5.2}$$

$$\vec{N}_{2s} = N_{2s}\vec{u}_2^{(6)} \tag{5.3}$$

$$\bar{N}_{1s}^{(2)} = \hat{C}^{(2,4)}\bar{N}_{1s}^{(4)} = N_{1s_1}\bar{u}_1^{(2)} + N_{1s_2}\bar{u}_2^{(2)} + N_{1s_3}\bar{u}_3^{(2)} \tag{5.4}$$

$$\bar{N}_{2s}^{(2)} = \hat{C}^{(2,6)}\bar{N}_{2s}^{(6)} = N_{2s_1}\bar{u}_1^{(2)} + N_{2s_2}\bar{u}_2^{(2)} + N_{2s_3}\bar{u}_3^{(2)} \tag{5.5}$$

$$\vec{F}_{t1s} = -F_{t1s}\vec{u}_2^{(4)} \tag{5.6}$$

$$\vec{F}_{t2s} = -F_{t2s}\vec{u}_2^{(6)} \tag{5.7}$$

$$\bar{F}_{t1s}^{(2)} = -\hat{C}^{(2,4)}\bar{F}_{t1s}^{(4)} = F_{t1s_1}\bar{u}_1^{(2)} + F_{t1s_2}\bar{u}_2^{(2)} + F_{t1s_3}\bar{u}_3^{(2)} \tag{5.8}$$

$$\bar{F}_{t2s}^{(2)} = -\hat{C}^{(2,6)}\bar{F}_{t2s}^{(6)} = F_{t2s_1}\bar{u}_1^{(2)} + F_{t2s_2}\bar{u}_2^{(2)} + F_{t2s_3}\bar{u}_3^{(2)} \tag{5.9}$$

After resolving the all forces in 2nd frame, static force equilibrium is studied. First, all forces acting along $\vec{u}_2^{(2)}$ are equated to zero (Equation 5.10 and 5.11). Afterwards, the same equilibrium is carried out for $\vec{u}_1^{(2)}$ and $\vec{u}_3^{(2)}$ in Equation 5.12, 5.13, 5.14 and 5.15.

$$\sum F_{u_2} = 0; \tag{5.10}$$

$$(-mg - 2F_S \sin\emptyset) + N_{1s_2} + N_{2s_2} + F_{t1s_2} + F_{t2s_2} = 0 \tag{5.11}$$

$$\sum F_{u_1} = 0; \tag{5.12}$$

$$N_{1s_1} + N_{2s_1} + F_{t1s_1} + F_{t2s_1} = 0 \tag{5.13}$$

$$\sum F_{u_3} = 0; \tag{5.14}$$

$$N_{1s_3} + N_{2s_3} + F_{t1s_3} + F_{t2s_3} = 0 \tag{5.15}$$

The calculation of the normal forces in terms of mass of the sphere and the pretension forces are not carried out. It is assumed that there are enough normal forces ($\vec{N}_{1s}$ and $\vec{N}_{2s}$) to transmit the torque from the input cone to the output cone, that is, there is no slippage

in between the cones and the sphere. This situation is experimentally validated, and the details are presented in Chapter 6.

Therefore, only the moments are taken into account to compute the output torque, which is supplied from the output cone, in terms of input torque that is applied from the input cone. Hence, the moment equilibrium about C is written in Equation 5.16.

$$\sum \bar{M}_C = \left[\tilde{R}_1^{(6)} \bar{F}_{t1s}^{(6)}\right] - \left[\tilde{R}_2^{(6)} \bar{F}_{t2s}^{(6)}\right] = \bar{0} \tag{5.16}$$

5.1.2. Step 2: Input cone

In Figure 5.2, the forces and moments acting on the input cone at a Z distance are demonstrated.

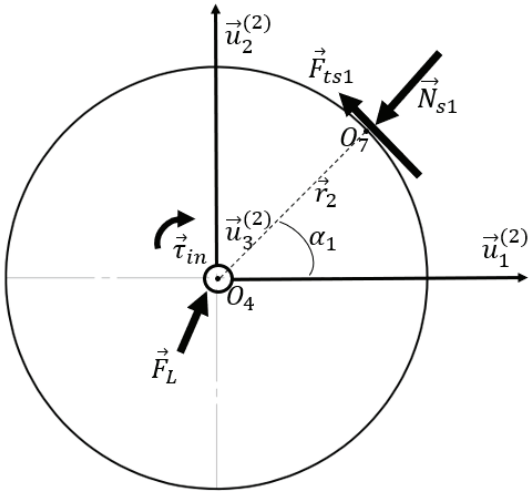

Figure 5.2. The illustration of the forces and moments acting on the left cone

In Figure 5.2, $\vec{F}_L$ represents the reaction forces (Equation 5.18) acting at the rotation axis of the input cone. $\vec{\tau}_{in}$ is the input torque defined in the 2nd frame, and it has three components as presented in Equation 5.27. The component about $\vec{u}_3^{(2)}$ is the input supplied to the system others are the reaction torques. $\vec{r}_2$ is the effective rotation radius, which changes according to the Z distance. $\vec{N}_{s1}$ is equal to the $-\vec{N}_{1s}$. Moreover, $\vec{F}_{ts1}$ is resolved in the 2nd frame so that the $\bar{F}_{t1}^{(2)}$ can be computed in terms of input torque. $\vec{F}_{ts1}$ is the $-\vec{F}_{t1s}$ and the rotation matrix in between frames is used as presented in Equation

5.19 and 5.20. The force equations for the static condition is studied in between Equations 5.17 and 5.26.

$$\bar{N}_{s1}^{(2)} = \hat{C}^{(2,4)}\bar{N}_{1s}^{(4)} = N_{s1_1}\bar{u}_1^{(2)} + N_{s1_2}\bar{u}_2^{(2)} + N_{s1_3}\bar{u}_3^{(2)} \tag{5.17}$$

$$\vec{F}_L = F_{L1}\vec{u}_1^{(2)} + F_{L2}\vec{u}_2^{(2)} + F_{L3}\vec{u}_3^{(2)} \tag{5.18}$$

$$\bar{F}_{ts1}^{(2)} = \hat{C}^{(2,4)}\bar{F}_{t1s}^{(4)} \tag{5.19}$$

$$\begin{aligned}\vec{F}_{ts1} = &-F_{ts1}(\cos\theta_{11}\sin\theta_{12})\vec{u}_1^{(2)} + F_{ts1}(\cos\theta_{12})\vec{u}_2^{(2)} \\ &+ F_{ts1}(\sin\theta_{11}\sin\theta_{12})\vec{u}_3^{(2)}\end{aligned} \tag{5.20}$$

$$\sum F_{u_1} = 0; \tag{5.21}$$

$$N_{s1_1} + (-F_{ts1}(\cos\theta_{11}\sin\theta_{12})) + F_{L1} = 0 \tag{5.22}$$

$$\sum F_{u_2} = 0; \tag{5.23}$$

$$N_{s1_2} + (F_{ts1}(\cos\theta_{12})) + F_{L2} = 0 \tag{5.24}$$

$$\sum F_{u_3} = 0; \tag{5.25}$$

$$N_{s1_3} + F_{ts1}(\sin\theta_{11}\sin\theta_{12}) + F_{L3} = 0 \tag{5.26}$$

Subsequently, equilibrium of moments about O_4 are shown in Equation 5.28.

$$\vec{\tau}_{in} = (\tau_1)\vec{u}_1^{(2)} + (\tau_2)\vec{u}_2^{(2)} - (\tau_{in})\vec{u}_3^{(2)} \tag{5.27}$$

$$\curvearrowleft_{+}\sum \vec{M}_{O_4} = \vec{r}_2 \times \vec{F}_{ts1} - \vec{\tau}_{in} = \vec{0}; \tag{5.28}$$

$$\begin{aligned}&(F_{ts1}r_2\sin\alpha_1\sin\theta_{11}\sin\theta_{12})\vec{u}_1^{(2)} - (F_{ts1}r_2\cos\alpha_1\sin\theta_{11}\sin\theta_{12})\vec{u}_2^{(2)} \\ &+ (F_{ts1}r_2\cos\alpha_1\cos\theta_{12} \\ &+ F_{ts1}r_2\sin\alpha_1\cos\theta_{11}\sin\theta_{12})\vec{u}_3^{(2)} \\ &= -(\tau_1)\vec{u}_1^{(2)} - (\tau_2)\vec{u}_2^{(2)} + (\tau_3)\vec{u}_3^{(2)}\end{aligned} \tag{5.29}$$

$$\tau_1 = F_{ts1}r_2\sin\alpha_1\sin\theta_{11}\sin\theta_{12} \tag{5.30}$$

$$\tau_2 = F_{ts1}r_2\cos\alpha_1\sin\theta_{11}\sin\theta_{12} \tag{5.31}$$

τ_1 and τ_2 are the reaction moments acting on the input cone (Equation 5.30 and 5.31).

In Equation 5.29, there are three unknowns including τ_1, τ_2 and F_{ts1}. Also, there are three equations. r_2 and α_1 are computed from the kinematic analysis introduced in Chapter 4, and the values of them are stated in Table 5.1. Therefore, by substituting these values into the Equation 5.29, τ_1, τ_2 and F_{ts1} are computed in Equation 5.32, 5.33 and 5.34 respectively.

$$\tau_1 = -1.1264 \text{ mN.m} \tag{5.32}$$

$$\tau_2 = 1.2707 \text{ mN.m} \tag{5.33}$$

$$F_{ts1} = 0.9357 \text{ mN.m} \tag{5.34}$$

In order to calculate the F_{t2s}, moments acting around C (Figure 5.1) are equated to zero in Equation 5.35. First, $\vec{R}_1$is defined in the assigned frame in Equation 5.36.

$$\left(\sum_{+} \bar{M}_C = \left[\tilde{R}_1^{(6)} \bar{F}_{t1s}^{(6)}\right] - \left[\tilde{R}_2^{(6)} \bar{F}_{t2s}^{(6)}\right] = \bar{0}\right. \tag{5.35}$$

Where;

The necessary rotations to be computed in Equation 5.35 are implemented in Equation 5.36, 5.37 and 5.38.

$$\vec{R}_1 = -R\vec{u}_1^{(4)} \tag{5.36}$$

$$\bar{R}_1^{(2)} = \hat{C}^{(2,4)} \bar{R}_1^{(4)} \tag{5.37}$$

$$\bar{R}_1^{(6)} = \hat{C}^{(6,2)} \bar{R}_1^{(2)} \tag{5.38}$$

Afterwards, $\vec{R}_2$ is defined according to the assigned coordinate frame (Figure 4.18) in Equation 5.39.

$$\vec{R}_2 = -R\vec{u}_2^{(6)} \tag{5.39}$$

Finally, $\vec{F}_{t1s}$ is resolved in 6th frame in Equation 5.40 and 5.41.

$$\bar{F}_{t1s}^{(2)} = \hat{C}^{(2,4)} \bar{F}_{t1s}^{(4)} \tag{5.40}$$

$$\bar{F}_{t1s}^{(6)} = \hat{C}^{(6,2)} \bar{F}_{t1s}^{(2)} \tag{5.41}$$

$$\begin{aligned} \vec{R}_1 \times \vec{F}_{t1s} = \vec{M}_K \\ = \left[\frac{R\tau_{in} \sin(\theta_{11} - \theta_{21}) \cos\theta_{22}}{r_2(\cos\alpha_1 \cos\theta_{12} + \sin\alpha_1 \cos\theta_{11} \sin\theta_{12})}\right] \vec{u}_1^{(6)} \\ - \left[\frac{R\tau_{in} \sin(\theta_{11} - \theta_{21}) \sin\theta_{22}}{r_2(\cos\alpha_1 \cos\theta_{12} + \sin\alpha_1 \cos\theta_{11} \sin\theta_{12})}\right] \vec{u}_2^{(6)} \\ + \left[\frac{R\tau_{in} \cos(\theta_{11} - \theta_{21})}{r_2(\cos\alpha_1 \cos\theta_{12} + \sin\alpha_1 \cos\theta_{11} \sin\theta_{12})}\right] \vec{u}_3^{(6)} \end{aligned} \tag{5.42}$$

where $\vec{M}_K$ is the total moment (Equation 5.42), which occurs because of the tangential force. In this case, while $\vec{u}_3^{(6)}$ points out the moment transmitted from input cone to the output cone, $\vec{u}_2^{(6)}$, and $\vec{u}_1^{(6)}$ force the sphere to move to a Z distance. However, it is prevented mechanically. Therefore, the assessment of these components is necessary for the efficiency of the transmission capability, which is discussed in the design optimization (Section 5.2) in detail.

$\vec{F}_{t2s}$ is already defined in Equation 5.7. Therefore, by substituting the numerical values into the Equation 5.35, $\left|\vec{F}_{t2s}\right|$ is calculated in Equation 5.43.

$$F_{t2s} = 0.9353 \text{ mN} \tag{5.43}$$

5.1.3. Step 3: Output Cone

As a final step, the static force analysis of the output cone is conducted. All forces and moments are resolved in 2nd frame since the rotation axes of the output cone is $\vec{u}_3^{(2)}$.

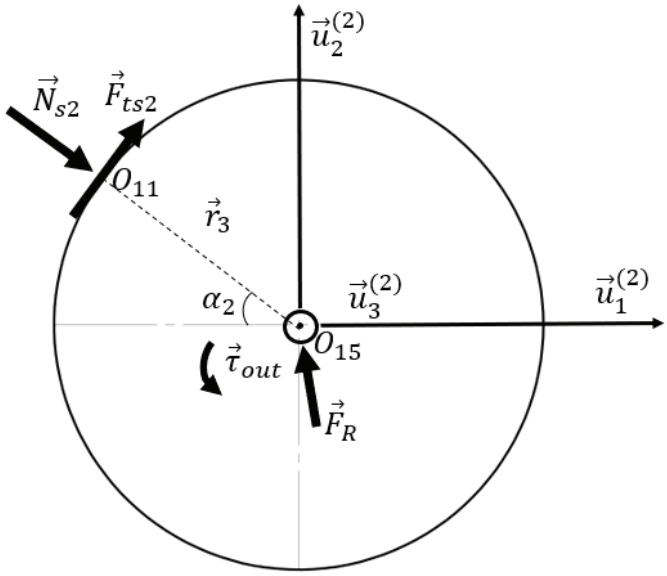

Figure 5.3. The illustration of the forces and moments acting on the right cone

In Figure 5.3, $\vec{F}_R$ represents the reaction forces (Equation 5.46) taking place at the rotation axis of the output cone. $\vec{N}_{s2}$ is equal to the $-\vec{N}_{2s}$ (Equation 5.44). Afterwards, $\vec{F}_{ts2}$ is equal to the $-\vec{F}_{t2s}$, and it is rotated from the 6th frame to 2nd frame (Equation 5.45).

$$\bar{N}_{s2}^{(2)} = \hat{C}^{(2,4)}\bar{N}_{2s}^{(4)} = N_{s2_1}\bar{u}_1^{(2)} + N_{s2_2}\bar{u}_2^{(2)} + N_{s2_3}\bar{u}_3^{(2)} \tag{5.44}$$

$$\bar{F}_{ts2}^{(2)} = \hat{C}^{(2,6)}\bar{F}_{t2s}^{(6)} \tag{5.45}$$

$$\vec{F}_R = F_{R1}\vec{u}_1^{(2)} + F_{R2}\vec{u}_2^{(2)} + F_{R3}\vec{u}_3^{(2)} \tag{5.46}$$

Forces acting along $\vec{u}_1^{(2)}$ are equated to zero in Equation 5.47 and 5.48.

$$\sum F_{u_1} = 0; \tag{5.47}$$

$$N_{s2_1} + F_{ts2_1} + F_{R1} = 0 \tag{5.48}$$

Afterwards, the static equilibrium is studied along $\vec{u}_2^{(2)}$ in Equation 5.49 and 5.50.

$$\sum F_{u_2} = 0; \tag{5.49}$$

$$N_{s2_2} + F_{ts2_2} + F_{R2} = 0 \tag{5.50}$$

Finally, $\vec{u}_3^{(2)}$ components of the forces acting on the output cone are equated to zero in Equation 5.51 and 5.52.

$$\sum F_{u_3} = 0; \tag{5.51}$$

$$N_{s2_3} + F_{ts2_3} + F_{R3} = 0 \tag{5.52}$$

After the force calculations, the moment equilibrium is studied about O_{15}. $\vec{\tau}_{out}$ has three components as stated in Equation 5.53. Its component about $\vec{u}_3^{(2)}$ is the output torque, and the others are the reaction torques acting on the output cone (Equation 5.55 and 5.56).

To compute the output torque, the moments taking place around O_{15} are equated to zero as illustrated in Equation 5.54.

$$\vec{\tau}_{out} = (\tau_{1out})\vec{u}_1^{(2)} + (\tau_{2out})\vec{u}_2^{(2)} + (\tau_{out})\vec{u}_3^{(2)} \tag{5.53}$$

$$\vec{\tau}_{out} - \left(\vec{r}_3 \times \vec{F}_{t2s}\right) = 0 \tag{5.54}$$

$$\tau_{1out} = \frac{r_3 \sin\alpha_2 \tau_{in} \cos(\theta_{11} - \theta_{21}) \cos\theta_{22} \sin\theta_{21}}{r_2(\cos\alpha_1 \cos\theta_{12} + \sin\alpha_1 \cos\theta_{11} \sin\theta_{12})} \tag{5.55}$$

$$\tau_{2out} = \frac{r_3 \cos\alpha_2 \tau_{in} \cos(\theta_{11} - \theta_{21}) \cos\theta_{22} \sin\theta_{21}}{r_2(\cos\alpha_1 \cos\theta_{12} + \sin\alpha_1 \cos\theta_{11} \sin\theta_{12})} \tag{5.56}$$

$$\boldsymbol{\tau_{out} = \tau_{in} \frac{r_3}{r_2} \delta} \tag{5.57}$$

where

$$\delta = \frac{\cos(\theta_{11} - \theta_{21})(\cos\alpha_2 \sin\theta_{22} + \sin\alpha_2 \cos\theta_{21} \cos\theta_{22})}{\cos\alpha_1 \cos\theta_{12} + \sin\alpha_1 \cos\theta_{11} \sin\theta_{12}} \tag{5.58}$$

Equation 5.57 states the mathematical model of the CVT in the static case. To observe the relation between the output torque and Z distance, the verification of output torque with respect to the same input torque as a function of Z distance is graphed by using abovementioned numerical results (Figure 5.4). The graph presented in Figure 5.4 has a nonlinear trend as there are a number of nonlinear terms indicated in Equation 5.58. Also, since all formulas are written according to Figure 4.1, it is reasonable that output

torque reduces with the increment of Z distance. The reason for this situation comprises of the decrease of the $|\vec{r}_3|$.

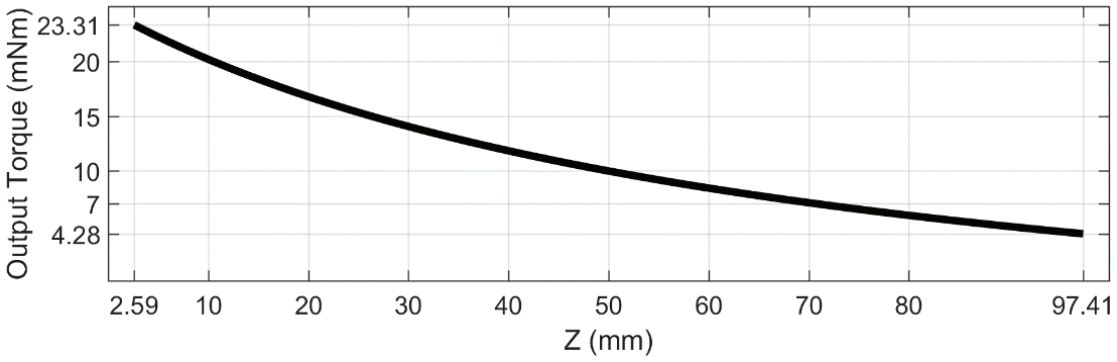

Figure 5.4. Output torque versus Z graph

In addition, power transmission is studied by comparing the input power with output power. Input power is computed with the help of input torque and input speed. Output power is calculated by multiplying the output torque (Equation 5.57) with output speed (Equation 4.88). According to Figure 5.5, there is an average of 0.05 mW difference between the input and output power. The issue stems from $\vec{u}_3$ component of $\vec{V}_R$. This component gives rise to slippage and decreases the output power since this velocity cannot be transmitted to the output cone. However, there is a mechanical constraint for this motion. Therefore, it is observed as a power loss in Figure 5.5.

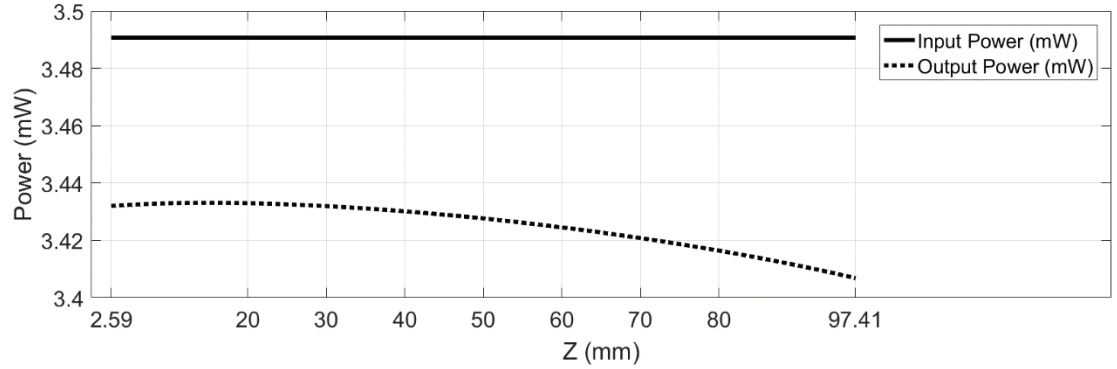

Figure 5.5. Power transmission versus time graph

5.2. Design Optimization

In this section, the design optimization of the CVT is investigated. It is indicated in Chapter 4 that there are five design parameters including R, r_1, L, D, θ . Therefore, the aim of this section is to minimize these design parameters with respect to the first prototype. The handle dimensions and the force capacity of the Hapkit v2.0 (Figure 5.5) is utilized to design the new CVT (Figure 5.6) in order to compare the resultant design with an existing haptic system. The primary reason for minimization is that the inertia of the cones have an adverse effect on the backdrivability performance of the system.

Besides, thanks to CVT design, it is aimed to reach the same output force by making use of a smaller motor than Hapkit. To realize this, the intended haptic scenario is mentioned in the 3rd optimization step.

Furthermore, in Hapkit, the motor is directly coupled with the drive wheel (Figure 5.6). However, in new CVT, there is a transmission system between the drive wheel and the motor coupled with the input cone (Figure 5.7). Therefore, in order to avoid the confusion, the torque of the input cone is defined as input torque (τ_{in}), and the torque that is supplied from the output cone is defined as $\tau_{drive\ wheel}$ because they are coupled with each other (Figure 5.7). Also, the same modification should be implemented by changing the name of the τ_{out} as $\tau_{drive\ wheel}$ in Equation 5.57 since all the calculations related to the optimization is devised according to that equation. Hence, modified version of the Equation 5.57 is stated as:

$$\tau_{drive\ wheel} = \tau_{in} \frac{r_3}{r_2} \delta \tag{5.59}$$

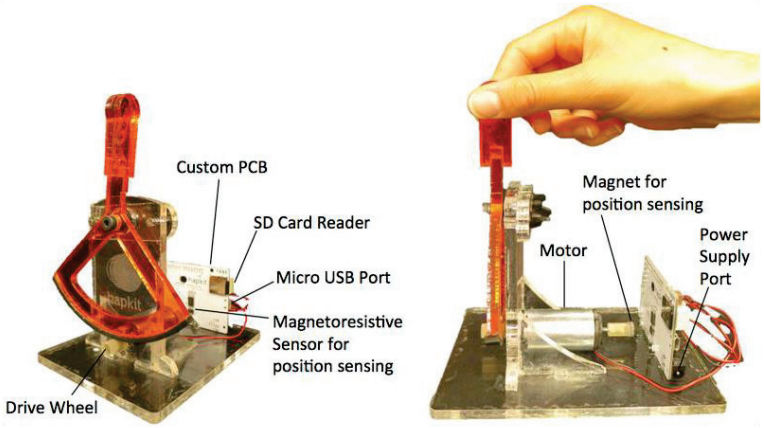

Figure 5.6. Hapkit v2.0 produced in Stanford University
(Source: http://hapkit.stanford.edu/build.html)

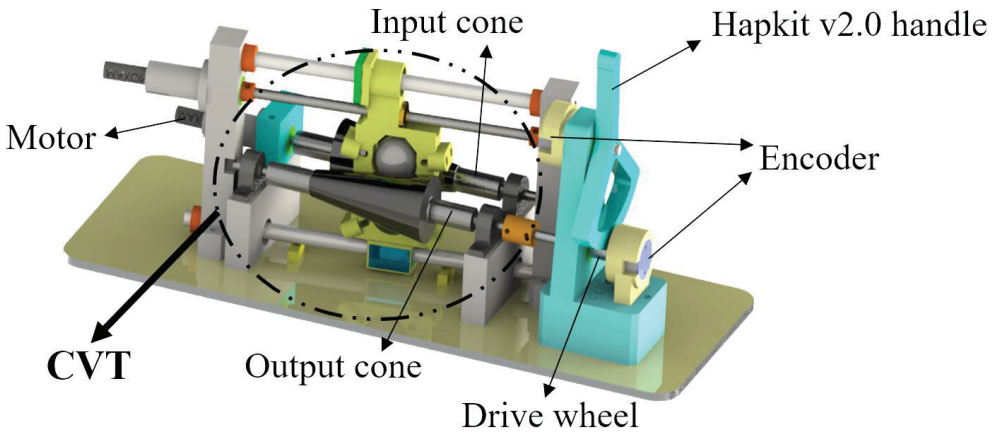

Figure 5.7. The illustration of the first prototype drawing of CVT

5.2.1. Step 1: Output force determination

In this step, the determination of the drive wheel torque ($\tau_{drive\ wheel}$) is investigated. To do this, first, the continuous output force of the HAPKIT v2.0 is considered as a reference (Martinez et al., 2016). It is indicated that the output force is 6 N. Second, handle dimensions of the HAPKIT v2.0 is evaluated and presented in Figure 5.8. All the dimensions illustrated in Figure 5.8 are in mm. Finally, the necessary calculations are performed and stated in between Equation 5.60 and 5.66.

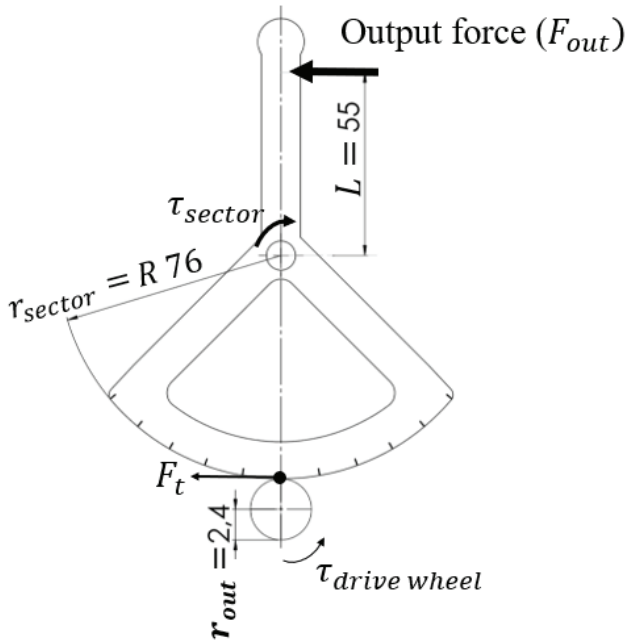

Figure 5.8. The illustration of the dimensions of the HAPKIT v2.0

$$\tau_{sector} = F_{out} L \tag{5.60}$$

$$\tau_{sector} = F_t r_{sector} \tag{5.61}$$

$$\tau_{drive\ wheel} = F_t r_{out} \tag{5.62}$$

Where; F_t is the tangential force taking place between the drive wheel and the sector due to the friction.

$$\tau_{sector} = \tau_{drive\ wheel} \frac{r_{sector}}{r_{out}} \tag{5.63}$$

From the Equation 5.60;

$$F_{out} = \frac{\tau_{sector}}{L} = \tau_{drive\ wheel} \frac{r_{sector}}{r_{out} L} \tag{5.64}$$

Hence, $\tau_{drive\ wheel}$ can be calculated from the Equation 5.64 as follows;

$$\tau_{drive\ wheel} = \frac{F_{out} r_{out} L}{r_{sector}} (c_{SF}) \tag{5.65}$$

By substituting the actual dimensions into the Equation 5.65:

$$\tau_{drive\ wheel} = \frac{(6)(2.40)(55)(1.2)}{(76)} = 12.50 \text{ mN. m} \tag{5.66}$$

Making use of the above equation, the necessary torque acting on the drive wheel is calculated. In Equation 5.65, c_{SF} is defined as a safety factor and it is written in Equation 5.66 as 1.2 multiplier. This value is chosen as a safety factor to tolerate the manufacturing error, backlash, frictions and stiffness in the selection process of the motor. Consequently, the drive wheel torque should be attained from the output cone so that the desired continuous output force is acquired. Theoretically, 7.2 N should be obtained as the output force. However, the reasons mentioned above may reduce this value.

The rest of the optimization steps are contemplated to determine the dimensions of the CVT.

5.2.2. Step 2: Assignment of the ratio of the effective radii

In this step, the ratio of the effective radii between the r_2 and r_{12} is to be selected. This selected as 2 for this study. As a result of this assignment, the CVT has the capability to increase the motor torque $2:1$ and to reduce $1:2$. The mathematical proof of this capability is investigated in the 3rd step.

5.2.3. Step 3: Calculation of the ratio of the nominal and stall torque of the motor

In this step, the ratio between the stall and continuous torque of the motor coupled with the input cone is calculated. In a general haptic device use, it is expected from the haptic device to be backdrivable when the human interacts with it. In this condition, the output impedance (output resistance) is at the minimum level. On the other hand, in a worst scenario in which the maximum impedance is required, the stall torque of the motor is given to the actuator. However, the stall torque can be applied for an instantaneous time. Therefore, to tackle this issue, a haptic scenario is proposed for the new CVT. According to this scenario, the dynamic performance of the motor coupled with the input cone is evaluated. Continuous and the stall torque values of the input motor are associated with the ratio of the radii (r_2 and r_{12}) in which the sphere is at the maximum and minimum Z level corresponding to maximum and minimum reduction ratios. This idea is investigated for two conditions as explained below.

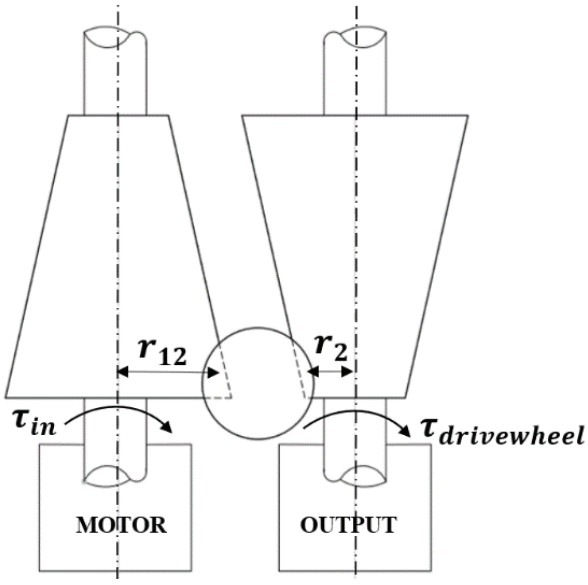

Figure 5.9. The illustration of the minimum transmission level (1st condition)

For the 1st condition that is illustrated in Figure 5.9, the effective output cone radius is adjusted to be at the minimum value (r_2). In a usual case where the user backdrives the haptic device via the handle, the transmission is at this level, and the motor does not supply any torque to resist the motion. On the other hand, when the maximum impedance is desired in order to resist the motion with maximum capability, the stall

torque of the motor is supplied to the system and substituted into the Equation 5.57 as an input torque (τ_{in}) because the transmission reduces the input torque at this condition. If the maximum force to resist the motion is identified by F_{out}, then $\tau_{drivewheel}$ is calculated as $F_{out}L$. At this situation, $\tau_{drivewheel1}$ is generated by the stall torque of the motor as:

$$\tau_{drivewheel1} = \tau_{stall}\frac{r_2}{r_{12}}\delta \tag{5.67}$$

However, stall torque can be applied for a limited period of operation. In order to exert to the user the same amount of F_{out}, the reduction ratio should be changed so that the continuous torque of the motor is used to exert the same F_{out} to the user. This constitutes the 2nd condition.

In Figure 5.10, the second condition, which expresses the maximum torque amplification, is presented. In this case, the motor torque subjected to the input cone should be changed since the motor torque amplification is increased at this transmission level. The solution for this issue is found with the help of the following idea: The continuous torque of the motor is supplied to the system which appears as the input torque (τ_{stall}) and it is aimed to display same F_{out} to the user. Thus, the continuous torque is substituted into the Equation 5.57 and presented as follows:

$$\tau_{drivewheel2} = \tau_{continuous}\frac{r_{12}}{r_2}\delta \tag{5.68}$$

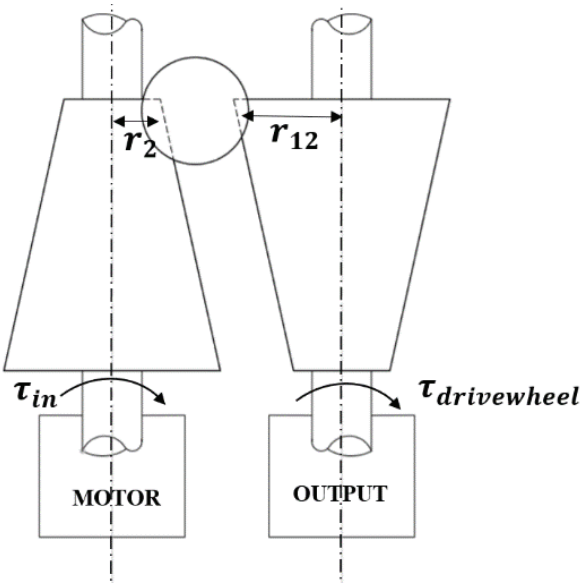

Figure 5.10. The illustration of the minimum transmission level (2nd condition)

During a usual haptic device use scenario, when the backdrivability is in its maximum level and at that instant when the maximum allowable force output is required to be displayed to the user, the stall torque of the motor is given to the input cone. Afterwards, the sphere is moved to the second condition while reducing the input torque of the motor. As the sphere is located at the second condition, the continuous torque is fed to the input cone. The significant point for this actuation strategy is that the transmission variation should be fast enough to comply with the allowable duration specified for stall torque to continuous torque variation so that the device makes the user feel the desired force continuously during this interval.

Therefore, it is aimed to reach the same torques acting on the drive wheel for both two conditions ($\tau_{drivewheel1} = \tau_{drivewheel2} = \tau_{drivewheelmax}$). Hence, Equation 5.68 and 5.67 are used to determine the ratio between the stall torque and the continuous torque of the motor to be used.

$$\frac{\tau_{stall}}{\tau_{continuous}} = \left[\frac{r_{12}}{r_2}\right]^2 \tag{5.69}$$

According to Equation 5.69, the CVT system has the capacity to alter the input torque by the square of the ratio of the effective radii. By substituting the ratio of the radii, which is assigned in the 2nd step as 2, into Equation 5.69, the following equality is found:

$$\frac{\tau_{stall}}{\tau_{continuous}} = \left[\frac{2r}{r}\right]^2 = 4 \tag{5.70}$$

At this point, two significant information including desired $\tau_{drivewheel}$ and the ratio between the stall and continuous torque are attained. Nevertheless, the selection of the motor cannot be achieved yet since there is δ term containing α_2, α_1, θ_{11}, θ_{12}, θ_{21}, θ_{22} in both Equation 5.67 and 5.68. Therefore, in the next step, R, θ, r_1 , D and L are determined.

Further, in Equation 5.69, r_{12} is the largest cone radius as it can also be seen in Figure 4.23. However, r_2 is not the smallest cone radius since the contact point of the sphere with two cones are not on the same horizontal line. That is why Z_{min} and Z_{max} parameters are defined in Equation 4.30 and 4.32. The smallest cone radius is defined as r_1 and the effective cone radius is r_2 in Equation 4.12. In Figure 5.9 and 5.10, r_2 is presented as the smallest effective cone radius. Therefore, Z_{min} is used in Equation 4.10 to compute r_2. This Equation is reconfigured below:

$$r_2 = \tan\theta(Z_{min} + R\sin\theta) + r_1 = r_1 + \tan\theta(2R\sin\theta) \tag{5.71}$$

According to the Equation 5.71, the optimum value of the R, θ and r_1 should be known. These parameters are studied in the 5th step.

5.2.4. Step 4: Definition of the mechanical constraints

In this step, the mechanical constraints including h_{limit}, which is the minimum vertical distance between the spheres, and transmission efficiency are discussed. The relation between the mathematical and physical meanings are stated to acquire the optimum values of the design parameters studied in the next step.

1st Constraint: h_{limit}

To start with first constraint, the h_{limit} parameter (Equations 5.72 and 5.73) is defined and illustrated in Figure 5.12.

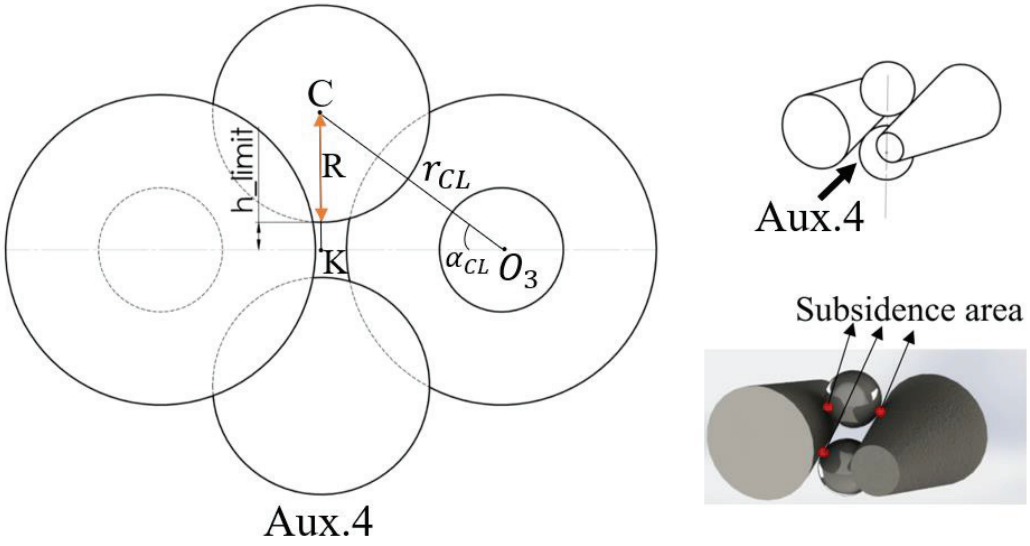

Figure 5.11. The illustration of the h_{limit} parameter

$$\left|\overrightarrow{CK}\right| = r_{CL} \sin \alpha_{CL} \tag{5.72}$$

$$h_{limit} = r_{CL} \sin \alpha_{CL} - R \tag{5.73}$$

For this parameter, the limit is assigned as minimum 2 mm because of two reasons. First, there are two spheres located along the same vertical axis. In order to prevent the contact of the spheres, there should be defined limit. Second, there is a contact between the cones, which are covered with neoprene, and spheres. As a result of this soft

interaction, the subsidence area (Figure 5.11) occurs, and the tolerance of this depth should be considered.

2nd Constraint: Efficiency of the transmission capability

In this criterion, the motion of the sphere related to the transmission performance is evaluated. Indeed, this ability is associated directly with the transmissible upper limit torques, which can be observed from Equation 5.42.

According to Figure 4.13, it is observed that $\vec{u}_2^{(6)}$ component of the $\vec{M}_K^{(6)}$(Equation 5.42) enforces the sphere to move along the Z direction. In other words, the transmission variation happens. This action is not desired, and it is constrained mechanically through the carriage mechanism so that the variation of Z distance is controlled precisely. On the other hand, the moment about $\vec{u}_3^{(6)}$ states the transmitted input torque from the input cone to the output cone.

Furthermore, the most challenging condition is realized if the normal forces acting on the sphere is applied on the same horizontal axis as illustrated in Figure 3.2. In other words, the sphere is not above the cones in this condition. To deal with this issue, the h_{limit} parameter is defined in the previous constraint. Therefore, the worst scenario is eliminated by the help of this constraint.

As a result of these assessments, the following method is chosen to be followed so that the evaluation can be performed relating the ease of the rolling action to the transmission action;

In the optimization iteration methodology that is discussed in the next step, the ratio between $\vec{u}_2^{(6)}$ and $\vec{u}_3^{(6)}$ of the components of the $\vec{M}_K^{(6)}$ is calculated for each iteration. The percentage of $\vec{u}_2^{(6)}$ with respect to $\vec{u}_3^{(6)}$ is named as $M_K\%$. Finally, the results are noted on the iteration table mentioned in the next step.

At the end of these computations, the desired situation is the minimization of this value. To clarify, if the result is 40%, that means the 60% moment is occurred to transmit the input torque. Conversely, if it is 10%, the 90% moment is used for transmission. Therefore, the minimal value is taken into consideration so that the CVT has the potential to transmit the input torque with the maximum efficiency.

5.2.5. Step 5: Iterative method for optimizing R, θ, r_1, L, D parameters

In this step, an iterative method is used to determine the values of the $R, \theta,\ L,\ D$ and r_1 parameters. The initial values of the iteration are chosen as the dimensions of the first prototype. All the lengths are defined in mm, and the angles are in degrees. The iteration is carried out by implementing the calculations in Matlab.

The primary objectives of the iteration are stated as follows:

- ✓ Minimization of the L distance (tolerance 50 mm ±2) and the sphere radius (tolerance 10 mm ± 5)
- ✓ $r_{12}/r_2 = 2$ (tolerance = +0.1)
- ✓ Minimization of the $M_K\%$ (tolerance = 3 ± 2)
- ✓ $h_{limit} = 2$ mm (tolerance = 3 ± 2)

In the first objective, L distance is chosen as 50 mm with tolerance to decrease the inertia of the cones. Afterwards, r_{12}/r_2 is selected as 2 because the ratio between the stall and the continuous torque of the DC motors, which is coupled with the input cone, is around 4 according to the data sheets. Therefore, r_{12}/r_2 should be chosen as 2 according to Equation 5.70. The tolerance of this objective is lower because the ratio of the radii has a significant affect on obtaining the desired force precisely. In the next objective, $M_K\%$ is stated. The tolerance values are selected by considering the first prototype result which was 2.90 shown in Table 5.2. Finally, h_{limit} is assigned as 2 according to the first prototype results. Moreover, the tolerance is given +2 to prevent possible collusions between the spheres.

In Table 5.2, the possible CVT configurations are studied by iteration of the design parameters in the scope of objectives that are stated in the previous page. The meaning of the colors used in Table 5.1 is stated as follows:

The green color is used when the number is within tolerance and red color is utilized to indicate the out of tolerance situation. The dashed line indicates the changed parameter.

The effect of change in design parameters on h_{limit}, r_{12}/r_2 and $M_K\%$ are indicated in Figure 5.12.

Table 5.2. Iterations for obtaining the intended design parameters

	D	r_1	R	L	θ	$M_K\%$	h_{limit}	$\frac{r_{12}}{r_2}$
1	59	10	17.5	101.12	8.53°	2.90	1.13	2.31
2	59	10	17.5	**90**	8.53°	**2.14**	**−0.26**	**2.16**
3	**50**	10	17.5	90	8.53°	**7.89**	**5.32**	**2.16**
4	50	10	17.5	**70**	8.53°	**3.60**	**3.46**	**1.89**
5	50	10	17.5	**60**	**9°**	**3.09**	**2.82**	**1.78**
6	**45**	10	**12.5**	60	**9.5°**	**3.11**	**3.18**	**1.86**
7	45	10	**10**	60	**10°**	**1.97**	**1.42**	**1.92**
8	**42**	10	10	60	**10.5°**	**4.11**	**4.26**	**1.96**
9	**45**	10	10	60	**11.5°**	**3.37**	**2.97**	**2.03**
10	45	10	10	60	**13°**	**5.31**	**4.36**	**2.12**
11	45	10	10	**55**	13°	**4.12**	**3.45**	**2.02**
12	**46**	10	10	55	13°	**3.43**	**2.65**	**2.02**
13	**45**	10	10	**50**	13°	**3.12**	**2.46**	**1.92**
14	45	10	10	50	**15°**	**5.24**	**4.11**	**2.01**
15	**47**	10	10	**50**	**15°**	**3.66**	**2.53**	**2.01**
16	47	10	10	50	**14°**	**2.76**	**1.60**	**1.97**
17	47	**9**	10	50	14°	**1.80**	**−0.74**	**2.06**
18	47	9	10	50	**13°**	**1.17**	**−2.00**	**2.01**
19	**45**	9	10	50	13°	**2.20**	**0.35**	**2.01**
20	**43**	9	10	50	13°	**3.44**	**2.17**	**2.01**
21	43	9	10	50	**12°**	**2.54**	**1.29**	**1.96**
22	43	9	10	50	**12.5°**	**2.97**	**1.74**	**1.99**
23	**42.5**	9	10	50	12.5	**3.29**	**2.15**	**1.99**
24	**43**	**9**	**10**	**52**	**12.5**	**3.34**	**2.13**	**2.03**

According to Figure 5.12, first, if L is reduced, y_2 and $\sin\alpha_{CL}$ diminish from the Equation 4.11 and 4.20. Therefore, h_{limit} value decreases from Equation 5.73. Reduction of D decreases the $\cos\alpha_{CL}$ in Equation 4.20. Hence, h_{limit} increases and $^{r_{12}}/_{r_2}$ is not

affected by this variation. The increase in θ results in the increase of y_1 and y_2. Also, r_2 and r_{12} are affected by this situation in the same fashion as y_1 and y_2 (Equation 4.10 and 4.11).

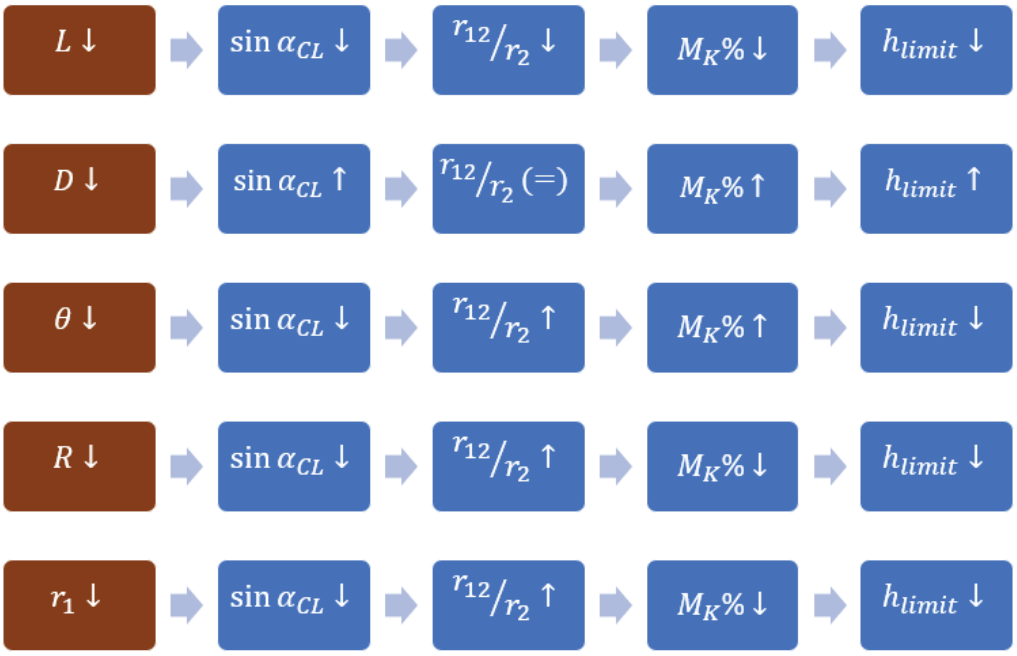

Figure 5.12. The flowchart for the effect of design parameters on the iteration results

In the next case, R is decreased and then $\sin\alpha_{CL}$ also diminishes from the Equation 4.20. Hence, h_{limit} decreases. Finally, if r_1 is reduced, the effect of this is the decrease of $\sin\alpha_{CL}$ (Equation 4.20) and h_{limit} (Equation 5.73). On the other hand, r_2 diminishes from Equation 4.12, and the ratio between the r_{12} and r_2 increases. Furthermore, the evaluation of the $M_K\%$ is performed according to Equation 5.42.

In the light of the above explanations related to the effect of the variation of design parameters on the objectives, the iterations are done and expressed as follows:

In the first iteration, the dimensions of the first prototype are considered as initial parameters. In the 2nd iteration, L is reduced and then h_{limit} decreases sharply below the zero. Hence, D is decreased in the next iteration as a solution to this issue. In the 4th iteration, r_{12}/r_2 moves beyond the tolerance limits because of the reduction of L parameter. Also, this issue can be observed in 5, 6, 7 and 8th iterations. However, as a priority, the aim is to approach to the intended dimensions set for L and R. Hence, in the 5th iteration, L is continued to be decreased without considering the r_{12}/r_2 problem. Also,

R is reduced in the 6th and 7th iterations. The issue related to r_{12}/r_2 is tried to be solved in 5, 6, 7 and 8th iterations by increasing the θ angle; however, the value is still out of tolerance. In addition to this problem, h_{limit} is below 2 mm in the 7th iteration. Therefore, D is diminished. Hence, h_{limit} is reached beyond the upper tolerance in the 8th iteration.

In consequence, h_{limit} is not still in the safe range. In the next iteration, D and θ increased to overcome the issue of r_{12}/r_2 and h_{limit} and this strategy results in positively. In the 10th iteration, θ is increased but the problem occurs related to the $M_K\%$, and h_{limit}. Hence, L is reduced in the next iteration, and h_{limit} is achieved to be within tolerance. However, $M_K\%$ is slightly below the upper tolerance. To reduce this value, D is increased in the 12th iteration. Afterwards, L and D are diminished in 13th iteration to reach the desired values. However, the result is problematic in the aspect of r_{12}/r_2. Accordingly, θ is increased to cope with this issue in the 14th iteration. However, $M_K\%$, and h_{limit} problem is not resolved as a result of this increment. Therefore, D is increased and the result of the 15th iteration is within tolerance for all criteria. However, the iteration is continued to acquire the minimum possible $M_K\%$ due to the fact that this criterion has a prominent role regarding transmission capability.

In the 16th , θ is decreased to minimize the $\%M_K$. However, h_{limit} and r_{12}/r_2 narrow down this reduction of θ value because they appear below the tolerance as a result of this reduction. To tackle with this problem, r_1 is decreased, and r_{12}/r_2 is moved within the tolerance in the 17th iteration. However, in this case, h_{limit} falls below the tolerance. In 19^{th} and 20^{th} iterations, D parameter is reduced, and the desired results are acquired in 20^{th} iteration. However, the minimization of the $M_K\%$ is aimed, and the iteration is continued to examine whether there is a better configuration.

In the next iteration, θ is reduced, and the same issue that occurred in 16th iteration takes place. Thus, θ is increased with a slight difference to acquire the optimum results. At this point, there are two problems including r_{12}/r_2 and h_{limit}. To cope with the h_{limit} issue, D is reduced in the 23rd iteration. Moreover, L is increased to stay within the tolerance range in the last iteration, and the design parameters are acquired at the end of 23 iterations.

5.2.6. Step 6: The selection of the motor for the input cone

In this step, the motor to supply the torque to the input cone is determined since all the terms that appear in Equation 5.67 and 5.68 are already determined in the previous steps. Thus, the numerical values are substituted in Equation 5.74, and the continuous torque of the motor is calculated in Equation 5.75. On the other hand, the stall torque is computed for Equation 5.76 and the result is presented in Equation 5.77.

$$12.50 = (\tau_{continuous})(2)(0.97) \quad 5.74$$

$$\tau_{continuous} = 6.44 \text{ mN m} \quad 5.75$$

$$12.50 = (\tau_{stall})(1/2)(0.97) \quad 5.76$$

$$\tau_{stall} = 25.77 \text{ mN m} \quad 5.77$$

The motor options are presented in Table 5.3. The selection of the motor is carried out by considering the abovementioned torque values. The tolerance for both τ_{stall} and $\tau_{continuous}$ is assigned as plus three ($+3$ mNm) according to the closest option for these torque values from the motor data sheets presented in Table 5.3.

Table 5.3. The motor options of the input cone

	Brand	**Model**	τ_{stall} **(mN m)**	$\tau_{continuous}$ **(mN m)**
1	Maxon	DCX 14L - 4.5V	23.5	6.36
2	Maxon	DCX 14L - 6V	24.8	6.96
3	Maxon	DCX 14L - 9V	27.8	6.88
4	Maxon	DCX 14L - 12V	24.7	6.91
5	Maxon	DCX 14L - 18V	28.5	6.94
6	Maxon	DCX 14L - 24V	22.9	6.66

The closest option is evaluated among the six motors, and the third motor is selected according to the specified tolerance.

5.3. Conclusion

In the final step, new CVT with the optimized parameters is designed in Solidworks (Figure 5.13) and manufactured with the help of a 3D printer (Figure 5.14).

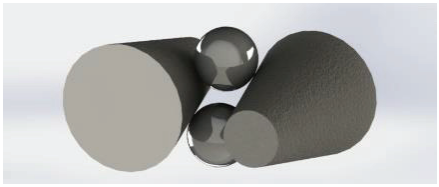

Figure 5.13. The illustration of the 3D drawing of the optimized CVT

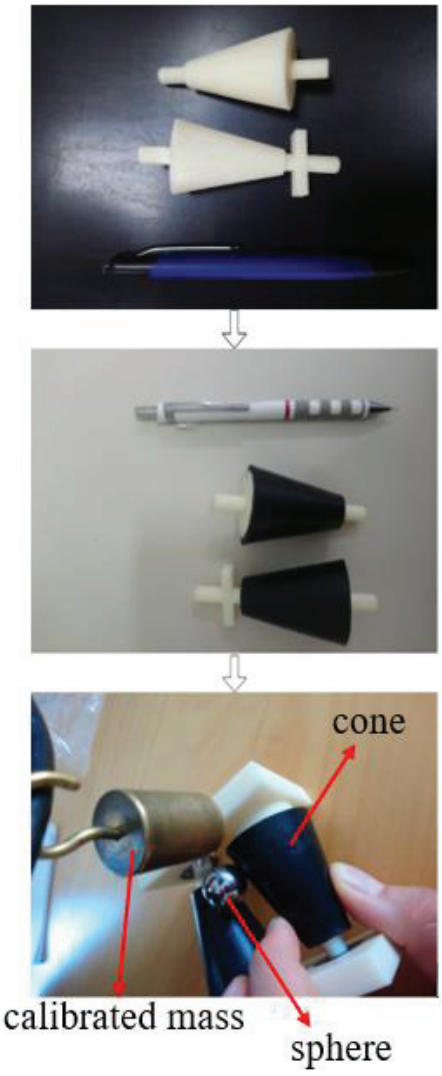

Figure 5.14. The illustration of the 3D printed optimized CVT

Afterwards, the surface of the cones are covered with neoprene, and then a calibrated mass is hung on the input cone. The mass is arranged to apply approximately 40 mN m to the input cone even if the calculated maximum input torque is 25.77 mNm (Equation 5.76). A quick slippage test is conducted without using sensors.

The aim of this test is to observe the possible problems of the manufactured system in the early prototype phase. The 3D drawing of the design is presented in Figure 5.13, and the 3D printed optimized CVT is presented in Figure 5.14.

In Table 5.4, the comparison between the first and optimized prototype (3D printed) is demonstrated. It is clearly seen that *L* parameter is reduced and this leads enhancing the application area of the proposed drive system in human-robot interfaces. For instance, new CVT can be used for a prosthesis or a haptic device as the inertia of the optimized cones have not an adverse effect on the backdrivability. Moreover, thanks to the optimized prototype, the energy consumption is reduced due to the optimized cones.

Table 5.4. The comparison of the first and optimized prototype

	D (mm)	r_1 (mm)	R (mm)	L (mm)	θ (rad)	$(\%)M_4$	$(\%)M_6$	h_{limit} (mm)	$\frac{r_{12}}{r_2}$
1st prototype	59	10	17.5	101.12	8.53°	9.83	9.83	1.13	2.31
Opt-timized prototype	**43**	**9**	**10**	**52**	**12.5°**	**12.79**	**12.79**	**2.13**	**2.03**

In this chapter, static force analysis of the new CVT and the optimization strategy are examined. In the first section (5.1), the system is assumed as a completely rigid body and the output force is computed in terms of the design parameters which are stated as *R*, *L*, θ and r_1. Afterwards, the design optimization is studied by considering the output force of the HAPKIT v2.0. Moreover, in the 5th step, the iteration is performed to acquire the design parameters within the tolerance. Finally, the motor coupled with the input cone is determined.

In the Chapter 6, the mechanical design of the optimized CVT and the tests are presented.

CHAPTER 6

EXPERIMENTAL VERIFICATION OF THE OPTIMIZED PROTOTYPE

In this chapter, the mechanical design details of the optimized prototype and the experimental validation are examined by making use of the contemplated tests that are stated in Chapter 1.

6.1. The constructional design of the optimized prototype

In this section, constructional design details of the optimized prototype are expressed. A 3D drawing of the design is illustrated in Figure 6.1.

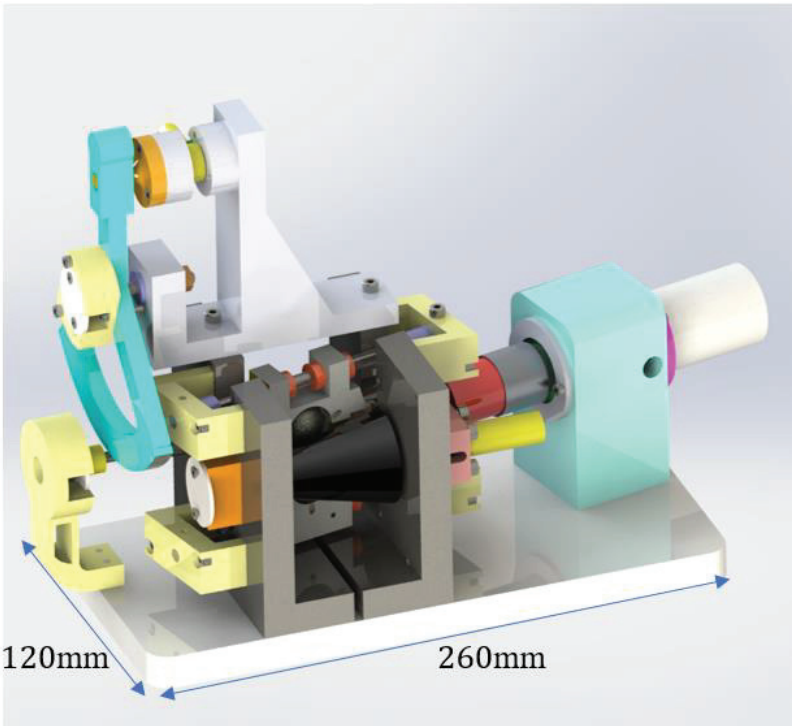

Figure 6.1. The Solidworks drawing of the optimized prototype

In Figure 6.2, the produced prototype is illustrated. In this design, a force sensor (Kistler, type 9017B) is fixed to the handle to measure the output force, Motor-1 (Maxon DCX 14L-9V) is used to apply the input torque to the CVT, and three absolute encoders (MagAlpha, TBMA702-Q-RD-00A) are utilized to observe whether there are slippages between the cones and the spheres, and the capstan drive.

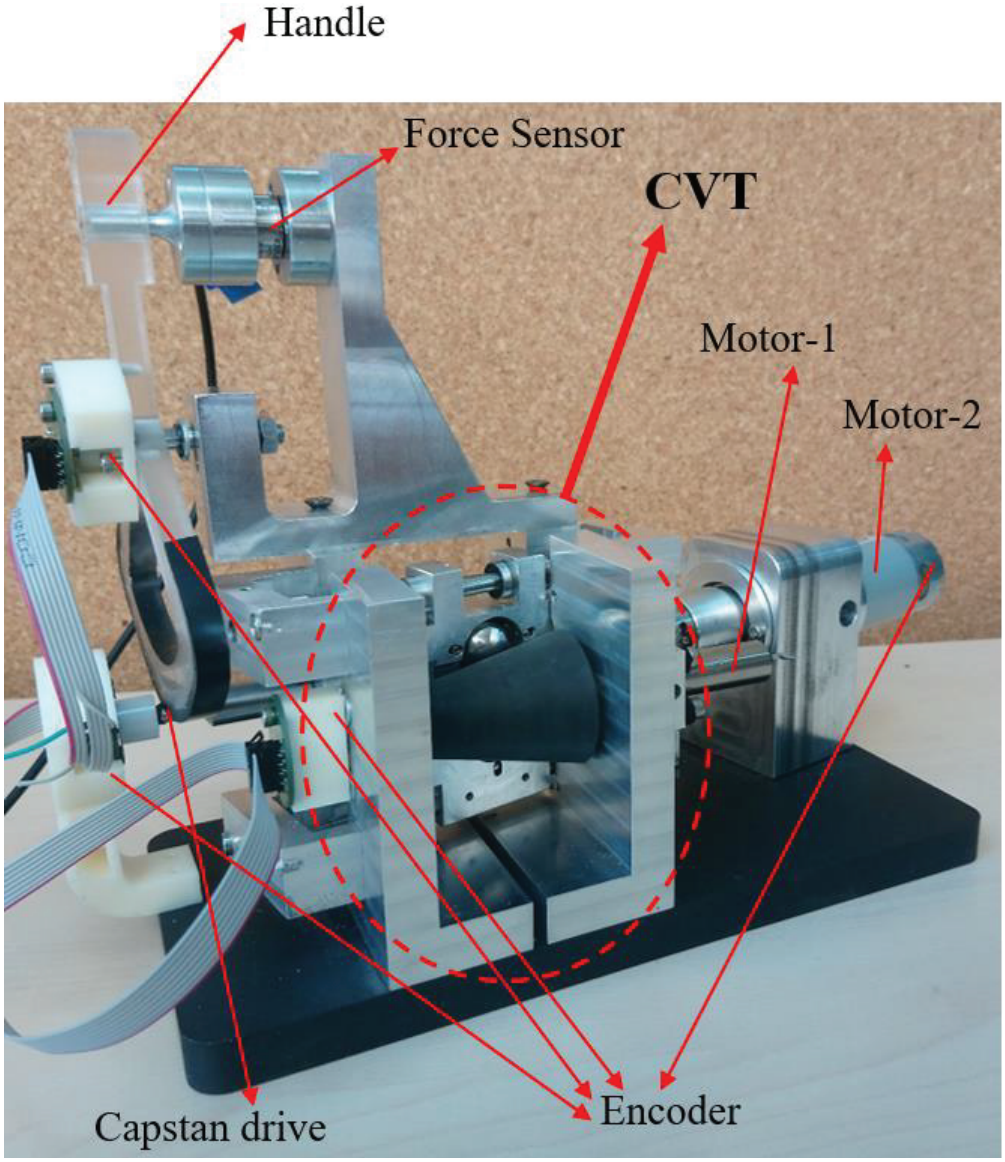

Figure 6.2. The produced prototype

The last encoder is coupled with the Motor-2 so that position control is employed to move the carriage mechanism to change the Z distance. To achieve this, a linear motion system is designed by using a ball screw transmission mechanism.

In the first prototype, the screw is rotated, and the nut is fixed on the carriage mechanism that is constrained to move linearly. However, in the optimized prototype, the ball bearing nut is rotated via Motor-2, and the screw is fixed to the carriage mechanism with the help of the bridge (Figure 6.3). To couple with the ball bearing nut and the motor-2, the shaft is designed and bedded by the help of bearings illustrated in Figure 6.3.

The reason for this modification is to approach the spheres to each other as much as possible because this leads to increase the efficiency of the transmission capability. It is explained in detail in Chapter 5 (5.2.4 section). Otherwise, the screw would lie across the spheres and this situation would give rise to increase the distance between the spheres.

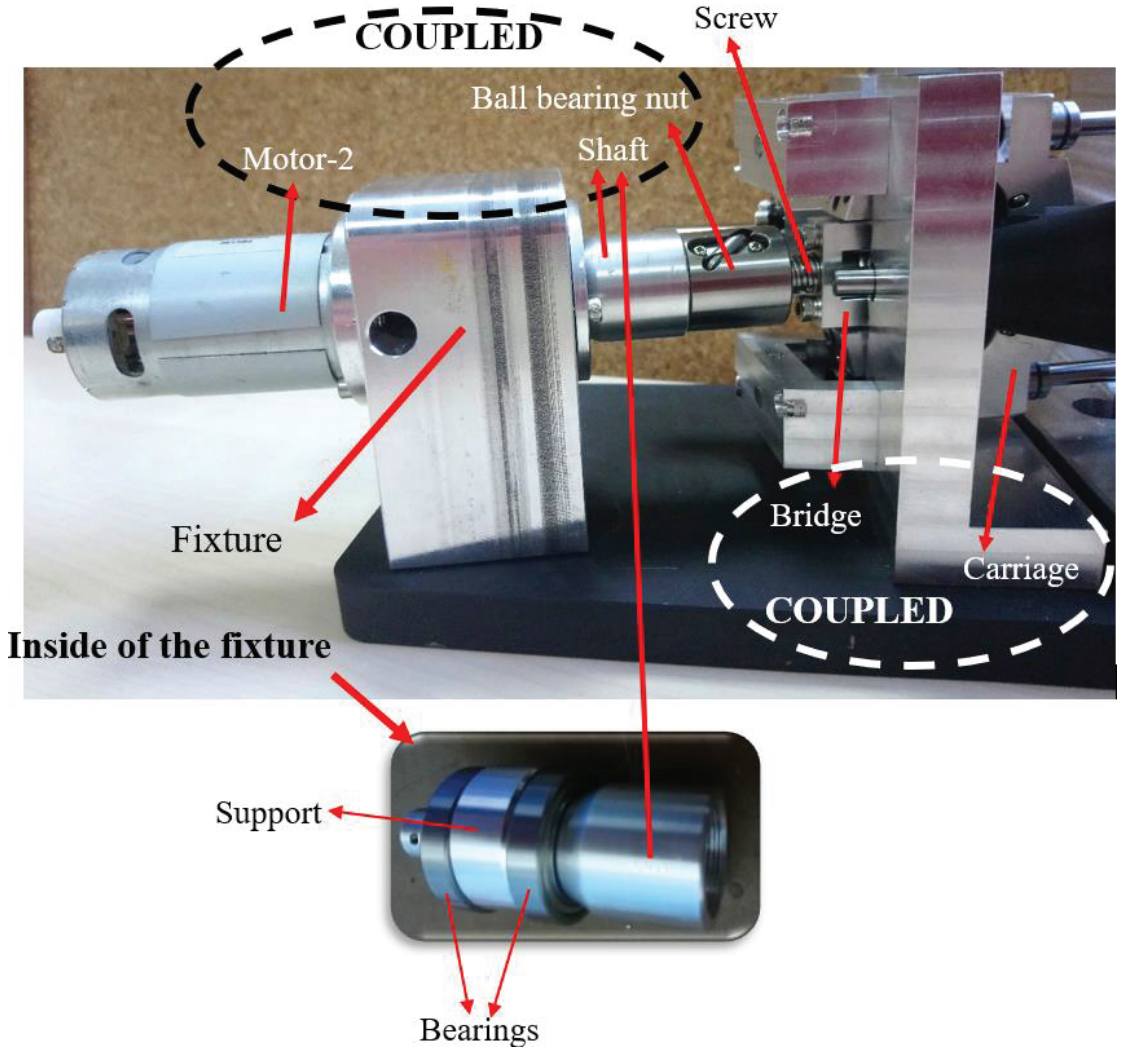

Figure 6.3. The design of the linear motion system

The next modification is implemented regarding the selection of the friction material covered on the cones and the covering operation. In the first prototype, the

friction material was diaphragm rubber. However, the covering process could not be performed precisely because the rubber is cut by the scissors from the layer and covered via the locktite on the cones by hand.

In the optimized prototype, the friction material is chosen as EPDM rubber having 70 shore hardness. The neoprene material used in HAPKIT (Martinez et al., 2016) is the basis for this selection, which has also the same shore value. The friction material is heated and covered on the cones in a circular motion. Finally, the covered cones are grinded with the help of a special grinding machine according to the desired cone angles and the radii.

Finally, the cone angle (θ), the length (L) and the r_1 values are measured through the contactless measurement method since the rubber is an elastic material. To achieve this, the profile projector machine (Mitutoyo) is utilized (Figure 6.4). In this measurement method, the real dimensions of the part is enlarged and the shadow of the part is measured.

Figure 6.4. The measurement of the covered cone via profile projector machine

The measured and the designed cone dimensions are stated in Table 6.1. The difference between them are the manufacturing errors result due to the manufacturing process with grinding, CNC milling and turning machines.

Table 6.1. The comparison between the desired and the measured dimensions of the cones

Cone number	r_1 (mm)	θ (rad)	L (mm)
1 **(Measured)**	9.4635	12.2883°	49.57
2 **(Measured)**	9.4525	12.3122°	50.08
Desired Values	**9**	**12.5°**	**50.76**

Tests are conducted by using the measured dimensions of the cones instead of the designed values so that the manufacturing errors are taken into account.

The next modification is performed on the carriage mechanism. In the second prototype, there is an extra pre-tension mechanism assembled vertically to apply a force to the lower sphere (Figure 6.5). By doing this, the gravitational effects are compensated. The rest of the pre-tension mechanisms are used to cage the sphere between the cones.

In Figure 6.5, the exploded view of the carriage mechanism is illustrated. The elements of the carriage mechanism shown in Figure 6.5 are stated as follows:

1. Sphere
2. Linear bearing
3. Miniature bearing
4. Sanded pin
5. Supportive tool
6. Spring
7. Set-screw
8. Carriage
9. Bridge
10. Bolt

The assembled carriage mechanism is presented in Figure 6.6.

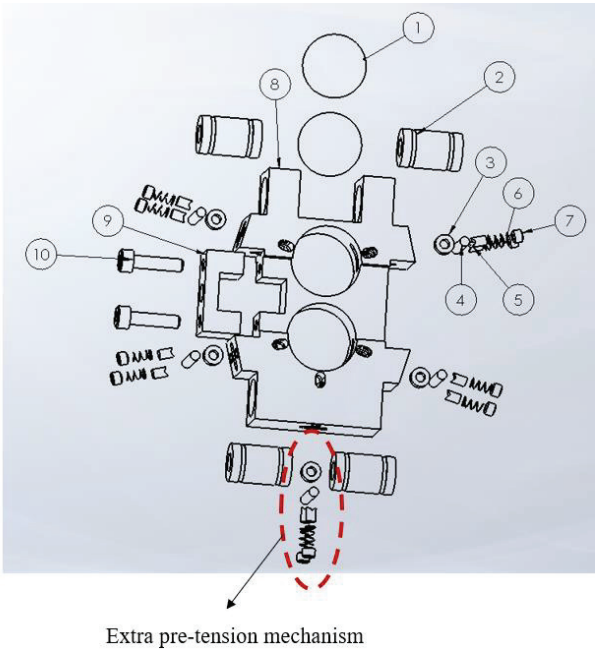

Figure 6.5. The exploded view of the carriage mechanism

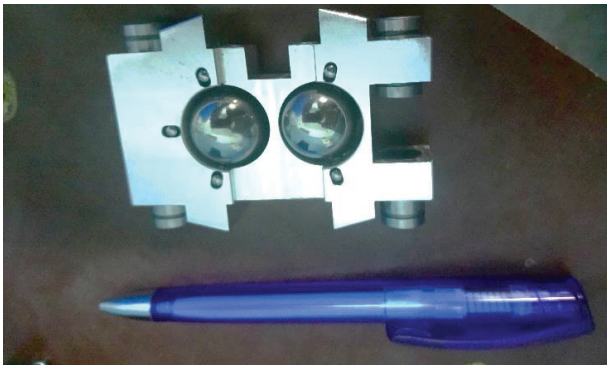

Figure 6.6. The assembled carriage mechanism

In the next section, the test setup is described.

6.2. Experimental Validation

Before starting the tests, the torque constant of Motor-1 is verified. To achieve this, the following experimental setup is constructed (Figure 6.7).

In this experiment, Motor-1 is driven in current control via Escon 36/2 DC Servo Controller.

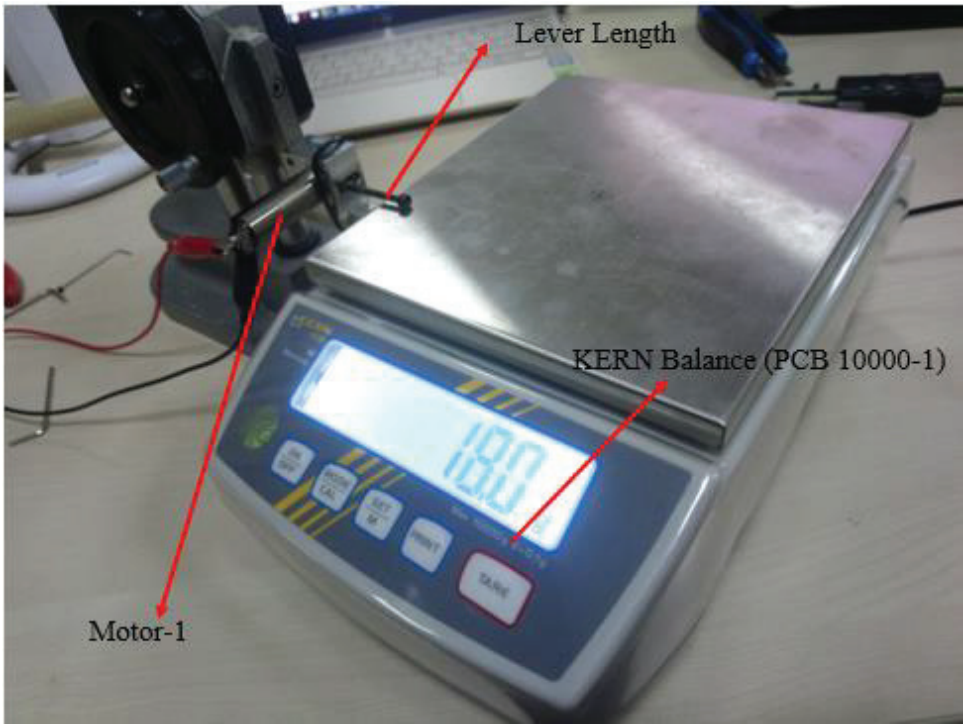

Figure 6.7. The torque constant validation setup of the Motor-1

Specifications of Motor-1 are indicated in Table.6.2.

A variety of current inputs are fed to Motor-1 while measuring the output torques with the help of KERN Balance device. The results are presented in Table 6.3.

Table 6.2. The Specifications of the Motor-1

DCX 14L-9V (Maxon Motor)	
Nominal Voltage	9V
Nominal Torque	6.88 mN m
Nominal Current	0.974 A
Stall Torque	27.8 mN m
Stall Current	3.8 A
Torque Constant	7.3 mN m/A

Table 6.3. Experimental test results for the torque constant verification of Motor-1

Given current (A)	Measured balance value (gr)	Output force value (N)	Torque contribution of the lever weigth (mN m)	Experimentally calculated torque (mN m)	Theoretically calculated torque (mN m)	% Error with respect to theoretical value
0.8	15.2	0.149	0.0462	5.918	5.84	1.322
0.84	15.9	0.155	0.0462	6.192	6.132	0.98
0.88	16.6	0.162	0.0462	6.467	6.424	0.67
0.96	17.9	0.175	0.0462	6.977	7.008	−0.43
0.99	18.7	0.183	0.0462	7.291	7.3	−0.11

In this experiment, the output shaft of Motor-1 is coupled with a bold, which is named as lever length in Figure 6.7. In other words, it is used to apply moment to the balance. After acquiring the information from the balance, it is converted to the force, and multiplied by the length of the bold so that the torque applied by the Motor-1 is calculated. Also, torque contribution to the weight of the lever is taken into account and indicated in Table 6.3 as torque of the lever length, and this value is subtracted from the applied torque. Finally, the given current is multiplied with the torque constant of Motor-1 to compute the theoretical torque. According to the results, the errors are acceptable as the experiment setup is not constructed precisely. The aim of the experiment is to verify, in a quick way, the torque constant of Motor-1.

In Figure 6.8, the flowchart of the experiments introduced in the following sections is illustrated. System is run in 1 kHz. In Test-1, 2 and 4 handle is fixed with the forcer sensor. This setup is defined as fixed-end experiment. On the other hand, in Test-2, drive wheel is free to rotate.

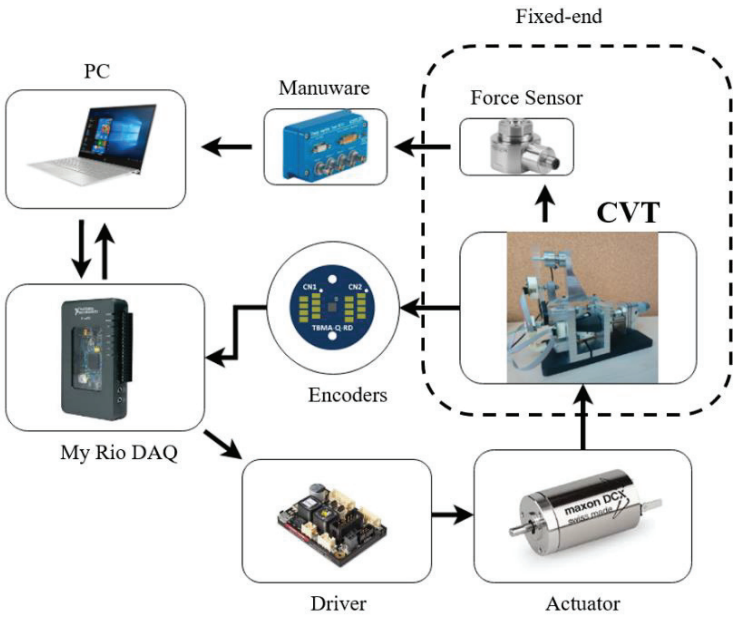

Figure 6.8. Flow chart of the tests

6.2.1 Test 1: The output force verification of the CVT (Fixed-end)

In this test, the output cone is coupled with a moment arm, which is fixed to the inertail frame via a force sensor, and a constant input torque is given to the system from the input cone (Figure 6.9). This procedure is implemented for different transmission levels so that the verification between the theoretical and experimental values are compared. The experiment is conducted for only one direction.

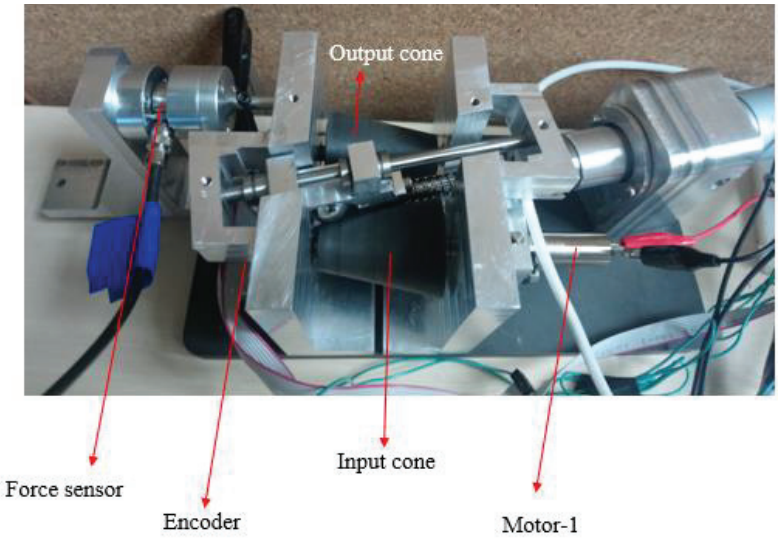

Figure 6.9. The output force verification test setup of the CVT

The calculated values presented in Table 6.3 are acquired by making use of Equation 5.57. The difference between the calculated and the measured values of output force riginates from the elastic behavior of the friction material, and the elastic part of the design is not modelled.

Table 6.3. The illustration of the results of the Test-1

Test points	Z (mm)	Measured Output Force (N)	Calculated Output Force (N)	Error %
1	0	1.1257	1.3019	13.5335
2	8	0.9407	1.0161	7.4125
3	16	0.7082	0.8029	11.7824
4	24	0.6204	0.6378	2.7132
5	32	0.4984	0.5062	1.5384
6	40	0.3757	0.3989	5.8065
7	46.1	0.3284	0.3294	0.2982
Average Error %				6.1550

According to the Figure 6.10, there is a nonlinear relationship between the Z and output force values.

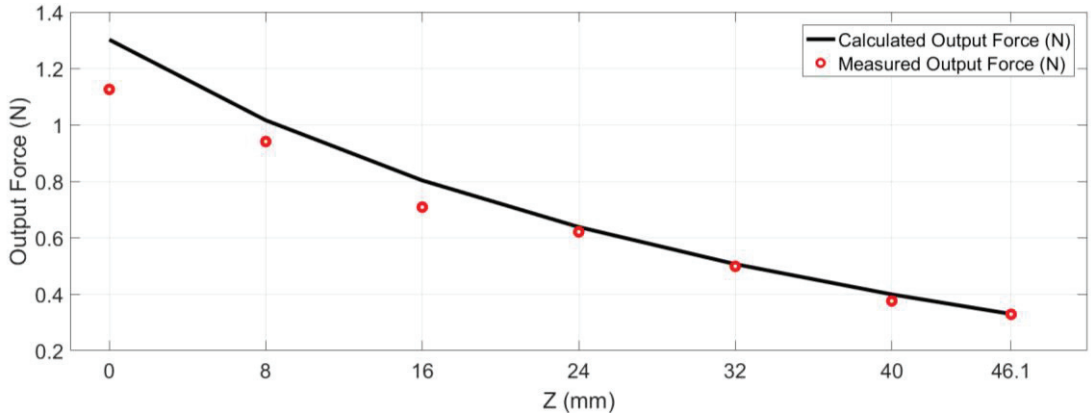

Figure 6.10. The illustration of the correlation graph for the output force verification

The reason for this trend arises from the δ term, which includes numerous nonlinear terms as presented in Equation 5.58.

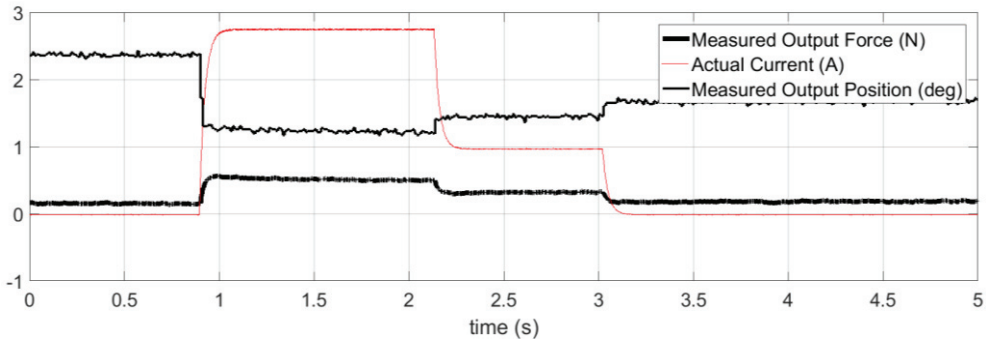

Figure 6.11. The illustration of the measured output force, actual current and measured angular position at the 6th test point

According to the Figure 6.11, measured output force reaches the peak point at 1st second, and then slightly decreases. The issue stems from the viscoelastic behavior of the friction material which is commonly known as the relaxation of the rubber.

On the other hand, the angular position of the input cone changes during this interval since the spheres are pressed between the cones when the input torque is supplied to the system. In other words, the tangential forces takes place at that instant and the applied torque is transmitted from the input cone to the output cone. In the course of this period, the angular position of the cones are changed, and then again replaced within the error, which is around 1.5° in Figure 6.11. Due to this change, the theoretical calculations do not take into account this phenomenon result in erroneous value with respect to the measured values.

6.2.2 Test 2: The bidirectional output force test (Fixed-end)

The aim of this test is to show that the new CVT design is capable of transmitting input torque bidirectionally. To achieve this, handle is coupled with a force sensor which is fixed to the base and the transmission level is varied by actuating Motor-2 (Figure 6.2). Also, the input torque of Motor-1 is adjusted for each transmission level to display 8 N bidirectionally. The calculation of this arrangement is stated in Equation 6.1.

$$\tau_{in} = \frac{\tau_{drivewheel} r_2}{r_3 \delta} \qquad 6.1$$

To obtain the Equation 6.1, Equation 5.65 is substituted into the Equation 5.57. The necessary input torques according to the Z distances is presented in Table 6.4 under input torque column.

Table 6.4. The results of the continuous output force experiment

Test points	Z (mm)	Input torque (mN m)	Measured Output Force in CW (N)	Measured Output Force in CCW (N)
1	0	7.0197	6.4179	−7.4588
2	8	8.9942	6.1375	−6.1315
3	16	11.3824	6.5805	−6.3981
4	24	14.3285	6.2564	−6.4807
5	32	18.0533	6.2185	−6.9378
6	40	22.9115	6.6196	−7.2638
7	46.1	27.74	7.0652	−7.0681
Calculated Output Force (N)				8.0103

According to Table 6.4, the inconsistencies between the CW and CCW directions stem from the adjustment of the pretension mechanism. In other words, the pretension level of the springs that are used to generate normal forces on the cones have a considerable effect on acquiring same output forces. The correlation between the two directions are presented in Figure 6.12.

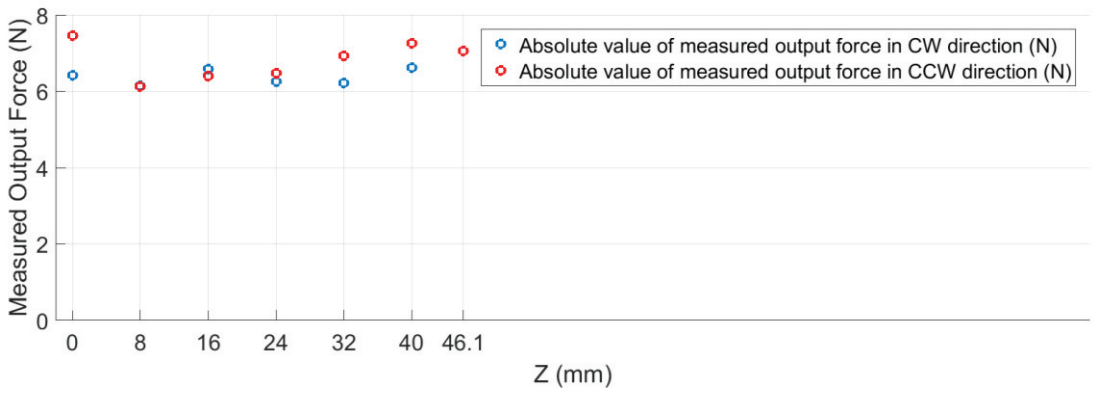

Figure 6.12. The illustration of the correlation graph for the continuous output force verification

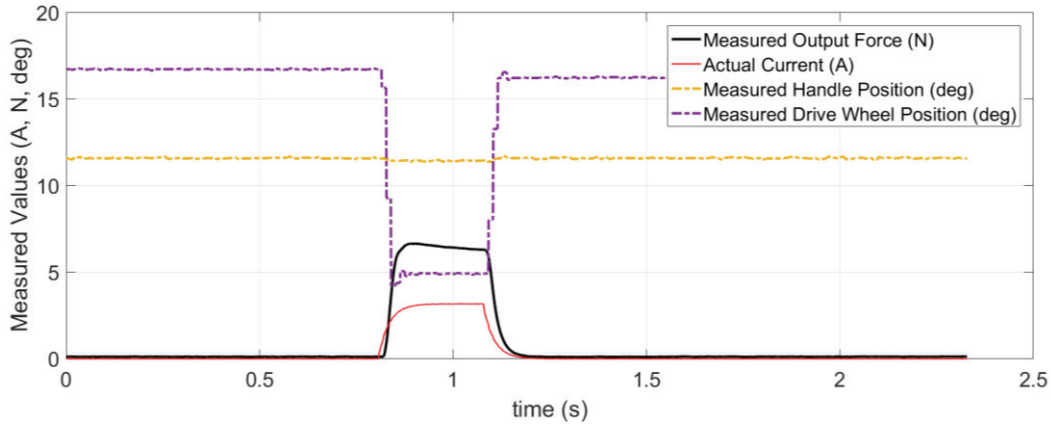

Figure 6.13. The illustration of the measured output force, actual current and measured angular position at the 6th test point

In Figure 6.13, the acquired output signal is presented. It is obvious that when the input torque is applied from the input cone, the tangential forces are occurred, and the input torque is transmitted. At this point, the spheres are compressed between the cones and then this energy is released as if the spring is compressed and released. This effect can be observed from the change in drive wheel position.

6.2.3. Test 3: Independent Motion and Stiffness Variation (Open-end)

In this step, the Motor-2 is given a sine signal to display the stiffness variation, and the position of the drive wheel is measured simultaneously. In this test, the output shaft is free to rotate. The results are given in Figure 6.14.

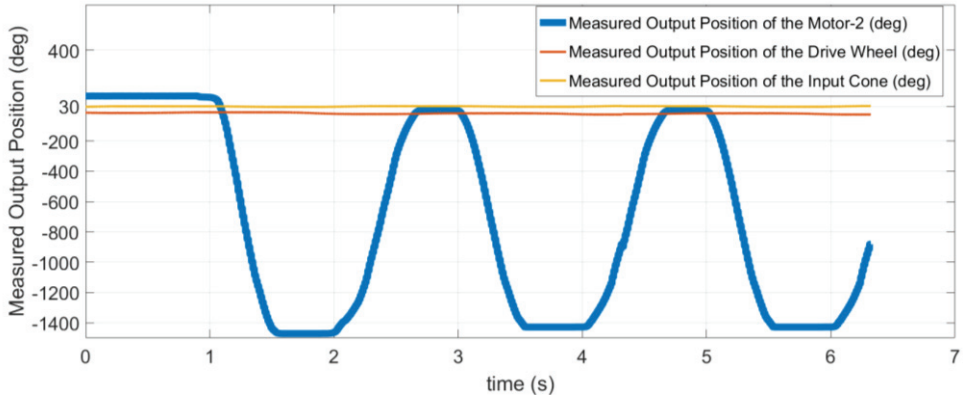

Figure 6.14. The illustration of the test-3 correlation graph

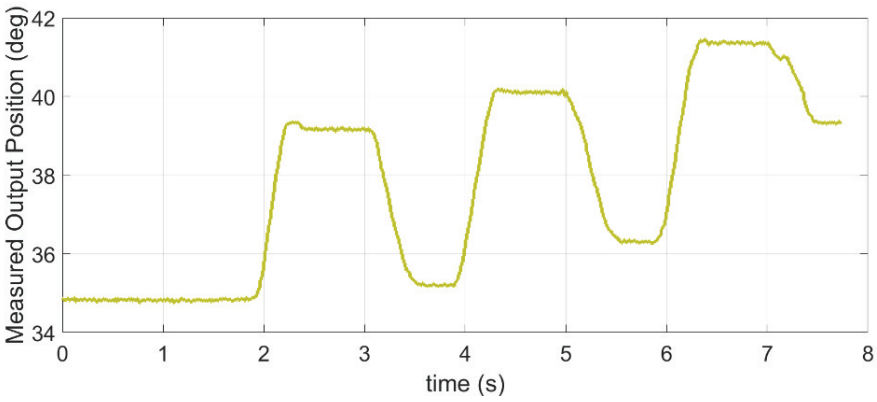

Figure 6.15. The illustration of the position of the Motor-1

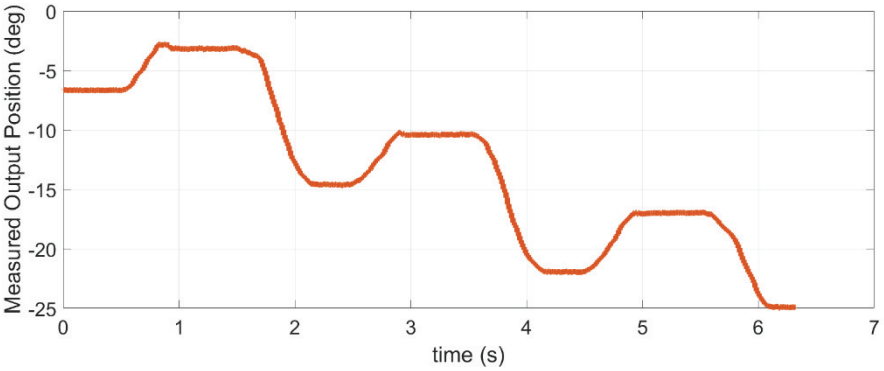

Figure 6.16. The illustration of the position of the drive wheel

According to the Figure 6.16, the maximum position error in the drive wheel is around 8° for each period (rise and fall). On the other hand, the position variation of the Motor-2 (Figure 6.14) is around 1600°. The reason of this error arise from the adjustment of the pretension mechanism (Figure 6.5), which is designed to adjust the normal force level between the cones and the sphere.

6.2.4. Test 5: The shock absorbing (Fixed-end)

In this test, the pretension of the springs are reduced intentionally to show the effect of this phenomenon, that is shock absorbing, on the system.

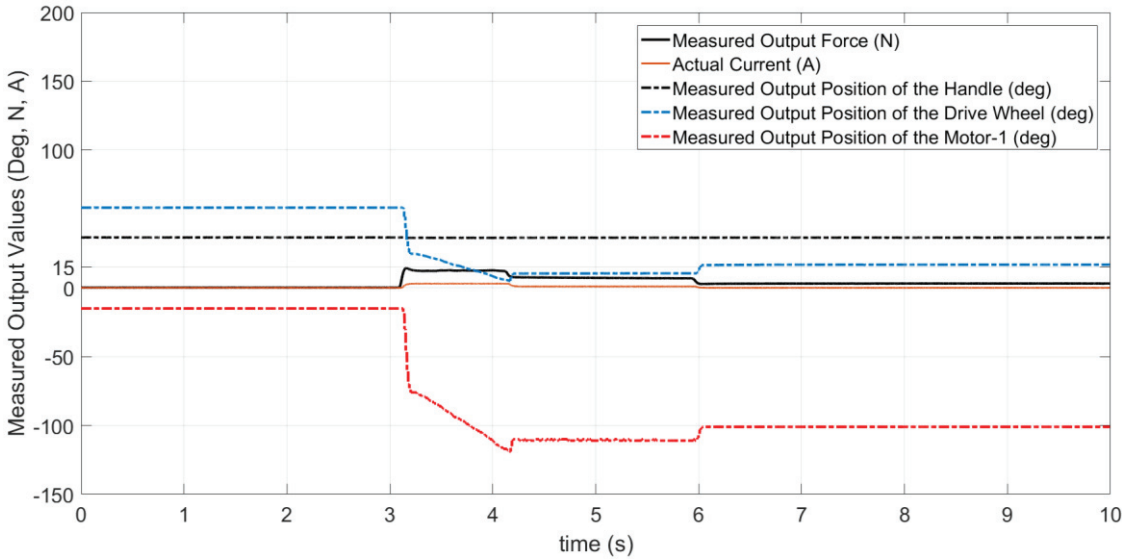

Figure 6.17. The acquired data for the impact test

Motor-1 is driven to supply 22 mN m while the handle is coupled via the force sensor to the inertial frame.

According to the Figure 6.17, it clear that there is a significant slippage between the cones. This situation can be observed from the encoder values of the Motor-1 and drive wheel. It can be concluded new CVT has the potential to regulate the upper transmissible torques.

CHAPTER 7

CONCLUSION

In this thesis, a novel variable stiffness joint design based on two-cone friction drive CVT is carried out. As a first step, the paper (Migliore et al., 2005) is examined, and the prototype introduced in this paper is produced (Figure 2.9) to understand the requirements of the joint designs to be used for human-robot interfaces. Afterwards, the primary reasons why two-cone friction drive CVT systems are not used as a VSA are investigated. The main problems are found to be bidirectional torque transmission and the control of the output torque independent from the output motion. To overcome these issues, a significant modification is performed by changing the transmission element to a sphere. Thus, the first prototype is developed for proof of concept tests. The results show that new CVT has the potential to perform the bidirectional torque transmission within a certain accuracy level.

Neverthless, the inertia of the cones produced for the first prototype should be decreased to minimize the minimum impedance. Moreover, optimization of the mechanism is important to enhance the application of the area of this new CVT in the human-robot interfaces. Therefore, an optimization methodology is studied by making use of the static force analysis of the CVT. To implement this, the geometrical calculations are carried out, and parametric formulas regarding the necessary angles are validated in terms of design parameters with the help of Solidworks models.

Afterwards, velocity level kinematics are examined to verify the speed reduction between the cones. Simulations are constructed in ADAMS and Solidworks software to compare the calculated data with simulation data. The errors between these data is around 1% which stems from the definition of contact points in both simulations. Therefore, this error is acceptable to prove the parametric formula for the velocity level kinematics.

In the next step, static force analysis is conducted to calculate the output torque as a function of input torque and the ratio of the radii. Finally, the optimization methodolgy through manual iterations is implemented to obtain the desired design parameters. Thanks to the optimization methodology, the size of the design is reduced to half of its original size.

After identifying the desired design parameters, the constructional design and the manufacturing processes are carried out for the optimized CVT. Furthermore, four tests are conducted to validate the design. First, the output force verification test is conducted to observe the variation between the output force and Z distance. The error between the measured and calculated data is around 6% which is due to the viscoelastic behaviour of the EPDM rubber. Moreover, in the 2nd test, it is observed that the new CVT has the capability to transmit the input torque bidirectionally within a certain accuracy level. Also, the relaxation behaviour of the viscoelastic material (EPDM) covered on the cones is observed experimentally.

In the next test, the variation of the output torque independent from the output motion is validated. Finally, one of the most prominent requirements for the human-robot joint structures, shock-absorbing, is experimentally tested. Results show that, by adjusting the normal forces via the pre-tension mechanism, the upper transmissible torque limits are altered. Moreover, when the input torque is given to the actuation system, cones compress the spheres between them during the input signal and the torque is transmitted. At the end of this interval, cones return back to their initial position.

As a future study, the system identification of the new CVT shall be studied to determine the impedance range experimentally. Moreover, the continuous desired output force test based on haptic scenario shall be conducted. Additionally, theoretical calculation shall be modified by taking into account the viscoelastic behaviour of the friction material for increasing the accuracy of calculations.

REFERENCES

ABB (2017 (accessed November 9, 2018)).
https://materials.dagstuhl.de/files/17/17071/17071.Bj%C3%B6rnMatthias.Slides2.pdf

Asada, H. H.(2016). Introduction to Robotics. (Lecture Notes), MIT.
https://ocw.mit.edu/courses/mechanical-engineering/2-12-introduction-to-robotics-fall-2005/

Dede, M. I. C. (2003). *Position/Force Control of Robot Manipulators*. (Master's Thesis), Middle East Technical University.

Faulring, E. L., Colgate, J. E., and Peshkin, M. A. (2006). The Cobotic Hand Controller: Design, Control and Performance of a Novel Haptic Display, *International Journal of Robotics Research,* Vol. 25, No. 11, pp. 1099-1119.

Faulring, E. L., Colgate, J. E., and Peshkin, M. A. (2007). Power Efficiency of the Rotational-to-Linear Infinitely Variable Cobotic Transmsission, *Journal of Mechanical Design,* Vol. 129, No. 12, pp. 1285–1293.

Force Dimension (2018 (accessed December 13, 2018)).
http://www.forcedimension.com/company/about

Grebenstein, M., Albu-Schaeffer, A., Bahls, T., Chalon, M., Eiberger, O., Friedl, W., Gruber, R., Haddadin, S., Hagn, U., Haslinger, R., Hoppner, H., Jorg, S., Nickl, M., Nothhelfer, A., Petit, F., Reill, J., Seitz, N., Wimbock, T., Wolf, S., Wusthoff, T., and Hirzinger G. (2011). The DLR Hand Arm System, *In Proceedings of the IEEE International Conference on Robotics and Automation*, 3175–82.

Ishida, T., and Takanashi, A.(2006). A Robot Actuator Development with High Backdrivability. *In Proceedings of the IEEE International Conference on Robotics and Automation*.

Ivanov, K. (2012). Self-Adjusting Motor-Wheel with CVT, *International Journal of Engineering and Innovative Technology(IJEIT),* Vol. 2, No. 5, pp. 287-91.

Ivanov, K.(2015). To the Discovery "Effect of Force Adaptation". *In Transactions of 14th Working Meeting IFTOMM Permanent Commission for the History of Mechanism and Machine Science(Workshop HMMS-2015)*.

Ivanov, K., Ualiev, G., and Tultaev, B. (2014). Kinematic and Force Analysis of Robot with Adaptive Electric Drives, *Applied Mechanics and Materials*, vol. 555.

Kim, J., Park, F. C., Park, Y., and Shizuo, M. (2002). Design and Analysis of a Spherical Continuously Variable Transmission, *Journal of Mechanical Design,* Vol. 124, No. 1, pp. 21–29.

Laffranchi, M., Tsagarakis, N. G., Cannella, F., and Caldwell, D. G. (2009). Antagonistic and Series Elastic Actuators: a Comparative Analysis on the Energy Consumption. *In Proceedings of the IEEE* , 5678–84.

Li, H., Liu, W., Wang, K., Kawashima, K., and Magid, E. (2018). A Cable-Pulley Transmission Mechanism for Surgical Robot with Backdrivable Capability, *Robotics and Computer-Integrated Manufacturing,* Vol. 49, pp. 328–34.

Lu, Y., and Fan, D., (2012). Transmission Backlash of Precise Cable Drive System, *Journal of Mechanical Engineering Science,* Vol. 227, pp. 2256–67.

Martinez, M. O., Morimoto, T. K., Taylor, A. T., Barron, A. C., Pultorak, J. D. A., Wang, J., Kaiser, A. G., Davis, R. L., Blikstein, P., and Okamura, A. M.(2016). 3-D Printed Haptic Devices for Educational Applications. *In Proceedings of the IEEE Haptics Symposium*, 126–133.

Migliore, S. A., Brown, E. A., and DeWeerth, S. P.(2005). Biologically Inspired Stiffness Control, *Proceedings of the IEEE International Conference on Robotics and Automation*, *4508*–13.

Petit, F., Chalon, M., Friedl, W., Grebenstein, M., Albu-Schaffer, A., and Hirzinger, G.(2010). Bidirectional Antagonistic Variable Stiffness Actuation: Analysis, Design and Implementation. *In Proceedings of the IEEE International Conference on Robotics and Automation*, 4189–96.

3dsystems (2018 (accessed December 13, 2018)). https://www.3dsystems.com/haptics-devices/3d-systems-phantom-premium

Pratt, G. A., and Williamson, M.M.(1995). Series Elastic Actuators, *19th Proceedings IEEE/RSJ International Conference on Intelligent Robots and Systems. Human Robot Interaction and Cooperative Robots* 1(1524), 399–406.

Salisbury, J. K. (1980). Active Stiffness Control of a Manipulator in Cartesian Coordinates, *19th IEEE Conference on Decision and Control including the Symposium on Adaptive Processes, 95*–100.

Samur, E. (2012). *Performance Metrics for Haptic Interfaces*. (PhD Thesis), EPFL.

Sclater, N. (2001). *Mechanism & Mechanical Devices Sourcebook, Third Edition*. McGraw-Hill.

Tonietti, G., Schiavi, R., and Bicchi, A.(2005). Design and Control of a Variable Stiffness Actuator for Safe and Physical Human-Robot Interaction, *In Proceedings of the IEEE International Conference on Robotics and Automation*, 526–31.

Vanderborght, B., Albu-Schaeffer, A., Bicchi, A., Burdet, E., Caldwell, D.G., Carloni, R., Catalano, M., Eiberger, O., Friedl, W., Ganesh, G., Garabini, M., Grebenstein, M., Grioli, G., Haddadin, S., Hoppner, H., Jafari, A., Laffranchi, M., Lefeber, D., Petit, F., Stramigioli, S., Tsagarakis, N., Damme, M.V., Ham, R.V., Visser, L. C., and Wolf, S.(2013). Variable Impedance Actuators: A review. *Robotics and Autonomous Systems,* Vol. 61, No. 12, pp. 1601–14.

Visser, L. (2013). *Modeling, Control and Application to Compliant Bipedal Walking*. (Master's Thesis), University of Twente.

Visser, L. C., Carloni, R., and Stramigioli, S.(2011). Energy-Efficient Variable Stiffness Actuators. *IEEE Transactions of the Robotics,* Vol. 27, No. 5, pp. 865-75.

Williamson, M. *Series Elastic Actuators* (1995). M.S. Thesis, M. I. T.

Wolf, S., and Hirzinger, G., (2008). A New Variable Stiffness Design: Matching Requirements of the Next Robot Generation, *In Proceedings of the IEEE International Conference on Robotics and Automation*, 1741–46.